



Powering Stellar Magnetism: Energy Transfers in Cyclic Dynamos of Sun-like Stars

Allan Sacha Brun¹ , Antoine Strugarek¹ , Quentin Noraz¹ , Barbara Perri^{1,2} , Jacobo Varela^{1,3} , Kyle Augustson¹ , Paul Charbonneau⁴ , and Juri Toomre⁵

¹ Département d'Astrophysique/AIM, CEA/IRFU, CNRS/INSU, Univ. Paris-Saclay & Univ. de Paris, F-91191 Gif-sur-Yvette, France; sacha.brun@cea.fr

² Centre for Mathematical Plasma Astrophysics, KU Leuven, Celestijnenlaan 200b-box 2400, B-3001 Leuven, Belgium

³ Universidad Carlos III de Madrid, Leganés, E-28911, Spain

⁴ Département de physique, Université de Montréal, C.P. 6128 Succ. Centre-Ville, Montréal, QC H3C-3J7, Canada

⁵ JILA and Department of Astrophysical and Planetary Sciences, University of Colorado, Boulder, CO 80309-0440, USA

Received 2021 June 30; revised 2021 November 30; accepted 2021 December 23; published 2022 February 9

Abstract

We use the anelastic spherical harmonic code to model the convective dynamo of solar-type stars. Based on a series of 15 3D MHD simulations spanning four bins in rotation and mass, we show what mechanisms are at work in these stellar dynamos with and without magnetic cycles and how global stellar parameters affect the outcome. We also derive scaling laws for the differential rotation and magnetic field based on these simulations. We find a weaker trend between differential rotation and stellar rotation rate, ($\Delta\Omega \propto (|\Omega|/\Omega_\odot)^{0.46}$) in the MHD solutions than in their HD counterpart ($|\Omega|/\Omega_\odot^{0.66}$), yielding a better agreement with the observational trends based on power laws. We find that for a fluid Rossby number between $0.15 \lesssim Ro_f \lesssim 0.65$, the solutions possess long magnetic cycle, if $Ro_f \lesssim 0.42$ a short cycle and if $Ro_f \gtrsim 1$ (antisolar-like differential rotation), a statistically steady state. We show that short-cycle dynamos follow the classical Parker–Yoshimura rule whereas the long-cycle period ones do not. We also find efficient energy transfer between reservoirs, leading to the conversion of several percent of the star's luminosity into magnetic energy that could provide enough free energy to sustain intense eruptive behavior at the star's surface. We further demonstrate that the Rossby number dependency of the large-scale surface magnetic field in the simulation ($B_{L,surf} \sim Ro_f^{-1.26}$) agrees better with observations ($B_V \sim Ro_s^{-1.4 \pm 0.1}$) and differs from dynamo scaling based on the global magnetic energy ($B_{bulk} \sim Ro_f^{-0.5}$).

Unified Astronomy Thesaurus concepts: Solar dynamo (2001); Solar magnetic fields (1503); Stellar magnetic fields (1610); Stellar rotation (1629); Solar differential rotation (1996); Magnetohydrodynamics (1964); Stellar convection envelopes (299); Magnetohydrodynamical simulations (1966); Solar analogs (1941); K stars (878); G stars (558)

1. Introduction

Sun-like stars go through various magnetic activity phases in their lives. From young very active T Tauri stars rotating much faster than our Sun to old stars that are less active, it is key to understand how convection, rotation, turbulence, magnetism, and surface activity evolve and feedback on one another over secular time. Of particular interest is the generation of magnetic field via dynamo action, because it is both the source of key temporal variabilities like the Schwabe 11 yr or Gleissberg 90 yr magnetic cycles in the Sun and at the heart of a complex feedback loop between stellar magnetism and rotation via wind braking and the loss of mass and angular momentum by the star (Matt et al. 2015; Brun & Browning 2017; Vidotto 2021). It is also key in providing the free energy reservoir needed to power eruptive events such as flares or coronal mass ejections (Shibata et al. 2013; Aschwanden et al. 2015; Maehara et al. 2017). In this work, we seek to assess how solar-like stars with different masses and rotation rates can power their magnetism by means of dynamo action in their convective envelopes.

Various activity indicators have been derived observationally over the last 50 yr using, for instance, photometric and spectroscopic variability (Baliunas et al. 1995; Oláh et al. 2009; Egeland 2017; Boro Saikia et al. 2018) and more recently

through asteroseismology (García & Aalot 2019) to connect the spectral class and age of a star to its dynamical properties and activity level. Turning specifically to solar-type stars, spectropolarimetric studies have revealed several interesting properties (Marsden et al. 2014). In Vidotto et al. (2014), it was shown that the large-scale magnetic field is following a scaling law with the stellar Rossby number $\langle B_V \rangle \propto Ro_s^{-1.38 \pm 0.14}$ for stars with $Ro_s > 0.1$ (here the stellar Rossby number is defined as the ratio between the rotation period and the convective turnover time). More recently, See et al. (2019b) have revisited this trend and found a similar result with $\langle B_V \rangle \propto Ro_s^{-1.40 \pm 0.10}$. It was also proposed in Petit et al. (2008) and later by See et al. (2015) that the toroidal magnetic field dominates over the poloidal field for fast rotators. It was further shown that no significant collapse of the large-scale field with respect to higher multipole moments was observed as the star evolved and is found less active (Vidotto et al. 2016). Recent work by Lehtinen et al. (2021) including more evolved stars seems to help constrain better the rotation–activity relationship, confirming that considering the Rossby number is better than the rotation period alone. In Karoff et al. (2018), the possibility that larger metallicity increases the activity level of solar analogs was also proposed.

Moreover, long observational studies based on Ca II H&K chromospheric observations have shown that magnetic activity of solar-like stars (Wilson 1978; Saar 1990; Plachinda & Tarasova 1999; Hall et al. 2007; Hall 2008) can be found to be either irregular with no obvious cyclic activity or to possess

activity cycles with short magnetic cycle periods (Metcalf et al. 2010; Jeffers et al. 2018) or long (decadal) ones (Noyes et al. 1984; Baliunas et al. 1995) as in the Sun. Such studies have further indicated the existence of a relation between Rossby number and magnetic cycle periods, its exact nature being still debated given the relatively small numbers of truly confirmed cyclic magnetic stars (do Nascimento et al. 2014; Egeland 2017).

A puzzling property regarding stellar magnetic cycles has been the existence (or not) of active and inactive branches of stellar activity, as proposed by Saar & Brandenburg (1999) and Böhm-Vitense (2007). Recently it has been argued that stars may be transiting from one state to the other as they evolve and that such distinct activity branches do not exist. Instead, activity would be decreasing while rotation would be almost unchanged beyond a certain age or stellar internal dynamo state. A key quantity to characterize this activity state transition is again the Rossby number. Metcalfe & van Saders (2017) proposed that once their Rossby number becomes large, stars stop braking through their stellar wind, hence departing from the classical Skumanich law $\Omega(t) \propto t^{-0.5}$ and gyrochronology trend (Skumanich 1972; Barnes 2003, 2007). This is still highly debated in the community as some observers find stars older than the Sun still following Skumanich’s law (Meibom et al. 2015; Barnes et al. 2016; Lorenzo-Oliveira et al. 2018, 2019; do Nascimento et al. 2020) while others do not (Metcalf et al. 2016; Metcalfe & Egeland 2019; Hall et al. 2021). The disagreement could also be due to the observation techniques (photometric versus chromospheric studies for instance) and observational data set (Kepler data versus long-term monitoring of individual stars) used, as each has rotation rate and age determination that sometimes differ significantly (Lorenzo-Oliveira et al. 2016; do Nascimento et al. 2020). Another alternative would be that stars temporarily stop spinning down before starting again (Curtis et al. 2020; Spada & Lanzafame 2020) or that the coronal temperature drops, yielding a smaller mass loss for older stars (Ó Fionnagáin & Vidotto 2018). Thus, understanding what happens from a theoretical point of view to stellar dynamo and magnetic field geometry for large Rossby numbers is crucial in helping to interpret the most recent observations. This is one of the goals of this study. Given the close link between surface activity and stellar magnetism, a key aspect to characterize is the amount of magnetic energy made available in a given solar-like star by dynamo action. We know that flare intensity is linked to the magnetic energy made available to the magnetic structures. It is thus crucial to better characterize energy transfers in solar-type star dynamos for a wide range of Rossby numbers.

Characterizing the differential rotation (DR) realized at the base and in the convective envelope of solar-type stars is central to the understanding of their magnetic field generation, activity level, and rotation, as it is directly linked to the Ω effect (e.g., stretching of the poloidal magnetic field lines by large-scale shear). Hence, the role of DR in driving the star’s magnetic activity level and field properties should be clarified (Donahue et al. 1996). Doppler imaging (Donati & Collier Cameron 1997; Barnes et al. 2005), asteroseismology (Gizon & Solanki 2004; Reinhold et al. 2013; García et al. 2014), classical spot models (Lanza et al. 2014), and short-term Fourier transform (Vida et al. 2014) are methods to infer DR. The combination of all these observations on stellar rotation and magnetism helps constrain the trends linking rotation with

stellar DR and magnetic activity. Various analyses of stellar DR revealed different dependencies between DR and star’s rotation ($\Delta\Omega \propto \Omega^n$), with n varying between 0.15 and 0.7 (Barnes et al. 2005; Reiners 2006; Reinhold et al. 2013). There is no clear consensus in the community for now; some authors are even advocating that such laws should be derived per spectral stellar classes and that the confusion comes from mixing together F and K stars (Balona & Abedigamba 2016). Saar (2011), Brandenburg & Giampapa (2018) also propose that the dependency of the DR with the rotation rate may not be monotonic, with a break near Rossby equals unity. By contrast, a more systematic and stronger dependency is observed with the star’s temperature ($\Delta\Omega \propto T_{\text{eff}}^{8.92}$, Barnes et al. 2005, Reinhold et al. 2013; and $\Delta\Omega \propto T_{\text{eff}}^{8.6}$, Collier Cameron 2007). Hence, we expect large-scale shear to vary both in amplitude and profile (as a function of latitude and depth) as the global stellar parameters change. Some recent studies have confirmed this is happening in solar-type stars by inverting seismically their profile (Benomar et al. 2018), pointing to a possible antisolar DR state (e.g., slow equator/fast poles), which was possibly already guessed in F stars (Reiners 2007) and advocated to exist in numerical simulations (Matt et al. 2011; Gastine et al. 2014; Brun et al. 2015, see below).

Considering the large number of global stellar parameters probed by these different observational studies, it is expected that the excitation of various types of convective dynamos may occur (Weiss 1994; Tobias 1998; Brun & Browning 2017; Brandenburg & Giampapa 2018; Charbonneau 2020). In order to quantify the influence of key parameters such as rotation and mass in characterizing the dynamo and magnetic level achieved in solar-like stars and given the intrinsic nonlinear mechanisms at work in stellar dynamos, multi-D numerical simulations have been developed over the years in an attempt to provide more quantitative answers.

Some studies have used the 2.5D mean-field dynamo approach to do so, extending solar mean-field dynamo models to other stellar spectral types (Chabrier & Küker 2006; Jouve et al. 2010; Küker et al. 2011; Kitchatinov et al. 2018, and references therein). While these studies are very helpful, most of them lack the full nonlinearity and genuine parametric dependence of 3D magnetohydrodynamic (MHD) simulations. Recent developments by Pipin (2021) are starting to overcome these limits and have extended the work of Rempel (2006) on the Sun to solar-type stars with various rotation rates. Nevertheless, with the arrival of more powerful supercomputers, other authors have used instead global 3D MHD simulations to model DR and stellar magnetism in the convection zone of solar-like stars (Glatzmaier & Gilman 1982; Miesch et al. 2000, 2006; Brun et al. 2004, 2011; Brown et al. 2008, 2010; Ghizaru et al. 2010; Käpylä et al. 2011, 2014; Gastine et al. 2014; Augustson et al. 2015; Karak et al. 2015). These studies pointed out the large magnetic temporal variability and the critical effect of stellar rotation and mass on magnetic field generation through dynamo mechanism, leading in some parameter regimes to configurations with cyclic activity (Gilman & Miller 1981; Gilman 1983; Glatzmaier 1985a; Brown et al. 2011; Racine et al. 2011; Augustson et al. 2013, 2015; Käpylä et al. 2013; Nelson et al. 2013; Beaudoin et al. 2016; Guerrero et al. 2016, 2019; Strugarek et al. 2017, 2018; Viviani et al. 2018, 2019; Warnecke 2018; Matilsky & Toomre 2020). Several studies pointed out the positive effect of a stable region underneath the

convection zone (Parker 1993) on the efficient storage of intense toroidal field and the lengthening of the stellar dynamo cycle period (Glatzmaier 1985b; Browning et al. 2006; Lawson et al. 2015; Beaudoin et al. 2016; Guerrero et al. 2016, 2019; Käpylä et al. 2019; Bice & Toomre 2020). Over the last decade, significant progress has been made in successfully simulating large-scale mean flows and stellar activity cycle using different numerical codes and methods (Jones et al. 2011). This is quite reassuring that a global consensus is growing on the nature of solar-like star dynamos. It is common knowledge that there are still key transitions in Rossby number (at low and high values of this parameter) that need to be understood further, as well as what is the exact type of convective dynamos realized in solar-like stars as their global parameters are varied. This study continues this effort by doing an even broader systematic parametric study of solar-like star dynamos coupled to a stably stratified layer below than what have been published so far. It extends the work published in Varela et al. (2016) and Brun et al. (2017) with the MHD anelastic spherical harmonic code (ASH) (Brun et al. 2004). In particular, we wish to better characterize energy transfers and how much of a star's energy (luminosity) is converted into magnetic energy by nonlinear global convective dynamos over a wide range of Rossby numbers, generalizing to solar-like stars the work by Starr & Gilman (1966) and Rempel (2006).

In the following sections, we analyze how DR and magnetism feedback on one another (Brun 2004; Fan & Fang 2014), as well as how kinetic and magnetic energies flow within a stellar magnetized rotating convective envelope, using 15 convective dynamo MHD simulations for model stars with different masses and rotation rates (hence Rossby numbers) in order to achieve this goal. In Section 2 we present the equations and model setup. In Section 3 we give a quick overview of one of the dynamo solutions emphasizing the main properties of a cyclic solution. In Section 4 we discuss the various DR profiles obtained in our parametric studies, expanding Varela et al. (2016) to include 15 models. We discuss angular momentum and various scaling laws of the DR contrast $\Delta\Omega$. In Section 5 we analyze our dynamo solutions for various key properties as a function of the Rossby number, such as their activity level, the amount of magnetic flux generated by the dynamo, the existence or not of an activity cycle and torsional oscillations, how the cycle period for cyclic solutions changes, what is the relative contribution of dipolar and quadrupolar magnetic fields in the overall dynamo-generated magnetic field, and interpret our simulations in terms of mean-field α - Ω classification. We further expand our data set with the 17 simulations published previously Strugarek et al. (2017, 2018) with the Eulag-MHD code (Smolarkiewicz & Charbonneau 2013), in order to improve the statistics. In Section 6 we perform an extensive study of energy transfer between various reservoirs in stellar dynamos, assessing how much magnetic energy is accessible to stars like our Sun to power eruptive events. We compute all MHD transfers between kinetic and energy reservoirs for the large-scale flows and magnetic fields. In Section 7 we reflect on our findings in an astrophysical context, comparing our results with recent observational results and then conclude.

2. Numerical Setup

In this section we present the main features of the ASH code, describing the boundary and initial conditions of the numerical models and our choice of global parameters.

2.1. Set of Equations Solved

We perform 3D MHD simulations of convective dynamo action coupled to a stable radiative interior where the anelastic MHD equations are solved for the motions of a conductive plasma in a rotating sphere (Jones et al. 2011). The anelastic approximation captures the effects of density stratification without having to resolve sound waves, which would severely limit the time step (Brown et al. 2012). In the MHD context, the anelastic approximation filters out fast magnetoacoustic waves but retains Alfvén waves.

The code ASH uses a pseudo-spectral method (Clune et al. 1999). The velocity (\mathbf{v}), magnetic (\mathbf{B}), and thermodynamic variables (entropy S , pressure P) are expanded in spherical harmonics $Y_{lm}(\theta, \phi)$ for their horizontal structure and in Chebyshev polynomials $T_n(r)$ for their radial structure (Brun et al. 2004). The density (ρ), entropy, pressure, and temperature (T) are linearized about the spherically symmetric background values, denoted by the symbol ($\hat{\cdot}$). The equations solved by ASH are (Brun et al. 2004)

$$\nabla \cdot \hat{\rho} \mathbf{v} = 0, \quad \nabla \cdot \mathbf{B} = 0 \quad (1)$$

$$\begin{aligned} \hat{\rho} \left(\frac{\partial \mathbf{v}}{\partial t} + (\mathbf{v} \cdot \nabla) \mathbf{v} + 2\Omega_* \times \mathbf{v} \right) \\ = -\nabla P + \rho \mathbf{g} + \frac{1}{4\pi} (\nabla \times \mathbf{B}) \times \mathbf{B} + \nabla \cdot \mathcal{D} \end{aligned} \quad (2)$$

$$\hat{\rho} \hat{T} \frac{\partial S}{\partial t} = -\hat{\rho} \hat{T} \mathbf{v} \cdot \nabla (\hat{S} + S) - \nabla \cdot \mathbf{q} + \Phi_d + \hat{\rho} \epsilon \quad (3)$$

$$\frac{\partial \mathbf{B}}{\partial t} = \nabla \times [\mathbf{v} \times \mathbf{B} - \eta \nabla \times \mathbf{B}], \quad (4)$$

with the velocity field $\mathbf{v} = v_r \hat{\mathbf{e}}_r + v_\theta \hat{\mathbf{e}}_\theta + v_\varphi \hat{\mathbf{e}}_\varphi$, the magnetic field $\mathbf{B} = B_r \hat{\mathbf{e}}_r + B_\theta \hat{\mathbf{e}}_\theta + B_\varphi \hat{\mathbf{e}}_\varphi$, the angular velocity in the rotation frame $\Omega_* = \Omega_* \hat{\mathbf{e}}_z$, $\hat{\mathbf{e}}_z$ the unit vector along the rotation axis, and g the magnitude of the gravitational acceleration. A volumetric heating term $\hat{\rho} \epsilon$ is also taken into account to approximate the generation of energy by nuclear reactions in the stellar core. The nuclear reactions are modeled very simply by assuming that $\epsilon = \epsilon_0 \hat{T}^{n_c}$. By enforcing that the integrated luminosity of the star matches its known surface value, we can determine ϵ_0 and n_c as listed in Table 7 of Brun et al. (2017). Note that only the low-mass star series of models (e.g., 0.5 and 0.7 M_\odot) require that heating source term, because their computational domain includes a portion of the nuclear energy generation core.

The diffusion tensor \mathcal{D} and the dissipative term Φ_d are defined as

$$D_{ij} = 2\hat{\rho} \nu \left[e_{ij} - \frac{1}{3} \nabla \cdot \mathbf{v} \delta_{ij} \right],$$

$$\Phi_d = 2\hat{\rho} \nu \left[e_{ij} e_{ij} - \frac{1}{3} (\nabla \cdot \mathbf{v})^2 \right] + \frac{4\pi\eta}{c^2} \mathbf{J}^2,$$

with e_{ij} the stress tensor and $\mathbf{J} = c/4\pi \nabla \times \mathbf{B}$ the current density. The energy flux \mathbf{q} is the sum of a radiation flux and of a turbulent entropy diffusion flux:

$$\mathbf{q} = \kappa_r \hat{\rho} c_p \nabla (\hat{T} + T) + \kappa \hat{\rho} \hat{T} \nabla S + \kappa_0 \hat{\rho} \hat{T} \frac{\partial \hat{S}}{\partial r} \hat{\mathbf{e}}_r,$$

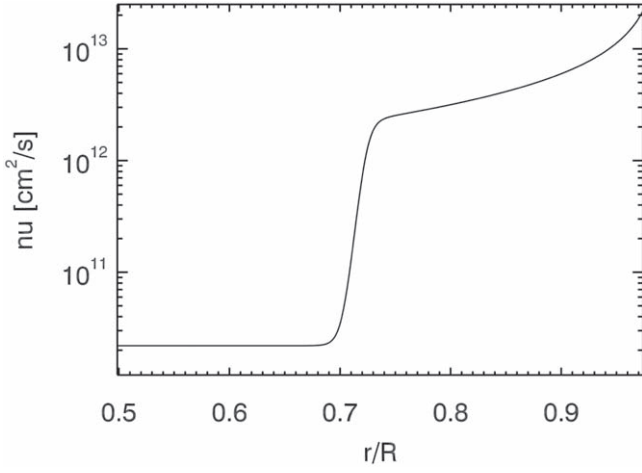


Figure 1. Typical radial profile of kinematic viscosity ν used in this study, here for case M11R3m. Profiles of κ and η are the same, but their amplitude depends respectively for each case on the chosen Prandtl and magnetic Prandtl numbers (see Table 3).

with ν , κ , and η the effective eddy diffusivities of the momentum, heat, and magnetic field transport, κ_r the atomic radiation diffusion coefficient, κ_0 the effective thermal diffusivity acting only on the spherically symmetric ($l=0$) entropy gradient, and c_p the specific heat at constant pressure.

Due to limitations in computing resources, current numerical simulations cannot capture all scales of solar convective motions and magnetic fields from global to atomic dissipation scales. The simulations described in this study resolve nonlinear interactions among a large range of scales but motions and magnetic fields still exist in solar-like stars on scales smaller than our grid resolution. Hence, our models should be considered as large-eddy simulations (LES) with parameterization to account for subgrid-scale (SGS) motions. The effective eddy diffusivities ν , κ , and η represent momentum, heat, and magnetic field transport by motions that are not resolved by the simulation. They are allowed to vary with radius but are independent of latitude, longitude, and time for a given simulation. In the simulations reported here, ν , κ , and η have the following profile:

$$\nu(r) = \nu_{\text{bot}} + \nu_{\text{top}} f_{\text{step}}(r),$$

where

$$\begin{aligned} f_{\text{step}}(r) &= (\hat{\rho}/\hat{\rho}_{\text{top}})^\alpha [1 - \beta] f(r), \\ f(r) &= 0.5(\tanh((r - r_t)/\sigma_t) + 1), \\ \beta &= \nu_{\text{bot}}/\nu_{\text{top}} = 10^{-3}, \end{aligned}$$

and with ν , ν_{bot} and ν_{top} in $\text{cm}^2 \text{s}^{-1}$ and r_t and σ_t in cm, as provided in Table 7 of Brun et al. (2017), and α is -0.5 for all cases. All models assumed a Prandtl number $Pr = \nu/\kappa$ of 0.25, so that κ can be directly obtained from the amplitude and profile of ν . The magnetic Prandtl number $P_m = \nu/\eta$ is equal to 1 or 2 depending on the case considered (see Table 3), so that η can as well be deduced from ν . These tapered profiles are chosen in order to take into account the much smaller subgrid-scale transport expected in the stably stratified radiative interior. A representative profile is shown in Figure 1. Their amplitudes are adapted for each rotation rate and stellar mass considered in order to achieve the best turbulent convective

dynamo states while retaining a reasonable numerical resolution and computing effort (still, each model has used of the order of 8 to 10 million CPU hours spread over several years).

The diffusivity κ_0 is set such as to have the unresolved eddy flux carrying the solar flux outward at the top of the domain (see Figure 2). It drops off exponentially with depth in order to avoid a large inward heat flux in the stable zone (see Miesch et al. 2000). Of course, there is some arbitrariness in choosing the exact shape and amplitude of our diffusivity profiles, and we do our best to limit their influence on the results reported here.

The mass flux and magnetic vector fields are maintained divergenceless by a stream function formalism (Brun et al. 2004):

$$\hat{\rho}\mathbf{v} = \nabla \times \nabla \times (W\hat{\mathbf{e}}_r) + \nabla \times (Z\hat{\mathbf{e}}_r), \quad (5)$$

$$\mathbf{B} = \nabla \times \nabla \times (C\hat{\mathbf{e}}_r) + \nabla \times (A\hat{\mathbf{e}}_r). \quad (6)$$

A perfect ideal gas equation is used for the mean state and the fluctuations are linearized:

$$\begin{aligned} \hat{P} &= (\gamma - 1)c_p \hat{\rho} \hat{T} / \gamma \\ \rho / \hat{\rho} &= P / \hat{P} - T / \hat{T} = P / \gamma \hat{P} - S / c_p \end{aligned}$$

with $\gamma = 5/3$ the adiabatic exponent.

The anelastic MHD system of equations requires 12 boundary conditions (BCs). We use an impenetrable and stress-free BCs at the top and bottom of the domain, i.e.,

$$v_r = \frac{\partial}{\partial r} \left(\frac{v_\theta}{r} \right) = \frac{\partial}{\partial r} \left(\frac{v_\phi}{r} \right) = 0.$$

Magnetic BCs are perfectly conducting at the lower radial boundary and the magnetic field matches a potential field in the upper boundary: $B_r|_{r_{\text{bot}}} = \frac{\partial}{\partial r} \left(\frac{B_\theta}{r} \right)|_{r_{\text{bot}}} = \frac{\partial}{\partial r} \left(\frac{B_\phi}{r} \right)|_{r_{\text{bot}}} = 0$ and $B_r|_{r_{\text{top}}} = \nabla \Psi \Rightarrow \Delta \Psi = 0$, with r_{top} and r_{bot} , respectively, the radius of the top and bottom of the numerical domain and r_{bcz} that of the base of the convective layer (see Table 1).

Finally, we maintain the entropy flux at the top and bottom. Keeping the values of $d\hat{S}/dr|_{r_{\text{top}}, r_{\text{bot}}}$ fixed at all times in the simulations further implies that the fluctuating dS/dr is set to zero at both BCs.

2.2. Model Structure and Initialization

The simulation is focused on the bulk convection zone, avoiding regions too close to the stellar surface. We include a stably stratified layer below the convective envelope, hence providing a realistic bottom boundary condition for the fields and flow that are allowed to be pumped down and to penetrate into the radiative interior. The code uses a realistic background stratification for the profiles of entropy (\hat{S}), density ($\hat{\rho}$), temperature (\hat{T}) derived from a one-dimensional solar-structure model CESAM (Morel 1997; Brun et al. 2002). Our starting point is the G- and K-star rotating convective 3D models published in Brun et al. (2017) (see also Matt et al. 2011; Brun et al. 2015 and Table 1).

The MHD models are initialized from their equivalent progenitor hydrodynamical models in which a small magnetic field perturbation is introduced in the convective envelope (many orders smaller than the final magnetic field observed in the simulation). In that hydrodynamic study we published 15 simulations covering four mass bins and four rotation rates. We

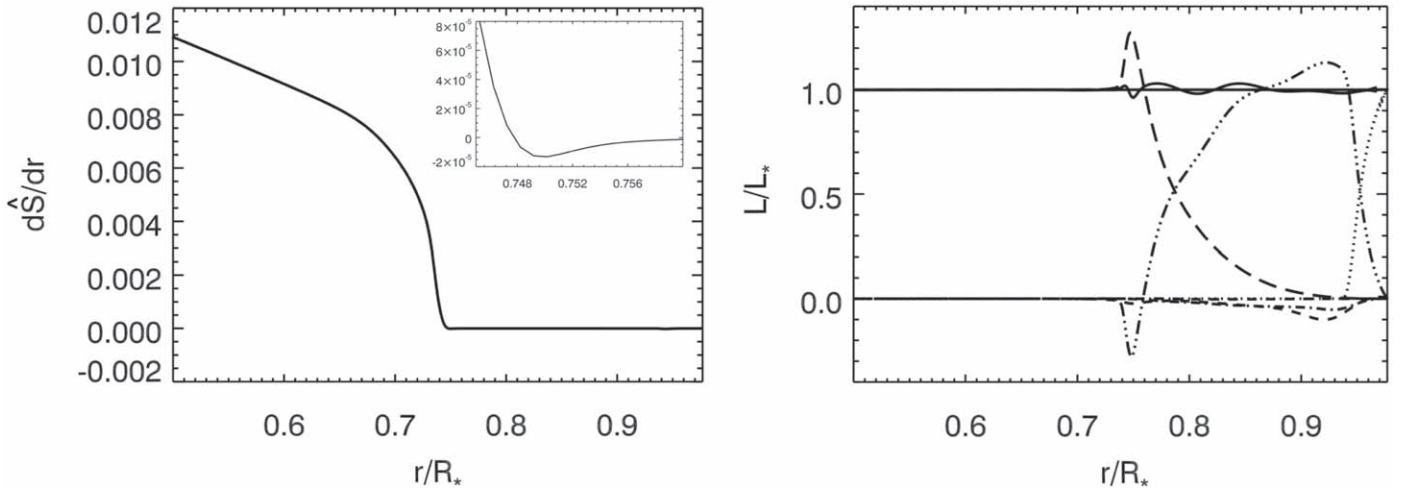


Figure 2. (a) Radial dependence of the mean entropy gradient for case M11R3m. The region of the tachocline is shown in the inset figure. (b) Time and horizontally averaged radial energy fluxes as luminosities (normalized to the star luminosity) for case M11R3m. The solid line is the total flux, the long-dashed line the radiative flux, the dashed–triple-dotted line the enthalpy flux, the dotted line the conductive entropy flux, the thick dashed–dotted line the kinetic energy, the dashed line the viscous diffusion flux, and the thick dashed line the Poynting flux.

have models for stellar masses 0.5, 0.7, 0.9, and 1.1 M_{\odot} and rotation rates ranging from 1/8 to 5 times the solar rotation rates. In keeping with the naming nomenclature of Brun et al. (2017), we name our model such as to indicate the mass of the star and its rotation rate. The models are named MA x rm, where “A” is the mass of the star and “r” the rotation rate of the star (in solar rotation rate). The index “x” indicates slow/antisolar ($x=s$) and prograde ($x=R$) DR models (except model M11R1m, which is also antisolar) and “m” stands for magnetism, to distinguish between the hydrodynamic progenitor published in 2017 and their MHD dynamo counterparts considered in this study.

The models have a numerical resolution of $(N_r, N_{\theta}, N_{\phi})$ $769 \times 256 \times 512$ except for few cases in the M09m and M11m series rotating at $\Omega_* = 3$ or $5\Omega_{\odot}$, where N_{θ} is 512 and N_{ϕ} is 1024.

In Figure 2 we show in (a) an example of the radial dependence of the entropy gradient, and in (b) the temporal and azimuthally averaged radial energy flux balance as luminosities for the model with 1.1 solar mass and 3 times the rotation rate of the Sun. We note the sharp increase of the stratification at the base of the convective envelope that is coherent with the stiff radiative interior found in main-sequence solar-like stars. Such a realistic interface, as opposed to an impenetrable wall, allows the convective motions to overshoot beyond the radius where the entropy gradient changes sign. By doing so they generate internal gravity waves and pump magnetic field. Because we are in this study mostly interested in the magnetic state of our simulation, we refer the reader to the following multidimensional studies of internal gravity wave generation in solar-like stars (Rogers & Glatzmaier 2006; Brun et al. 2011; Alvan et al. 2014, 2015). Turning to the radial flux balance, we note that the enthalpy flux (dashed–triple-dotted line) dominates energy transport in most of the convective envelope. The diffusive fluxes (radiative in the bottom half of the computational domain (long dashed) and unresolved near the top (dotted line)) carry the stellar luminosity at each end of the domain. We note an inward kinetic energy flux (dashed–dotted line) reaching about 10% of the star’s luminosity, as is common to find in stratified convection simulations. The Poynting and viscous fluxes account for less than 1% of the radial energy balance.

Finally, we note the negative enthalpy flux near the base of the convective envelope, which is compensated by a local increase of the radiative flux, such as to reach a satisfactory radial energy balance and thermal equilibrium.

2.3. G- and K-star Parametric Study

As indicated above, we initiate each of the 15 dynamo simulations from mature, relaxed hydrodynamics convective states and introduce a seed magnetic field in the convective envelope only. These hydrodynamical progenitors have been run long enough to reach a statistically stationary state in the convection zone and a well established rotation profile. They possess a genuinely established tachocline, defined as the transition between DR in the outer convective envelope to solid-body rotation in their stable radiative interior, leading to regions with strong shear (Spiegel & Zahn 1992). The tachocline plays an important role in the dynamo process of magnetic field generation in solar-like stars as reported in simulations performed by several authors (Glatzmaier 1985b; Browning et al. 2006; Racine et al. 2011; Masada et al. 2013; Lawson et al. 2015; Guerrero et al. 2016).

The main parameters of the models are listed in Tables 2 and 3. The density scale heights between the top and the base of the convection zone and between the top and the bottom of the model are defined as $N_{\hat{\rho}_{\text{bcz}}} = \ln(\hat{\rho}_{\text{out}}/\hat{\rho}_{\text{bcz}})$ and $N_{\hat{\rho}_{\text{tot}}} = \ln(\hat{\rho}_{\text{out}}/\hat{\rho}_{\text{in}})$. For the M05 model, $N_{\hat{\rho}_{\text{bcz}}} = 3.25$ and $N_{\hat{\rho}_{\text{tot}}} = 4.70$; M07 model, $N_{\hat{\rho}_{\text{bcz}}} = 3.48$ and $N_{\hat{\rho}_{\text{tot}}} = 5.78$; M09 model, $N_{\hat{\rho}_{\text{bcz}}} = 3.31$ and $N_{\hat{\rho}_{\text{tot}}} = 5.99$; and M11 model, $N_{\hat{\rho}_{\text{bcz}}} = 3.28$ and $N_{\hat{\rho}_{\text{tot}}} = 5.60$. The convective flows at the middle of the convective envelope vary from 5 m s^{-1} up to about 300 m s^{-1} in our sample, and the convective turnover time from 7 (case M11R1m) to 222 (case M05R3m) days. The surface DR between the equator and latitude 60° varies from -102 to $+278$ nHz in our sample, and we will study its maintenance in detail in Section 4.1. In the middle of the convection zone, the rms magnetic field typically varies from 1 to 70 G in our models. It is found to be maximum close to the bottom of the convective envelope, where the large-scale shear efficiently powers the dynamo, and the magnetic field can be

Table 1
Global Properties on the Main Sequence of the Four Stars Used in Our ASH Dynamo Models

Mass (M_{\odot})	Radius (R_{\odot})	L_* (L_{\odot})	T_{eff} (K)	Sp. T.	M_{bcz} (M_{\odot}, M_*)	r_{bcz} (R_{\odot}, R_*)	\hat{T}_{bcz} (K)	$\hat{\rho}_{\text{bcz}}$ (g cm^{-3})	$\Delta_{\text{cz}}\hat{\rho}$...	$\Delta_f\hat{\rho}$...	r_{bot} (R_*)	r_{top} (R_*)
0.5	0.44	0.046	4030	K7	0.18, 0.36	0.25,0.56	4.3×10^6	14.0	42	193	0.13	0.95
0.7	0.64	0.15	4500	K4/K5	0.079, 0.11	0.42,0.66	3.0×10^6	2.1	50	605	0.32	0.97
0.9	0.85	0.55	5390	G8	0.042, 0.046	0.59,0.69	2.6×10^6	0.51	67	1013	0.38	0.97
1.1	1.23	1.79	6030	G0	0.011, 0.010	0.92,0.75	1.6×10^6	0.048	81	830	0.5	0.97

Note. All the listed values were computed with the CESAM stellar evolution code (Morel 1997). We adopt $M_{\odot} = 1.989 \times 10^{33}$ g, $R_{\odot} = 6.9599 \times 10^{10}$ cm, and $L_{\odot} = 3.846 \times 10^{33}$ erg s $^{-1}$. The density ratios $\Delta_{\text{cz}}\hat{\rho}$ and $\Delta_f\hat{\rho}$ are evaluated by forming the ratio between the value of the density, respectively, at the base of the convection and the top of the domain and at the bottom and the top of the domain.

Table 2
Models Dimensional Characteristics

	Ω_* (Ω_{\odot})	\tilde{V}_r (m s^{-1})	\tilde{V}_{θ} (m s^{-1})	\tilde{V}_{ϕ} (m s^{-1})	$\Delta\Omega$ (nHz)	\tilde{B}_r (G)	\tilde{B}_{θ} (G)	\tilde{B}_{ϕ} (G)	τ_c (days)	τ_{ν} (yr)	τ_{κ} (yr)	τ_{η} (yr)
	MHD (HD)											
M05Sm	1/8	13.52	12.19	29.35	-23 (-24)	13.54	15.01	24.87	102.23	15.78	3.94	15.78
M05R1m	1	7.27	7.39	29.72	112 (129)	15.92	15.66	40.92	190.03	37.33	9.33	74.65
M05R3m	3	6.21	6.80	56.85	200 (85)	10.32	9.34	25.91	222.49	64.65	16.16	64.65
M05R5m	5	6.95	4.69	6.59	9 (146)	39.36	49.61	70.71	198.79	64.65	16.16	64.65
M07Sm	1/4	25.44	18.14	30.35	-53 (-32)	11.85	11.05	17.72	62.82	4.50	1.13	4.50
M07R1m	1	16.34	14.48	44.72	111 (120)	5.28	5.00	8.12	97.82	8.22	2.06	16.45
M07R3m	3	14.74	11.21	38.41	68 (187)	29.62	33.21	67.96	108.46	14.24	3.56	28.49
M07R5m	5	13.42	11.55	14.34	-2 (223)	35.85	42.33	54.71	119.11	18.39	4.60	18.39
M09Sm	1/2	53.51	36.80	48.98	-36 (-25)	1.70	1.66	1.68	35.83	2.72	0.68	2.72
M09R1m	1	38.74	35.32	68.55	102 (108)	2.32	2.44	3.17	49.50	3.86	0.97	7.72
M09R3m	3	30.61	32.42	148.70	265 (288)	1.07	1.07	1.93	62.64	6.67	1.67	6.67
M09R5m	5	27.94	19.74	56.43	76 (338)	20.33	19.82	47.02	68.62	7.18	1.80	7.18
M11R1m	1	130.77	93.56	140.61	-102 (-131)	12.69	11.81	13.06	16.67	1.46	0.37	2.93
M11R3m	3	90.23	81.57	272.53	278 (291)	4.49	4.66	6.83	24.17	2.54	0.63	2.54
M11R5m	5	88.50	61.74	88.73	109 (435)	18.63	18.48	32.93	24.63	2.62	0.65	3.27

Note. Characteristic velocities, differential rotation, magnetic fields, and timescales are listed, using averages over a small interval of $0.01R_*$ at the middle of the convective envelopes (unless stated otherwise). The differential rotation is taken between latitude 60° and the equator at the surface of the models (see Section 4.1). Likewise, the total magnetic flux is computed at the surface of the models and averaged over at least one magnetic cycle for the cyclic cases (see Section 5.4). The rms velocity and magnetic field are $\tilde{v} = (\tilde{v}_r^2 + \tilde{v}_{\theta}^2 + \tilde{v}_{\phi}^2)$ and $\tilde{B} = (\tilde{B}_r^2 + \tilde{B}_{\theta}^2 + \tilde{B}_{\phi}^2)$. Here, $\tau_c = D/\tilde{v}$ is the overturning convection time, and the dissipation timescales are defined as $\tau_x = D^2/x$ with $x \in [\nu, \kappa, \eta]$, where $D = r_{\text{top}} - r_{\text{bcz}}$ the thickness of the convective layer that differs for each mass bin.

stored in the tachocline close to the convective-radiative boundary.

Our sample of simulations were designed to operate in a relatively homogeneous turbulent Reynolds number regime, as seen in the first column of Table 3. The supercriticality degree can be characterized by the Rayleigh number achieved in our models, compared to a critical Rayleigh number for the onset of convection. Such a modified Rayleigh number was proposed by Takehiro et al. (2020) and is listed in column 6 of Table 3. All our models exhibit a Rayleigh number at least five times larger than the critical Rayleigh number. We have run these models as long as we could while maintaining a reasonable numerical cost to achieve the large parameter study presented here and while computing the models showing a magnetic cycle over several decades. In this study we use the Rossby number as a measure of the influence of rotation on the flows maintaining the DR as well as power dynamos. Several Rossby number definitions have been proposed in the community, and we have computed the fluid Rossby number Ro_f , the convective Rossby number Ro_c , and the stellar Rossby number Ro_s in Table 3. We refer the reader to Brun et al. (2017) and their Appendix for a more in-depth discussion of these various

definitions of the Rossby number. We will focus here on the fluid Rossby number Ro_f and note that the other two are related to Ro_f through a nearly linear relationship. The fluid Rossby number decreases with rotation rate and increases with mass and varies from 0.07 to 2.35 in our sample of models. This range nicely covers the transition from solar-like to antisolar DR regimes (the transition is nearly at $Ro_f \simeq 1$), and our smallest Rossby number (namely model M05R5m) is close to the expected fast rotators' saturation regime.

We now briefly present one representative cyclic dynamo solution before entering into a more detailed analysis of our dynamo simulations ensemble in Sections 4–6.

3. Overview of One Cyclic Dynamo Case

To illustrate the richness of the dynamo solutions discussed in this study, it is key to show how the subtle nonlinear interplay between convection, rotation, and turbulence leads to the generation of time-dependent complex magnetic fields. All 15 models discussed in detail in this study successfully generate and maintain a dynamo-generated magnetic field against ohmic dissipation.

Table 3
Model Characteristics Nondimensional Numbers

	Re	R_m	Pe	P_m	Ra [10^6]	Ra^*/Ra_c	Ta [10^6]	Ro_f	Ro_c	Ro_s	Ek [10^{-3}]	Λ [10^{-3}]
M05Sm	56.34	56.34	14.08	1	0.01	67.64	0.21	1.74	0.38	3.96	4.37	4.57
M05R1m	71.71	143.42	17.93	2	0.89	16.83	37.49	0.33	0.31	0.70	0.33	1.88
M05R3m	106.08	106.08	26.52	1	7.15	8.58	1012.05	0.15	0.17	0.23	0.06	0.14
M05R5m	106.08	106.08	29.68	1	7.60	5.69	2811.24	0.07	0.10	0.14	0.04	4.59
M07Sm	26.16	26.16	6.54	1	0.01	73.32	0.05	1.24	0.72	2.98	9.03	7.18
M07R1m	30.69	61.38	7.67	2	0.11	28.75	1.82	0.42	0.50	0.89	1.48	0.39
M07R3m	47.94	95.88	11.98	2	0.64	14.78	49.12	0.16	0.23	0.30	0.29	8.40
M07R5m	56.36	56.36	14.09	1	1.59	8.91	227.44	0.09	0.17	0.18	0.13	8.68
M09Sm	27.69	27.69	6.92	1	0.01	54.09	0.05	1.28	0.74	3.02	8.98	0.12
M09R1m	28.48	56.96	7.12	2	0.04	24.71	0.40	0.68	0.66	1.51	3.16	0.14
M09R3m	38.90	38.90	9.73	1	0.33	11.02	10.79	0.27	0.35	0.50	0.61	0.01
M09R5m	38.21	38.21	9.55	1	0.36	7.00	34.70	0.10	0.20	0.30	0.34	5.33
M11R1m	32.06	64.12	8.02	2	0.01	47.17	0.06	1.38	0.78	3.30	8.33	11.36
M11R3m	38.31	38.31	9.58	1	0.10	17.16	1.56	0.54	0.50	1.10	1.60	0.51
M11R5m	38.81	38.81	9.70	1	0.13	6.87	4.62	0.27	0.34	0.66	0.93	13.06

Note. All quantities listed have been averaged over a small interval of $0.01R_*$ at the middle of the convective envelopes. $Re = \bar{v}D/\nu$ is the Reynolds number. The Prandtl number $Pr = \nu/\kappa = 1/4$ in all cases. $P_m = \nu/\eta$ is the magnetic Prandtl number, $R_m = ReP_m$ is the magnetic Reynolds number, and $Pe = RePr$ is the Péclet number. $Ra = (-\partial\hat{\rho}/\partial S)\Delta SgD^3/\hat{\rho}\nu\kappa$ is the Rayleigh number, and Ra^*/Ra_c is the modified Rayleigh number as computed by Takehiro et al. (2020). $Ta = 4\Omega_*^2 D^4/\nu^2$ is the Taylor number. We also list three Rossby numbers: the fluid Rossby number $Ro_f = \tilde{\omega}/2\Omega_*$, the convective Rossby number $Ro_c = \sqrt{Ra/TaPr}$, and the stellar Rossby number $Ro_s = P_{rot}/\tau_c^{CS}$. The latter is useful for comparison with observationally derived Rossby numbers. For Ro_s we have therefore considered the empirical convective turnover time derived by Cranmer & Saar (2011), which is $\tau_c^{CS} = 314.24 \exp\left[-\frac{T_{eff}}{1952.5 \text{ K}} - \left(\frac{T_{eff}}{6250 \text{ K}}\right)^{18}\right] + 0.002$ days. We note that it correlates well with our fluid Rossby number and find $Ro_s \simeq 2.26Ro_f$. The Ekman number is defined as $Ek = \nu/(\Omega_* D^2)$ and the Elsässer number as $\Lambda = \tilde{B}^2/8\pi\hat{\rho}D\bar{v}\Omega_*$.

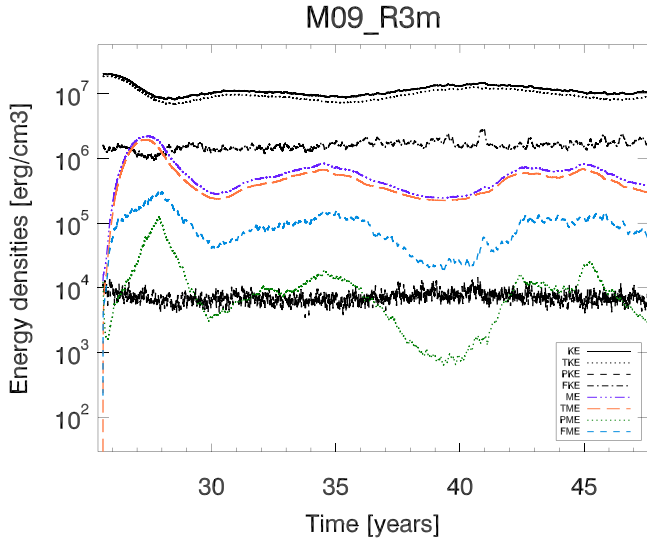


Figure 3. Temporal evolution in case M09R3m of the kinetic (KE) and magnetic (ME) energies. We also show their axisymmetric toroidal TKE, TME, and poloidal PKE and PME components and their fluctuating components FKE and FME. We note the rise over about 500 days of ME just after having introduced a weak seed field. Then follows a modulation of ME with a 9 yr period. Case M09R3m is indeed one of our cyclic cases (see also Figure 4).

We defer the systematic comparison between all 15 models to the next sections and focus here on the representative case M09R3m. Indeed, M09R3m is in an intermediate Rossby number regime ($Ro_f = 0.27$) and therefore lies in the middle of our sample of models. The temporal evolution of kinetic and magnetic energies is shown in Figure 3. The magnetic energies first rise very fast to then saturate after about 1000 days in this case, and exhibit long-term oscillations over a decadal

timescale reminiscent of a solar-like magnetic cycle. All components of the magnetic energy (toroidal, poloidal, and fluctuating) oscillate in phase in this model. The mean toroidal kinetic energy also presents oscillation of the same amplitude, albeit anticorrelated with the magnetic ones. These energy trends are similar to the ones found in the magnetic cycles obtained with the EULAG code in Strugarek et al. (2018, see their Figure 3) and points toward a similar dynamo mechanism involving a strong feedback of the magnetic field on the DR within the convective envelope. We will perform a detailed analysis of this mechanism in Section 5. Here, we first illustrate the dynamics of the dynamo achieved in model M09R3m in Figure 4. The top row shows the 3D structure of our model by means of a potential-field extrapolation outside our computational domain at three different instances covering a magnetic reversal. We see that the field at the south pole changes from blue to black, showing the polarity reversal. The strong toroidal field at the base of the convective envelope can be seen through the transparency. In the leftmost panel, this deep wreath is mainly blue (westward oriented). Its polarity is reversed in the rightmost panel (red, eastward oriented), showing that the polarity reversal takes places over the full convective domain. The subsequent rows show spherical slices of B_ϕ at the base of the convective envelope (second row), B_r at the top of the domain (third row), entropy fluctuations (S') at the top of the domain (fourth row), and enstrophy $|\nabla \times \mathbf{v}|^2$ (last row). We recover in the second row the magnetic wreath located at the base of the convective envelope and at midlatitude that changes polarity as the cycle progresses. The toroidal field reaches high values of up to 1.5×10^4 G, with a strong temporal variation, as seen in the middle panel during the reversal. The surface radial field (third row) reaches values of about 100 G and exhibits a complex topology, mixing dipolar and quadrupolar

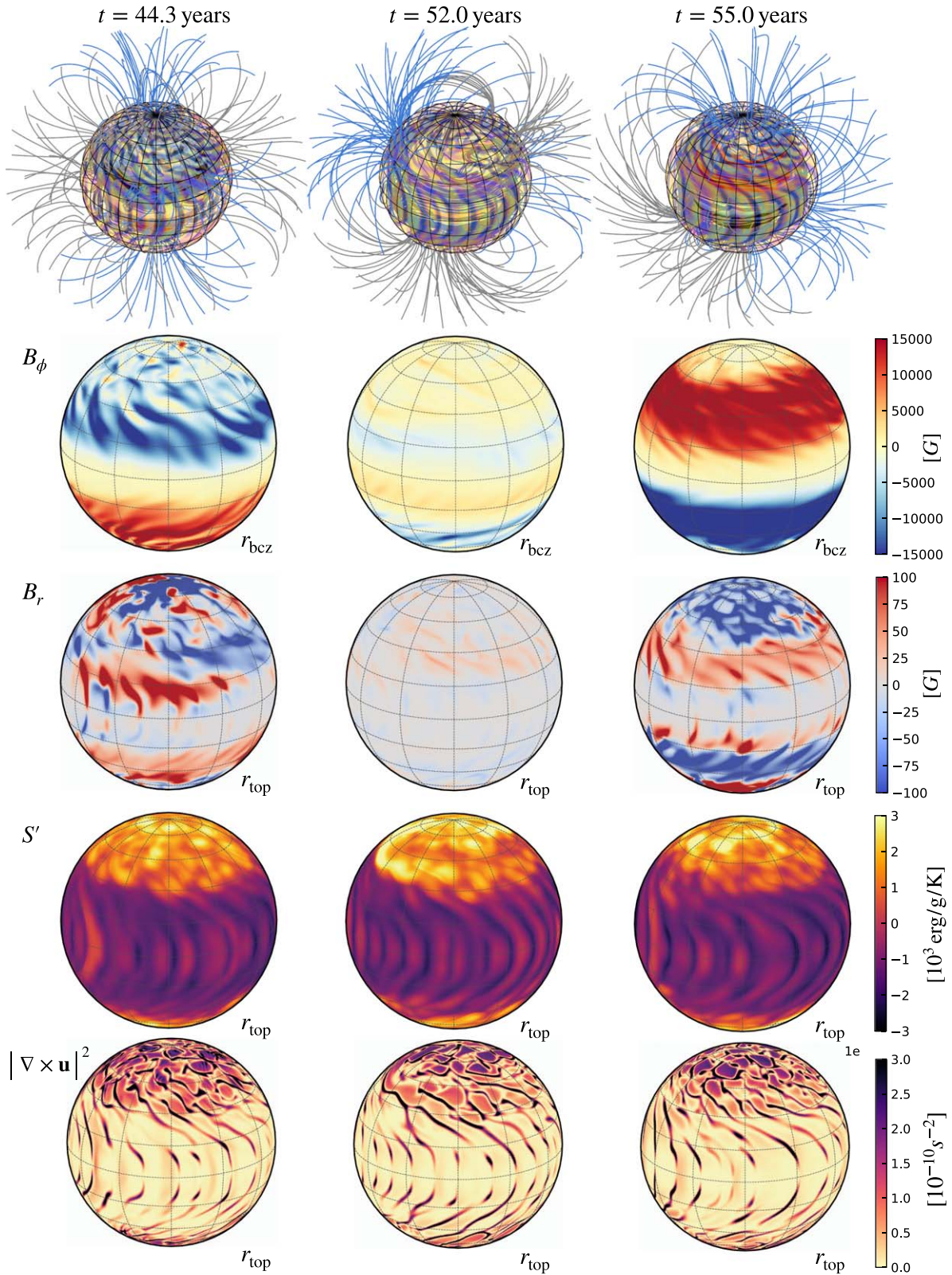


Figure 4. Temporal evolution of a magnetic cycle for case M09R3m, taken at three different instances during one reversal. The upper row shows a 3D potential extrapolation of the modeled magnetic field, with blue lines denoting field lines oriented outward and black lines oriented inward. Behind a semitransparent representation, the radial velocity is close to the surface, while deeper below, the magnetic wreaths are shown by red (oriented eastward) and blue (oriented westward) lines. The second row shows the azimuthal field at the bottom of the convection zone, and the third row the radial field at the top of the domain. The fourth row shows the entropy fluctuations at the top of the domain, and the lowest row the entropy at the same depth.

symmetries. We see again here that both fields oscillate in phase and reach a minimum in the midst of the magnetic reversal (middle panels). Finally, the two last rows show the thermal (entropy) fluctuations and the vortical motions (enstrophy) in our simulations. The first striking aspect is that these two quantities vary very little along the magnetic cycle. Indeed, the magnetic field modifies the large-scale motions and the average convective state in our models. Yet the magnetic cycles (when present) show little imprint on the convective flows themselves and mainly act on the mean flows (see Section 4.1). The specific entropy fluctuations have two distinctive features. First, a mean pole-to-equator contrast is well established in the model, with higher entropy fluctuations at the poles. Such contrast is expected in models with a solar-like DR (Brun & Toomre 2002) and can be generally related to the pressure field required to drive the observed meridional flow. Second, patterns in S' are imprinted by the nonaxisymmetric convective motions themselves, which are also recognizable in the enstrophy in the lower panel. The enstrophy is concentrated at the boundaries of the so-called banana cells at low latitude (Miesch et al. 2000) and is distributed between convective cell centers and boundaries at high latitude.

We now turn to the detailed analysis of the large-scale flows (Section 4), magnetic properties (Section 5), and energetic balances (Section 6) achieved in the 15 models. The reader mostly interested in the astrophysical consequences of our study may consider going directly to Section 7 for a summary.

4. Large-scale Flows in the Models

In this section, we analyze the DR profiles of the models including both a stable subadiabatic layer and magnetic field self-consistently generated by dynamo action. The aim of the study is to compare the DR profiles of the hydrodynamical and MHD models. We confirm our preliminary results (Varela et al. 2016) and those of others (Karak et al. 2015; Guerrero et al. 2016; Viviani et al. 2018) that the presence of magnetic fields leads to different trends for the DR with stellar rotation rate and mass when compared to their hydrodynamical counterpart. We further discuss how the meridional circulation is impacted by the presence of a magnetic field and discuss the main mechanisms acting to redistribute angular momentum within the convective shell. We also observe torsional oscillations in our set of dynamo simulations but delay their discussion to Section 5.3.

4.1. Differential Rotation Profiles as a Function of Rossby Number

We analyze the DR of the simulations that results from the angular momentum redistribution occurring mostly in the convection zone. The panels of Figure 5 show a meridional cut of the axisymmetric DR averaged over 10 overturning convective times, defined as $\tau_c = \int_{r_{\text{bcz}}}^{r_{\text{top}}} dr / \tilde{v}_r$ (see Table 2).

We observe that for the simulations M05Sm, M07Sm, M09Sm, and M11R1m, there is an antisolar DR, with the poles rotating faster than the equator, like their hydrodynamical counterparts (see Figure 6 and also Brun et al. 2017). The cases rotating at an intermediate rotation rate show a solar-like DR. Finally, the cases rotating the fastest (R5 series) show almost no DR (in particular for cases M05Sm and M07Sm). This constitutes a big difference with their hydrodynamical counterpart cases. The magnetic field here had a major impact, with

almost solid-body rotation imposed throughout the convective envelope. There is little asymmetry in the profiles between the northern and southern hemispheres, as expected when the average is performed over an interval long enough with respect to the convective overturning time (except for M05Sm for which the rotational constraint is the weakest and the longitudinal average less meaningful). Figure 6 also displays radial cuts of the rotation for the MHD cases (blue lines) and hydrodynamic progenitor cases (gray lines). In cases rotating 1, 3, and 5 times the solar rotation rate (bottom three rows), the velocity range in latitude (different styles of line) is generally reduced in the presence of a magnetic field. This effect is observed to be stronger as the rotation rate increases. Conversely, the effect of the magnetic field is mild for the slowly rotating cases (upper row), except on the slowly rotating case M11R1m, which still shows some degree of magnetic feedback on its DR. As one may expect, the radial gradient of the DR near the tachocline is generally weaker in all MHD simulations compared with hydrodynamic progenitors. This points to a magnetic feedback of the dynamo field on the DR itself, a feedback that is observed to strengthen as the rotation rate increases.

We have calculated the surface latitudinal DR $\Delta\Omega$ for each model, defined as the difference between the equator and 60° latitude. A positive value thus denotes a solar-like DR and a negative value an antisolar DR. We report these values for the magnetic cases as well as the hydrodynamic progenitors in Table 2 (fourth column).

The DR of our sample spans a range between -102 and $+278$ nHz, with some fast-rotating models presenting an extremely weak DR, like M05R5m with $\Delta\Omega = 9$ nHz. We find that the absolute DR generally weakens in MHD models compared to their hydrodynamic progenitors, as expected from the radial profiles shown in Figure 6. This is particularly striking for fast rotators such as M09R5m, which goes from 338 nHz in hydro to 76 nHz in MHD.

We investigate in Figure 7 the DR trends with respect to the rotation rate (left panel) and rotation period (right panel). The DR of the hydrodynamic progenitors and of the MHD cases are respectively shown in small semitransparent and large opaque symbols. The shape of the symbol labels the rotation of the model, and the color the mass of the modeled star, as indicated in the legend. In the right panel, we compare the model DR to the DR in the Kepler sample obtained by Reinhold & Gizon (2015) (shown as black dots). The dotted lines correspond to their estimated observational detection limits. We first note that the absolute value of our DRs agrees well with the observed values. In addition, the DR range in our sample increases as the rotation period decreases, like what is observed in the Kepler satellite sample. Several of our models nevertheless lie outside the observed values: the three antisolar DRs on the right (triangles) and two of our fast-rotating models. Several reasons can explain this discrepancy. Slowly rotating stars could produce very few starspots or even no starspots at all (see, for instance, van Saders et al. 2019), making their DR impossible to detect with photometry. Another possibility is that they lie outside the presently detectable limit with the Kepler data, due to their long rotational period (up to about 200 days for our most slowly rotating model). Finally, the two fast-rotating models (M05R5m and M07R5m) show very weak DRs due to magnetic feedback, which are outside the detection limits of Kepler (dotted black lines).

The left panel of Figure 7 shows the DR trend with the rotation rate. Using only the hydrodynamic progenitors, we

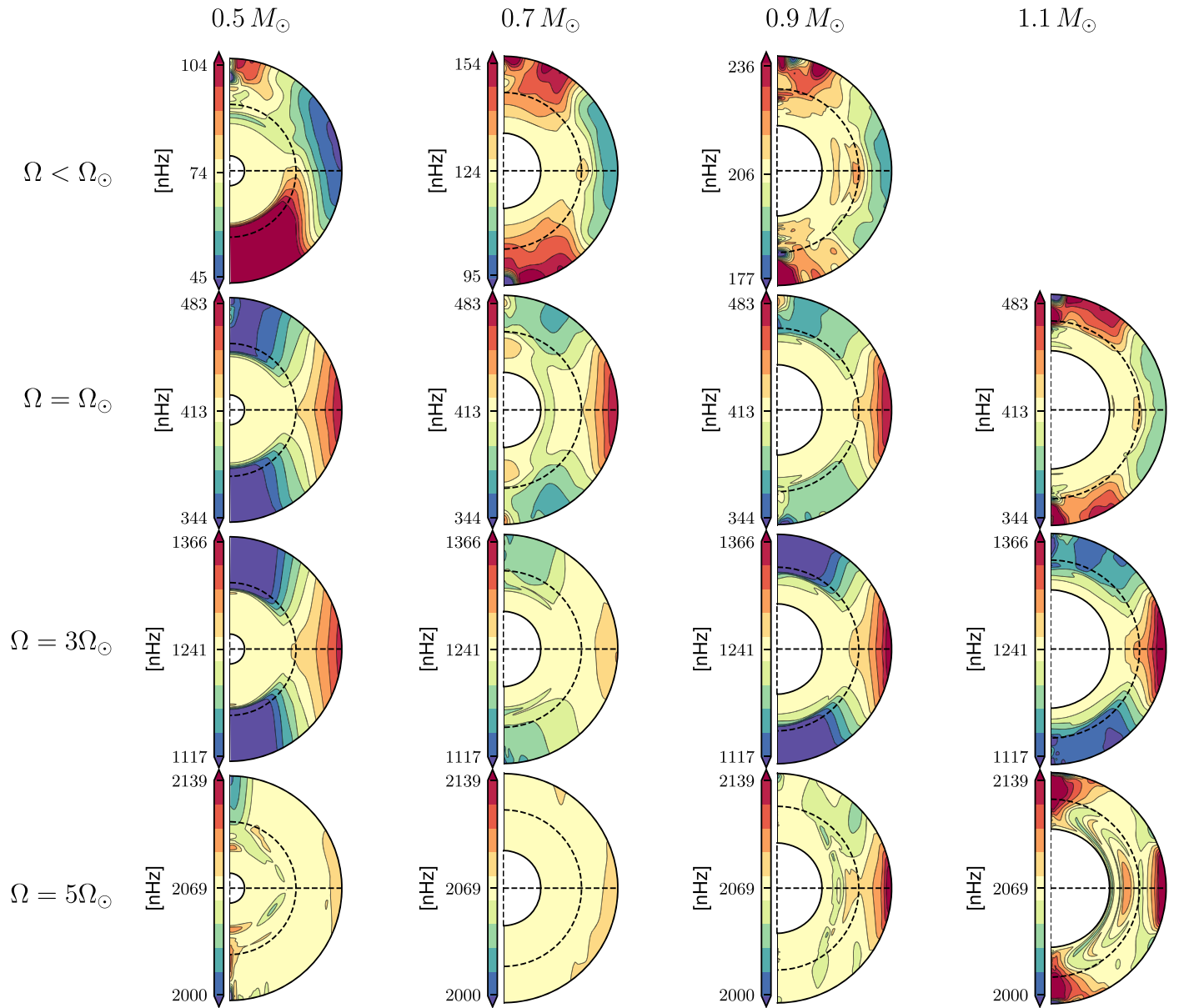


Figure 5. Temporal and longitudinal averages of the angular velocity profiles over 10 convective overturning times ($10 \tau_c$) in our suite of models. Prograde flows are in reddish tones and retrograde ones in bluish tones. In each panel, the dashed semicircle represents the base of the convective envelope and the dashed horizontal line the equator.

previously showed that the DR scales as $\Omega^{0.66}$ (Brun et al. 2017). Blindly trying to fit such a power law to the MHD sample, we find that the exponent reduces to $\Omega^{0.46}$. This weaker dependency is expected due to the magnetic feedback on the DR through the Lorentz force. It also agrees better with the observational trends, which are still quite uncertain and were found to vary from 0.2 (Balona & Abedigamba 2016 for G stars), 0.3 (Reinhold et al. 2013 for cool stars), to even 0.7 (Donahue et al. 1996 for F-K stars). Looking more closely at our sample on the left panel of Figure 7, it clearly appears that a power-law fit is a poor representation of the DR in our sample. Rather, we see that $\Delta\Omega$ increases with Ω for slow rotators, while it dramatically drops for fast rotators due to the magnetic feedback. Following Saar (2011), we recast in Figure 8 the DR trend in terms of relative DR $\Delta\Omega/\Omega$ with respect to the fluid Rossby number Ro_f (for the different definitions of Rossby number used in this work, see the caption of Table 3 or the Appendix A of Brun et al. 2017). We

find a trend that is very similar to the observational trend reported by Saar (2011) (shown by the dashed line in Figure 8): $\Delta\Omega/\Omega$ is roughly constant for inverse Rossby numbers lower than a certain threshold (here $Ro_f^{-1} \lesssim 5$), and it drops for fast rotators as $\Delta\Omega/\Omega \propto Ro_f^p$. Saar (2011) proposed that $p = 2$, but here our sample agrees with a somewhat large range $p \in [2, 6]$. Additional models with even higher turbulence level are required to confirm the exact amplitude of the drop in DR contrast found in the fast-rotating cases. Finally, our sample also shows some hint of an increase of $\Delta\Omega/\Omega$ at large Rossby numbers, which is outside the observable constraints for now. It would be interesting to search observationally for candidate solar-like stars possibly possessing such antisolar rotation states.

In Brun et al. (2017), we have proposed that the DR could follow two power laws with respect to the Rossby number and the stellar mass. Here, we find that the DR is weakened at high Rossby number, and therefore we do not recover a simple

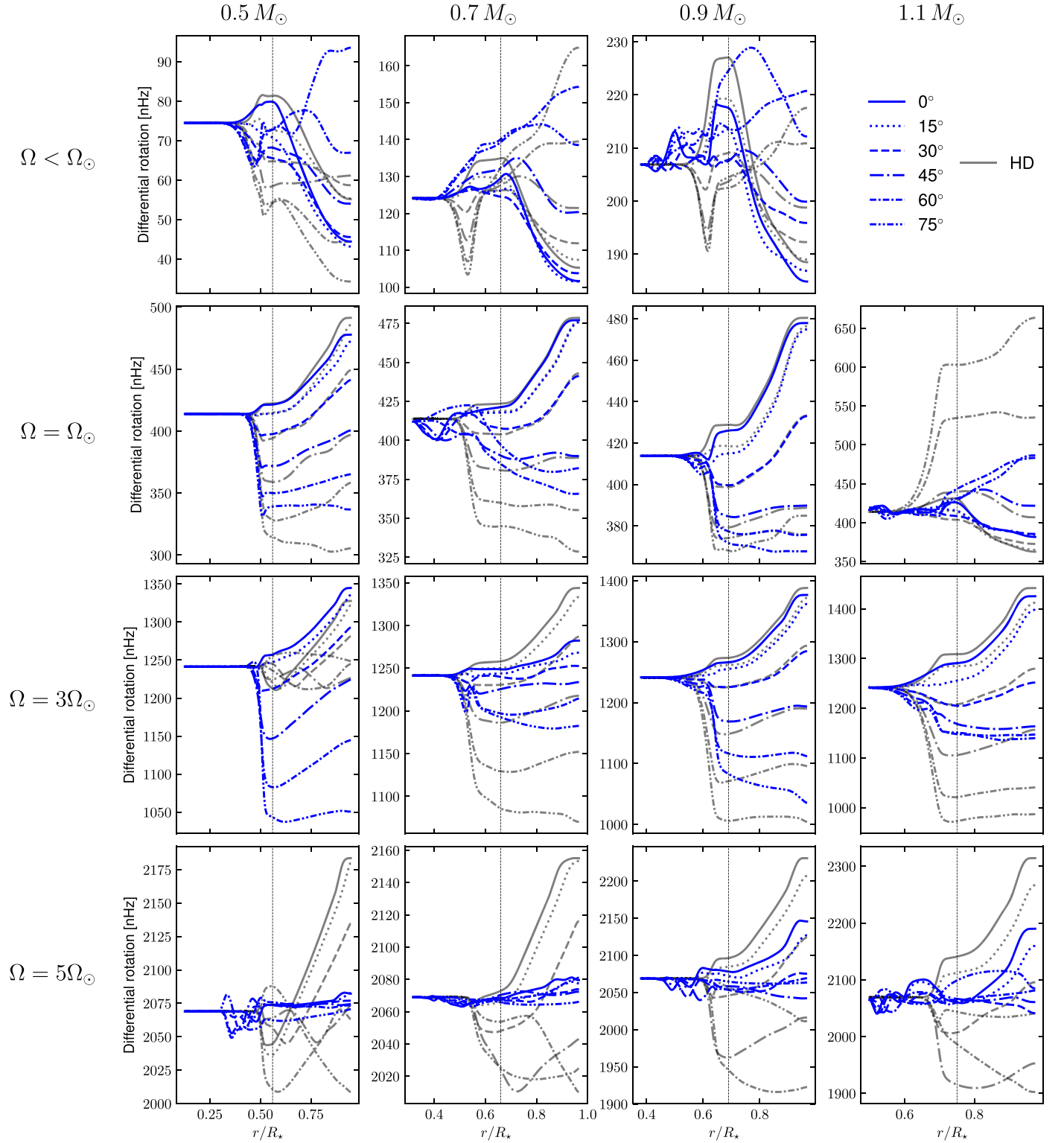


Figure 6. Radial cuts of the temporal- and longitudinal-averaged angular velocity from the equator to 75° latitude every 15° (black lines are for the hydrodynamical cases and the blue lines the MHD/dynamo cases). The solid vertical line in each panel shows the bottom of the convective layer.

power-law trend, as we saw in Figure 7. We can nevertheless attempt to fit such a combined power law on a subsample of our models, excluding the fast-rotating case but retaining the slow rotators. We obtain in this way

$$\Delta\Omega = 107R_{0f}^{-0.73 \pm 0.13} \frac{M_*^{1.93 \pm 0.42}}{M_{\odot}} \text{ nHz (HD)}, \quad (7)$$

$$\Delta\Omega = 84R_{0f}^{-0.40 \pm 0.20} \frac{M_*^{0.78 \pm 0.62}}{M_{\odot}} \text{ nHz (MHD)}. \quad (8)$$

In the MHD case, we find again that the DR is less sensitive to both the Rossby number and the stellar mass. The power-law fit is nevertheless questionable here, as the range covered by our Rossby numbers and masses is quite small. We have

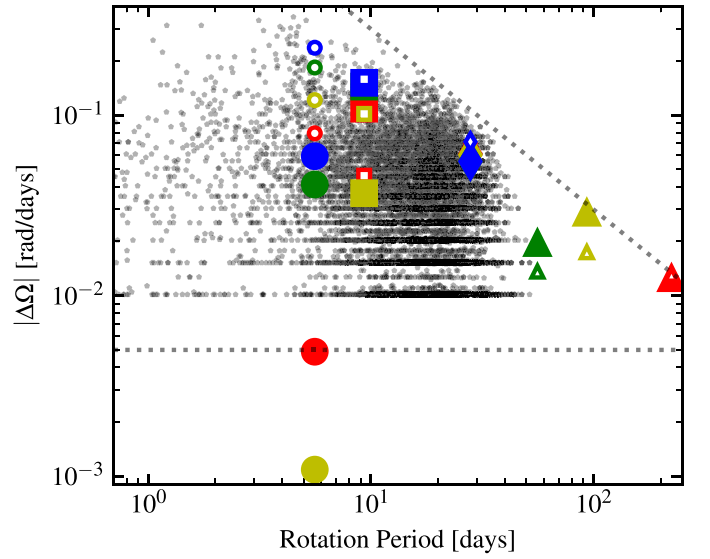
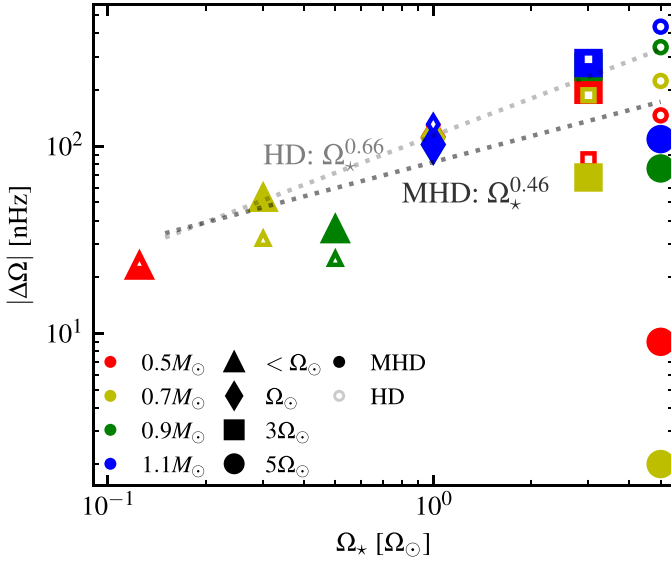


Figure 7. Absolute value of the differential rotation between the equator and 60° latitude vs. rotation rate (left panel) and rotation period (right panel). The symbols denote the rotation rate of the model and the color the mass of the modeled star, as shown in the legend. MHD models are shown by the large plain symbols, and the hydrodynamic progenitors by the smaller open ones. On the right panel, the differential rotation in the Kepler sample obtained by Reinhold & Gizon (2015) is shown as black dots and the observational detection limit by the two dotted black lines.

nevertheless included the results of the fit here to compare with the purely hydrodynamic case (Brun et al. 2017). We can conclude here that the clear trend in stellar mass and effective temperature found in the hydrodynamic study (Brun et al. 2017) is less significant when magnetism is taken into account, but overall we see a better agreement with observations of the dynamo models compared to their hydrodynamical progenitors.

The MHD simulations therefore show that the magnetic field changes the angular momentum redistribution, especially for fast-rotating stars. In the next section, we perform a detailed analysis of this balance for four representative models.

4.2. Angular Momentum Transfer

We can better understand how the DR profiles are achieved in the dynamo models by identifying the main physical processes responsible for redistributing angular momentum within rotating convective shells. Our choice of stress-free and potential-field BCs at the top and stress-free and perfect conductor BCs at the bottom of the computational domain have the advantage that no net external torque is applied, and thus angular momentum is conserved. We can assess the transport of angular momentum by considering the mean radial (\mathcal{F}_r) and latitudinal (\mathcal{F}_θ) angular momentum fluxes, applying the procedure used in Brun et al. (2004). Starting from the ϕ component of the momentum equation expressed in conservative form and averaged in time and longitude:

$$\frac{1}{r^2} \frac{\partial(r^2 \mathcal{F}_r)}{\partial r} + \frac{1}{r \sin \theta} \frac{\partial(\sin \theta \mathcal{F}_\theta)}{\partial \theta} = 0, \quad (9)$$

involving the mean radial angular momentum flux

$$\mathcal{F}_r = \hat{\rho} r \sin \theta \left[-\nu r \frac{\partial}{\partial r} \left(\frac{\hat{v}}{r} \right) + \widehat{v'_r v'_\phi} + \hat{v}_r (\hat{v}_\phi + \Omega r \sin \theta) - \frac{1}{4\pi \hat{\rho}} \widehat{B'_r B'_\phi} - \frac{1}{4\pi \hat{\rho}} \widehat{B_r B_\phi} \right], \quad (10)$$

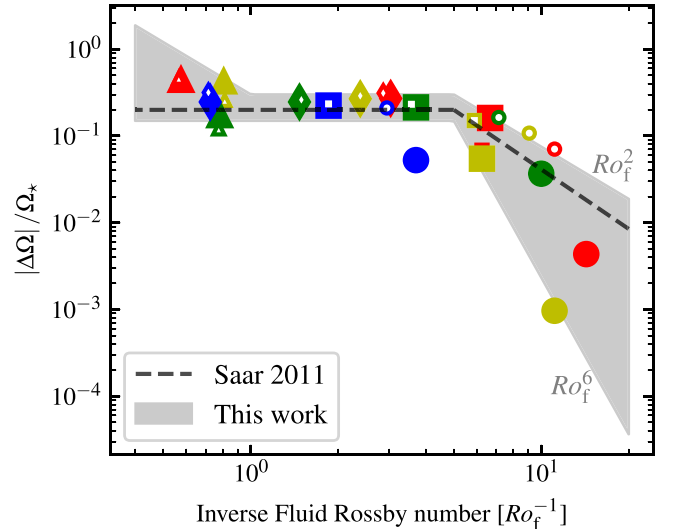


Figure 8. Relative differential rotation between the equator and 60° latitude as a function of the fluid Rossby number. The symbols shape and color are the same as in Figure 7. The trend found in the MHD sample is highlighted by the gray area, and the observational trend reported by Saar (2011) is shown by the dashed black line.

and the mean latitudinal angular momentum flux

$$\mathcal{F}_\theta = \hat{\rho} r \sin \theta \left[-\nu \frac{\sin \theta}{r} \frac{\partial}{\partial \theta} \left(\frac{\hat{v}_\phi}{\sin \theta} \right) + \widehat{v'_\theta v'_\phi} + \hat{v}_\theta (\hat{v}_\phi + \Omega r \sin \theta) - \frac{1}{4\pi \hat{\rho}} \widehat{B'_\theta B'_\phi} - \frac{1}{4\pi \hat{\rho}} \widehat{B_\theta B_\phi} \right]. \quad (11)$$

In these equations, the terms on the right-hand side represent, for both fluxes, contributions respectively from viscous diffusion (which we denote as $\mathcal{F}_r^{\text{VD}}$ and $\mathcal{F}_\theta^{\text{VD}}$), Reynolds stresses ($\mathcal{F}_r^{\text{RS}}$ and $\mathcal{F}_\theta^{\text{RS}}$), meridional circulation ($\mathcal{F}_r^{\text{MC}}$ and $\mathcal{F}_\theta^{\text{MC}}$), Maxwell stresses ($\mathcal{F}_r^{\text{MS}}$ and $\mathcal{F}_\theta^{\text{MS}}$), and large-scale magnetic torques ($\mathcal{F}_r^{\text{MT}}$ and $\mathcal{F}_\theta^{\text{MT}}$). The Reynolds stresses are

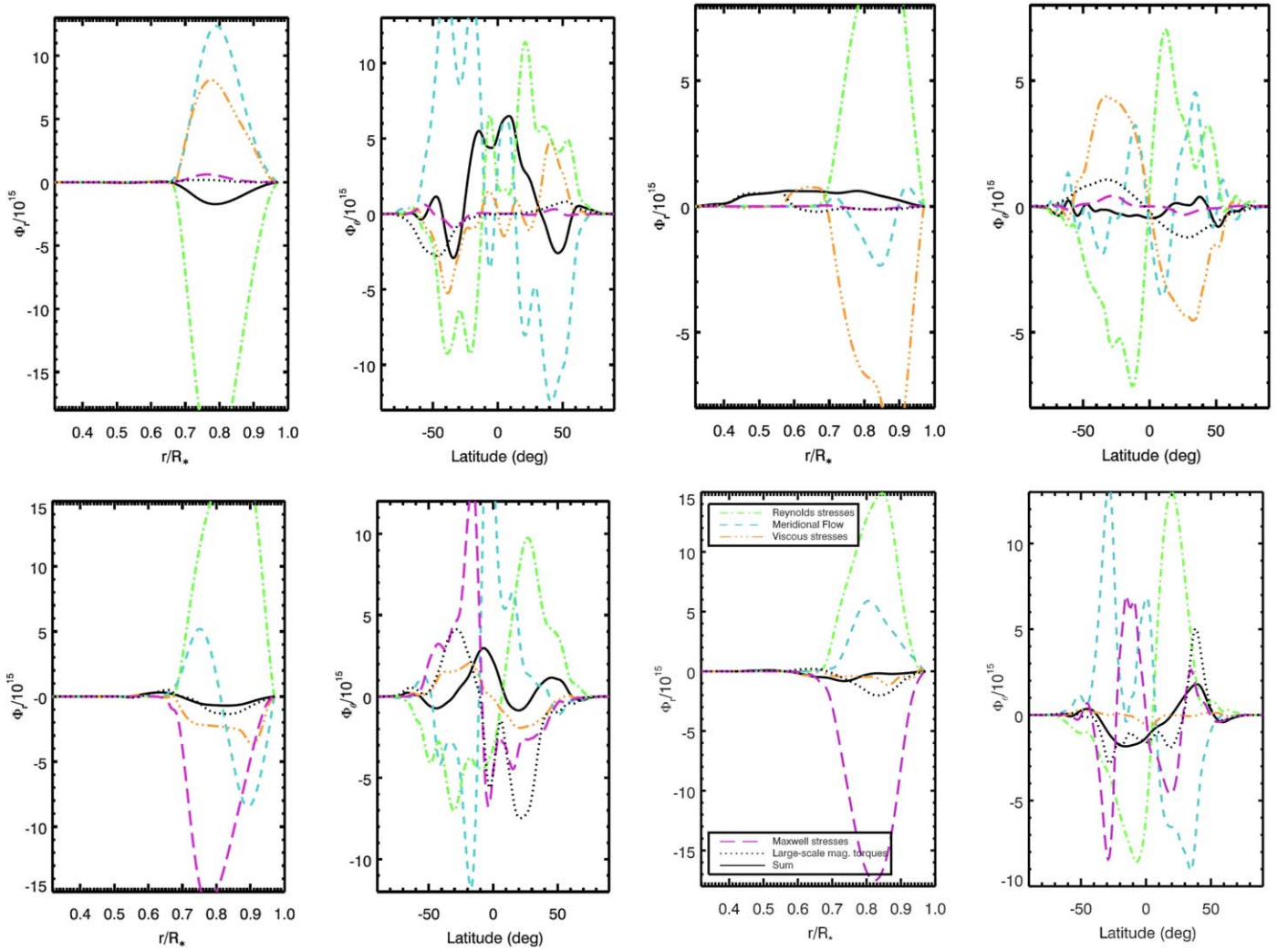


Figure 9. Angular momentum transport in the M07 case series. We display cases M07Sm (left) and M07R1m (right) in the top row and M07R3m (left) and M07R5m (right) in the bottom row. For each model, the radial (left) and latitudinal (right) angular momentum balance are shown, with Reynolds stress contribution shown as green dashed–dotted lines, viscous stresses as dashed–triple-dotted yellow lines, meridional circulation as dashed cyan lines, Maxwell stresses as long dashed magenta lines, the large-scale magnetic torques as a black dotted line and the sum of all contributions as a solid black line. We note that a very good angular momentum balance is achieved in most models in both directions with the sum being close to zero.

linked to correlations of the fluctuating velocity components coming from organized tilts within the convective structures, especially in the downflow plumes. Likewise, the Maxwell stresses are associated with correlations of the fluctuating magnetic field components due to the twist and tilt of the dynamo-generated magnetic structures.

In Figure 9 we show the components of \mathcal{F}_r and \mathcal{F}_θ for the M07 case series, having integrated over colatitude and radius as follows:

$$\begin{aligned} \Phi_r(r) &= \int_0^\pi \mathcal{F}_r(r, \theta) r^2 \sin \theta d\theta, \\ \Phi_\theta(\theta) &= \int_{r_{\text{bot}}}^{r_{\text{top}}} \mathcal{F}_\theta(r, \theta) r \sin \theta dr. \end{aligned} \quad (12)$$

Thus, Φ_r represents the net angular momentum flux through horizontal shells at different radii and Φ_θ represents the net flux through cones at different latitudes. This representation is helpful in assessing the direction and amplitude of angular momentum transport within the computational domain by each component of \mathcal{F}_r and \mathcal{F}_θ .

For each of the four cases, we display Φ_r on the left panel and Φ_θ on the right panel, both normalized by R_*^2 . Turning to the radial angular momentum transfer, we first note a very good overall radial balance. We find that the Reynolds stresses (green dashed–dotted curves) transport angular momentum outward in all the low Rossby number models. By contrast, M07S, the slowly rotating case, has the Reynolds stresses transporting angular momentum inward. The viscous diffusion and Maxwell stresses oppose this transport, tending to rigidify the rotation state in the radial direction. The meridional circulation has one large cell per hemisphere for the M07Sm case (see Section 4.3). It opposes the Reynolds stresses, but as the rotation rate increases and the Maxwell stresses gain in amplitude, it changes in profiles and direction to yield a radial balance of angular momentum, from the angular momentum equation. Note that the mean large-scale magnetic torques (black dotted line) have little influence on the overall radial angular momentum balance.

Considering now Φ_θ , we can assess the balance of latitudinal angular momentum transport. We first notice that the Reynolds stresses (green curves) are systematically equatorward in both

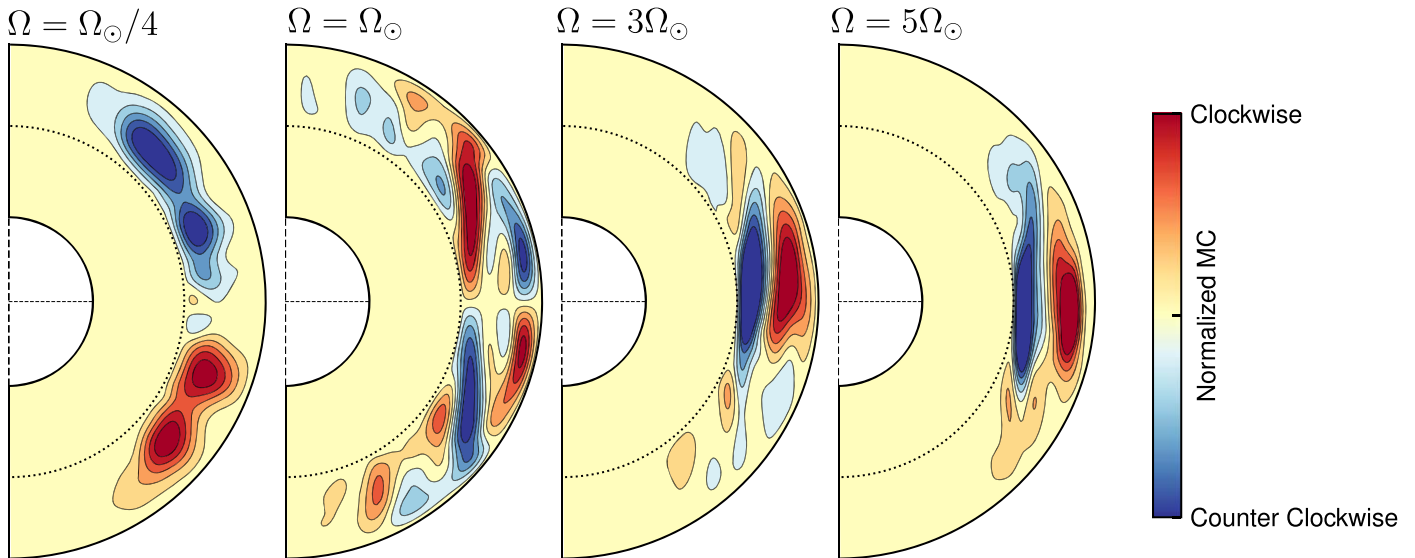


Figure 10. Meridional flows in M07m case series. The contours are normalized and denote clockwise (red) and anticlockwise (blue) circulations.

hemisphere (positive in the northern hemisphere and negative in the southern one). Because most cases exhibit a very good latitudinal balance, as demonstrated by the solid black curve, these Reynolds stresses must be nicely counterbalanced. A quick survey of the right panels for all four models indicates that many contributors act depending on the Rossby number of the simulations. For the slowly rotating case (upper-left corner), we see that it is mostly the meridional circulation (cyan dashed curve) that does most of the work (we defer the reader to Section 4.3 for a discussion of the meridional circulation patterns in the various dynamo cases). By contrast, magnetic terms do not play much role in the case of M07Sm. For M07R1m (right-top corner) it is now the viscous diffusion that plays that role of opposing the Reynolds stresses. For that case, the meridional circulation is not doing much, but we do see a 20% contribution of the large-scale magnetic torques, the Maxwell stresses being still weak. As the Rossby number decreases and the dynamo action becomes more intense, we see that the magnetic terms start influencing the latitudinal angular momentum transport more and more, tending to oppose the Reynolds stresses. It is particularly noticeable for the M07R3m case (bottom-left corner), helped by the large-scale magnetic torques. In that case the meridional circulation is somewhat helping the Reynolds stresses, notably at low latitudes near the equator. For the M07R5m case, the story becomes less clear; except for the Reynolds stresses, all terms fluctuate and sometimes oppose or reinforce the turbulent stresses. Maxwell stresses still play an important role as does the meridional circulation. In that model, the DR has been so significantly quenched by dynamo action that it is not surprising the trends are less clear and systematic. In summary, in most cases the transport of angular momentum by Reynolds stresses are opposed by a combination of meridional circulation, viscous stresses, and Maxwell stresses.

4.3. Meridional Circulation Profiles

The meridional flow patterns are also affected by the presence of magnetism in our set of models, especially for the fast-rotating cases. We immediately note that the meridional

circulation is indirectly modified by magnetism (as will be made clear in Section 6.2). Indeed, magnetic stresses play a negligible role in setting the meridional flows in our models, and the differences we observe compared to the hydrodynamical counterparts originate from changes in the DR (see, e.g., Passos & Charbonneau 2014).

We illustrate the meridional flow pattern achieved in the M07m set of simulations in Figure 10. The slow-rotating case (first panel) is very similar to its hydrodynamic progenitor, with a well-defined circulation cell in each hemisphere. Both cells circulate from the equator to the pole at the surface and from the pole to the equator at the base of the convective envelope. The second model rotating at the solar rate (second panel) is also similar to its hydrodynamical progenitor and shows a more complex circulation profile. These are consistent with previous numerical experiments by, e.g., Karak et al. (2015). It consists of stacked cells elongated along the rotation axis outside the tangent cylinder and two counterrotating cells in each hemisphere at high latitude. Finally, the fast-rotating models (third and fourth panels) exhibit a peculiar meridional circulation pattern concentrated at the equator, with two stacked transequatorial cells (see, e.g., Simitiev & Busse 2009). These profiles can be understood as follows. In these models, the DR is strongly quenched by magnetic feedback as seen in the previous section. In particular, the radial shear of DR vanishes at the equator as seen in Figure 6. As a result, gyroscoping pumping (Miesch et al. 2006; McIntyre 2007; Featherstone & Miesch 2015) dramatically weakens along the equator, and the resulting meridional circulation is both very weak (this can be seen in the drop of meridional flow kinetic energy in Table 5) and mainly driven by the remaining latitudinal shear. This leads to two meridional cells crossing the equator, as seen in the last panels of Figure 10. Having presented the large-scale flows achieved in the simulations, we now turn to discussing their magnetic properties.

5. Magnetic Properties

In this section, we discuss in more detail various aspects of our dynamo simulations, such as their type, their temporal

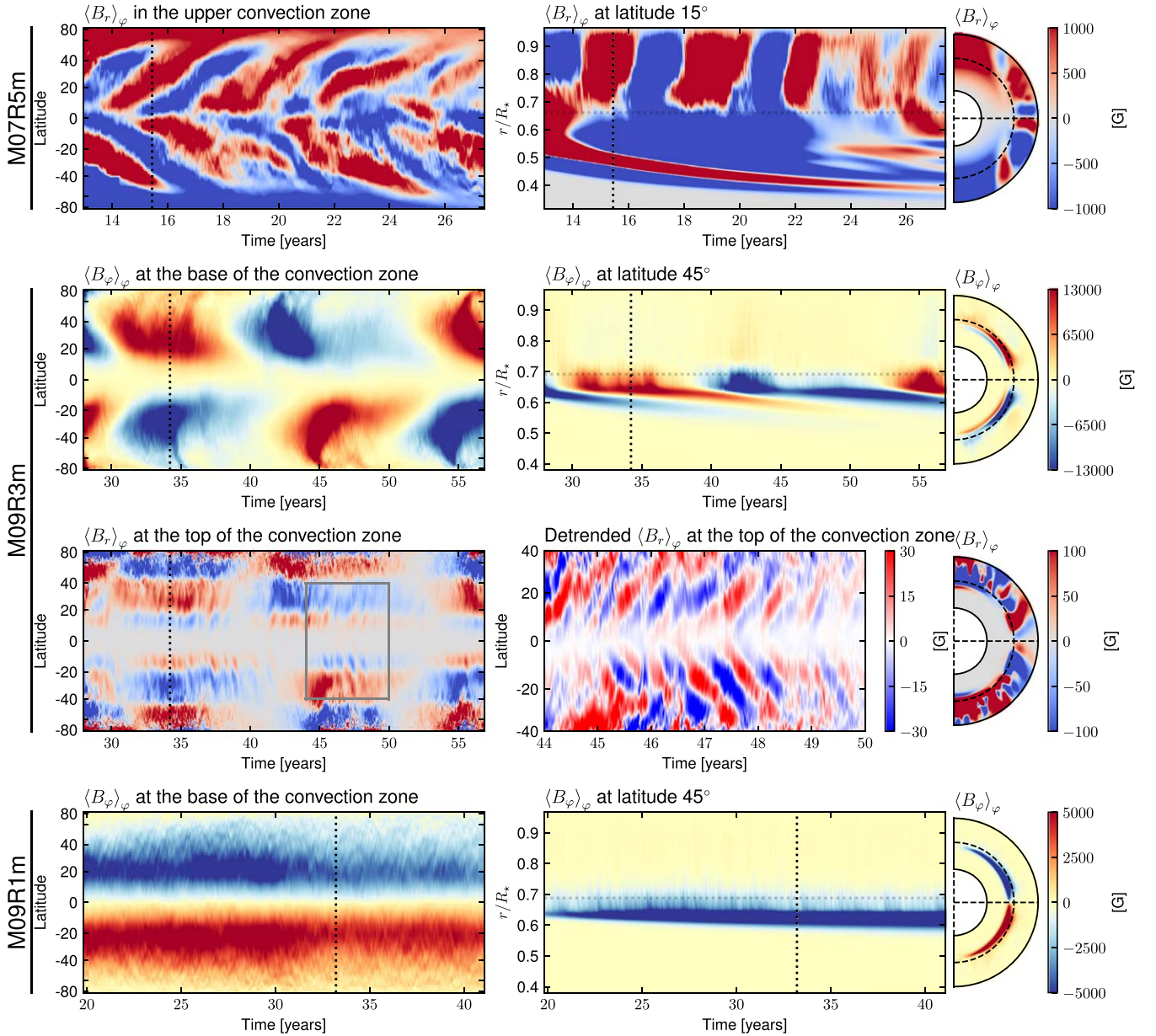


Figure 11. Various dynamo states achieved in our sample by our models, as illustrated by M07R5m (top panels), M09R3m (middle panels), and M09R1m (lower panels). In the top panel, we show the time–latitude, time–radius, and instantaneous meridional plane of B_r (red denotes positive values and blue negative values), with sampling times indicated by a vertical dashed line. These illustrate the short magnetic cycles achieved by our models. The four middle panels illustrate both the short and long cycles achieved in model M09R3m. The first panels show the latitude–time (at the base of the convection zone) and radius–time (at midlatitude) diagrams of the mean azimuthal magnetic field that reverses on a decadal timescale. The two panels below show the mean radial field at the top, which also shows the same cyclicity. Once the long cycle is filtered, the short cycle appears in the zoomed panel on the right at a particular epoch and around the equator. The lowest panels show the mean azimuthal field for model M09R1m and illustrate a dynamo with no cycles but which sustains strong stable wreaths at the base of the convective envelope.

variability, the amount of magnetic flux they generate, and the distribution in space and size of their magnetic fields.

5.1. Properties of Dynamo Solutions: Long Cycles, Short Cycles, and Steady Dynamos

We find three dynamo states in our sample of 15 MHD models: long (decadal) magnetic cycles, short (yearly) magnetic cycles, and stable magnetic wreaths concentrated close to the bottom of the convection zones. These three states are illustrated in Figure 11 with models M07R5m, M09R3m, and M09R1m.

Let us first focus on the decadal cycles, as the one found for M09R3m (see middle left panels in Figure 11). In this model,

we find that the global magnetic field of the star reverses with a period of 10 yr (see first column in Table 4). The averaged azimuthal field at the bottom of the convection zone presents a solar-like butterfly diagram, with both polar and equatorial branches. The magnetic field is generally consistent with dipolar symmetry, with the azimuthal field of inverse polarities in each hemisphere. We also see some departures from hemispheric symmetry (for instance around $t = 42$ yr). The azimuthal field is found to be concentrated at the base of the convective envelope and in the tachocline, where the radial shear of Ω is maximized, as shown in the time–radius and meridional diagrams. It develops over a relatively large latitudinal extent, as shown by the active latitudinal band

Table 4
Magnetic Properties of the Modeled Dynamos

	Long Cycle (y/[yr]/n)	Short Cycle (y/[yr]/n)	$\delta_s\Omega$ [nHz]	Active lat. [$^{\circ}$ - $^{\circ}$]	Φ_{tot} [10^{24} Mx] $_{\text{min}}^{\text{max}}$	B_{rms} [G] $_{\text{min}}^{\text{max}}$	$B_{r,\text{dip}}$ [G] $_{\text{min}}^{\text{max}}$	$B_{L,\text{surf}}$ [G] $_{\text{min}}^{\text{max}}$	f_{dip}	f_{quad}
M05Sm	n	n	2.4	[43–45]	$3.0_{2.6}^{3.3}$	793_{683}^{884}	191_{156}^{217}	357_{296}^{407}	0.21	0.22
M05R1m	13.6 ± 5.7	1.2 ± 0.6	2.1	[31–31]	$1.9_{1.3}^{2.5}$	575_{343}^{805}	58_{17}^{99}	158_{88}^{234}	0.05	0.25
M05R3m	21.4 ± 9.4	0.5 ± 0.2	2.1	[44–45]	$2.1_{1.0}^{3.4}$	552_{297}^{830}	38_{93}^{93}	146_{69}^{215}	0.28	0.37
M05R5m	n	1.8 ± 1.0	3.0	[49–55]	$8.6_{4.7}^{9.1}$	1698_{1131}^{1851}	196_{21}^{236}	819_{426}^{929}	0.19	0.35
M07Sm	n	n	5.4	[51–53]	$4.8_{4.5}^{5.2}$	575_{524}^{648}	136_{130}^{142}	306_{279}^{340}	0.29	0.38
M07R1m	6.2 ± 1.1	1.4 ± 1.3	3.7	[26–35]	$8.6_{6.16}^{11.7}$	949_{616}^{1325}	200_{100}^{266}	439_{261}^{601}	0.38	0.48
M07R3m	y	2.5 ± 0.8	4.1	[21–22]	$8.7_{3.2}^{13.0}$	972_{127}^{1951}	157_{40}^{251}	340_{198}^{573}	0.12	0.40
M07R5m	n	1.0 ± 0.7	1.2	[55–58]	$18.4_{15.3}^{20.2}$	1597_{1320}^{1879}	181_{52}^{351}	925_{699}^{1072}	0.35	0.48
M09Sm	n	n	13.1	[72–73]	$1.8_{1.7}^{1.8}$	109_{97}^{123}	53_{49}^{55}	60_{55}^{66}	0.60	0.17
M09R1m	n	n	9.0	[20–21]	$1.1_{0.9}^{1.5}$	68_{58}^{100}	11_6^6	23_{18}^{33}	0.23	0.29
M09R3m	9.9 ± 1.8	0.9 ± 0.6	9.0	[24–26]	$2.2_{0.3}^{4.0}$	133_{51}^{261}	10_{69}^{23}	47_{6}^{91}	0.16	0.27
M09R5m	n	1.3 ± 0.7	9.5	[30–35]	$13.4_{10.7}^{18.7}$	657_{485}^{970}	274_{221}^{400}	392_{284}^{608}	0.35	0.44
M11R1m	n	n	12.4	[46–47]	$14.5_{13.2}^{15.8}$	589_{544}^{650}	$10_{0.8}^{23}$	184_{161}^{197}	0.06	0.31
M11R3m	4.9 ± 0.9	n	11.5	[20–21]	$2.7_{0.7}^{7.1}$	86_{20}^{226}	$11_{0.7}^{31}$	55_{13}^{60}	0.22	0.29
M11R5m	.	.	39.0	[52–77]	$53.1_{41.6}^{57.7}$	1208_{980}^{1329}	71_{528}^{875}	809_{596}^{986}	0.51	0.11

Note. The first column indicates the presence or absence of a long (decadal), deeply seated magnetic cycle. When the time series were long enough to identify a cycle period unambiguously, its value is given with error bars. Otherwise, the existence of such a cycle is indicated by a yes (“y”) and its absence by a no (“n”). The second column shows the same for the short magnetic cycle that we identify in the upper convection zone near the equator. We do not indicate this information for model M11R5m, which was not run long enough to determine the existence or absence of magnetic cycles. The third column indicates the amplitude of the torsional oscillations at the surface in nHz (see Section 5.3). The fourth column shows the active latitudinal band at the bottom of the convection zone, based on the azimuthally averaged and temporally varying azimuthal field straddling the base of the convection zone. The fourth column shows the total magnetic flux at the surface, in units of 10^{24} Mx, with the minimum and maximum as the subscript and superscript (see Section 5.4). The three next columns show the root-mean-squared surface field in Gauss, the surface dipole in Gauss, and the surface large-scale radial field $B_{L,\text{surf}}$ (taken for $l < 5$) in Gauss with the same layout (see Section 7). Finally, the last two columns show the fractions of the large-scale dipole (f_{dip}) and quadrupole (f_{quad}), as defined in Section 5.5.

reported in the fourth column of Table 4. We find this band to be centered at higher latitudes the slower the model rotates for low and intermediate Rossby numbers. Conversely, this activity band moves to high latitudes for models with antisolar DR. The averaged radial magnetic field at the surface is also found to reverse with the same timescale. At the surface, the migration branches are nevertheless not as clear as deep within the convection zone in this case. Strugarek et al. (2017, 2018) also found similar deeply seated cycles using the EULAG code, as well as Augustson et al. (2015) using the ASH code. The cyclic behavior in their results originates from the nonlinear magnetic feedback of the large-scale Lorentz force onto the DR. This weakens the source of the mean toroidal field that decreases and reverses, while the associated poloidal field closely follows due to the sign inversion of the electromotive force. We find the same mechanism in this new sample of simulation with the ASH code. Indeed, the DRKE cyclic variation observed in Figure 3 compensates the magnetic energy cyclic variation, pointing toward a magnetic cycle determined by the Lorentz force feedback. This fascinating dynamo regime sustaining a long decadal magnetic cycle, because of the existence of a subtle nonlinear feedback loop between the large-scale shear and the toroidal magnetic field, is therefore confirmed by the present study using a different numerical code than Strugarek et al. (2017). We stress that its existence can be unveiled here only because we consider fully nonlinear convective dynamos, with a self-consistent DR maintenance and magnetic field generation.

Still, we have attempted to interpret our simulations through mean-field dynamo theory by inverting the α tensor and its antisymmetric part γ by means of the singular-value decomposition (SVD) technique (see Augustson et al. 2015; Simard et al. 2016).

The details of this procedure are given in Appendix B. One can then use the derived $\bar{\alpha}$ profile to compute the Parker–Yoshimura rule (Parker 1955; Yoshimura 1975) and assess the consistency of a mean-field approach with our 3D turbulent model. We therefore compute

$$S_{\theta} = -\lambda\alpha\partial_r(\Omega/\Omega_0), \quad (13)$$

where $\lambda = r \sin \theta$. The time–latitude variations of S_{θ} are shown at the base of the convection zone of M09R3m in the left panel of Figure 12, with red/white denoting a southward migration rule and blue/black a northward migration rule. We overlay contours of B_{ϕ} as black contours (solid/dashed denoting positive/negative contours) in the left panel. We see that the derived Parker–Yoshimura dynamo wave rule does not agree with the observed latitudinal propagation, which strengthens our interpretation in terms of a cycle dominated by the Lorentz force feedback on the DR itself.

We also find another type of cyclical behavior in our sample of models: short cycles, which seem to preferentially be sited close the equator and in the upper part of the convection zone. Such types of cycles have already been reported in previous publications with numerical models (Beaudoin et al. 2016; Käpylä et al. 2016; Strugarek et al. 2018) and could be reminiscent of the possible quasi-biennial oscillations observed in the Sun (Broomhall et al. 2012; Simoniello et al. 2013). They oscillate on a yearly timescale as shown in the second column of Table 4. Short cycles are interestingly found in almost all of our models, except the slowly rotating cases. Two short cycles are illustrated in Figure 11 for cases M07R5m and M09R3m. In the former fast-rotating case, no long deeply seated cycle is observed, and the short cycle clearly appears in both the latitude–time and radius–time diagrams. In the case

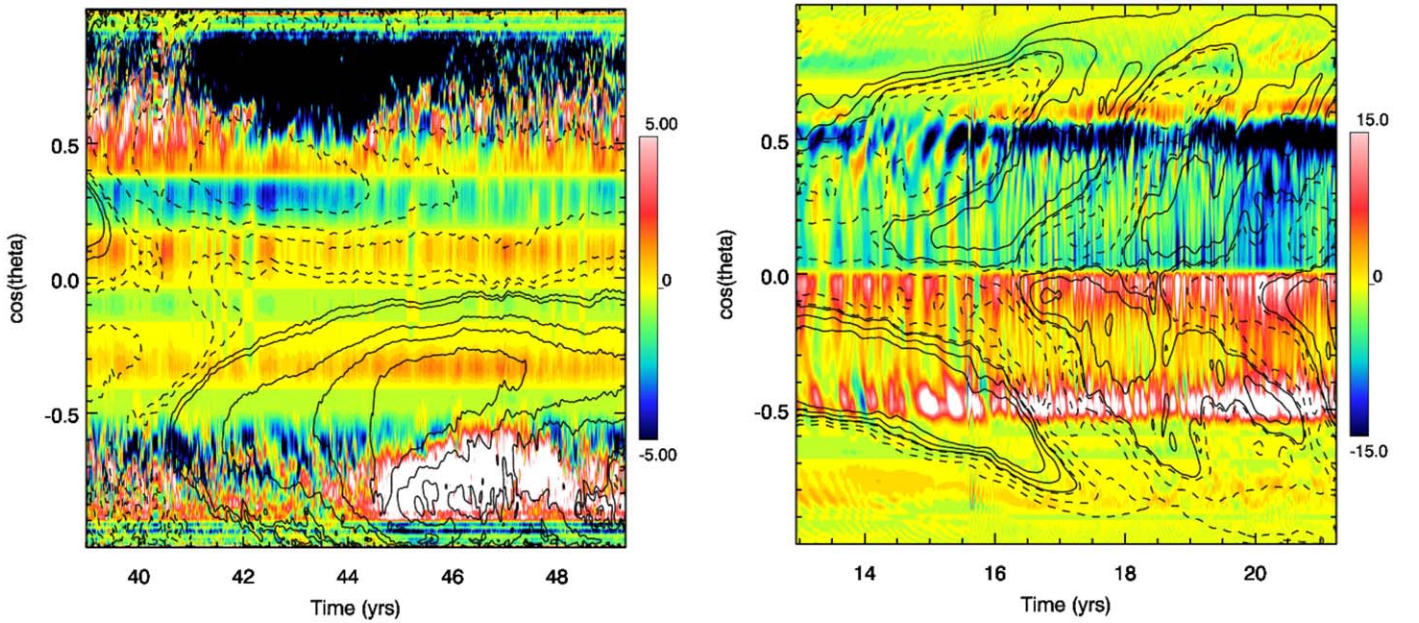


Figure 12. Parker–Yoshimura rule S_θ (see Equation (13)) as deduced from the SVD extraction of the equivalent mean-field α tensor. On the left, it is shown for model M09R3m at the base of the convective envelope as a function of the cosine of the colatitude and time (color contours in m s^{-1}). Contours of B_ϕ are overlaid in black contours (solid denotes positive values, dashed negative values; covering $\pm[250, 10^4]$ G). On the right, the same is shown for model M07R5m in the mid-upper part of the convective envelope. In this case, the black lines label contours of B_r (covering $\pm[75, 1500]$ G).

M09R3m, both types of cycle are found at the same time, and the short cycle appears clearly once the signal of the long cycle is removed (see zoomed panel). The short cycles are found to always show a poleward propagation branch and to be concentrated close to the equator. We have performed the same SVD analysis and show the Parker–Yoshimura rule S_θ (Equation (13)) for model M07R5m, which is shown in the right panel of Figure 12. In this case, the analysis is carried out in the upper part of the convective envelope, and contours of B_r are overlaid above the propagation rule. The Parker–Yoshimura rule is found here to be in good qualitative agreement with the poleward branch, suggesting that an $\alpha - \Omega$ or an $\alpha^2 - \Omega$ dynamo could be at the source of this type of cycle. The short cycles furthermore embed much less magnetic energy than the deeply seated ones, and we do not find any clear DRKE beating associated with them. As a result, we find that the two types of cyclical behaviors likely originate from two different dynamo processes: the deep-seated cycle from the large-scale feedback loop between the magnetic field and the DR through Maxwell torques, and the short cycles from the standard $\alpha - \Omega$ or $\alpha^2 - \Omega$ dynamo loop. Finally, short cycles were also reported in the study of Strugarek et al. (2018), with the same type of localization within the convective envelope. In this previous study, the short cycles were only found at small Rossby number, i.e., for the fast-rotating cases. Here we find short magnetic cycles much more ubiquitously in our sample models, as they only disappear at large Rossby numbers. It is possible that the coarse resolution used in Strugarek et al. (2018) with the EULAG code prevented models at intermediate Rossby number to develop such magnetic cycles. Additional modeling effort pushing the turbulence level of the simulations is required to properly assess this point, which is left for future work.

Finally, some models in our sample do not present any cyclical behavior. Instead, they sustain a steady dynamo with stable magnetic wreaths within their convective envelope and

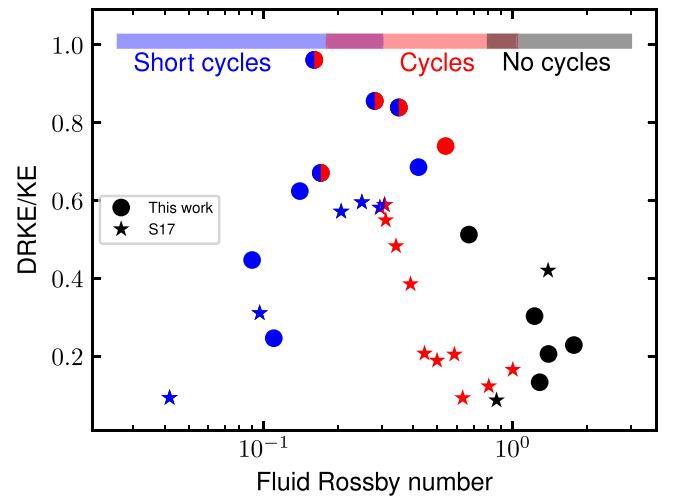


Figure 13. Summary of the dynamo states found in our study (circles) and in the previous study of Strugarek et al. (2017) (stars). In both studies, we find a clear trend in the type of cyclical behavior that models tend to produce as a function of the Rossby number. They are shown here by the ratio between the differential rotation and total kinetic energies. For small Rossby numbers, only short cycles are found. At intermediate Rossby numbers, decade-long cycles resembling the solar cycle start to appear on a relatively narrow parameter space. At high Rossby numbers, magnetic cycles disappear and our models produce energetic stable wreaths of magnetic field in their convective envelopes.

tachocline. This is the case, for instance, with model M09R1m shown in the lower panels of Figure 11. We obtain such solutions only in the high Rossby number regime, close to and above the transition toward an antisolar DR.

To summarize, we find that the different types of cyclical behaviors exist in specific Rossby number ranges in our sample. We illustrate this in Figure 13 where we follow Gilman (1983) and show DRKE/KE as a function of Ro_f in our set of models. Short cycles are found for $Ro_f \lesssim 0.42$, deeply seated

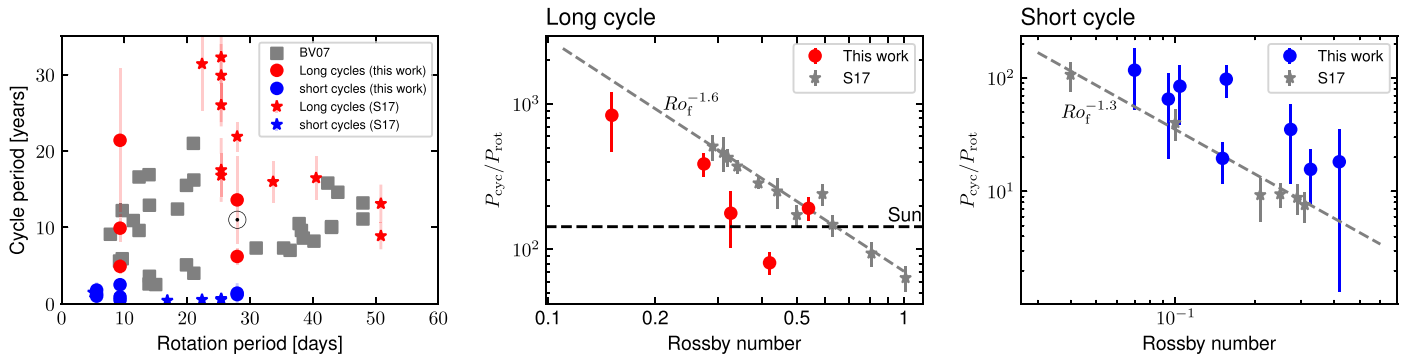


Figure 14. Magnetic cycle period trends. The left panel shows the classical cycle period–rotation period diagram with our models (circles), the models published in Strugarek et al. (2017) (stars), and the stellar sample of Böhm-Vitense (2007) (gray squares). The middle panel shows the trends of the long-cycle period divided by the rotation period as a function of Rossby number. The right panel shows the same for the short cycles. In those two panels, the Rossby trend deduced in Strugarek et al. (2018) is indicated by the gray dashed line.

solar-like cycle for $0.15 \lesssim Ro_f \lesssim 0.65$, and steady magnetic fields for $Ro_f \gtrsim 1.0$. The exact boundaries between these cyclical behaviors regimes are not precisely defined and may depend on a number of factors. First, let us note that the same trend was found in Strugarek et al. (2018) with the EULAG code, as shown by the colored stars also plotted in Figure 13. This is very important because it again demonstrates that the results discussed in this study are not code or setup dependent, but the results of genuine nonlinear convective dynamo action in a rotating spherical shell. It confirms that the Rossby number is one of the key parameters to characterize the various dynamo states found in the literature and that cyclic convective dynamo solutions clearly exist in a parameter regime that our study helps to refine. The transitions between the different types of cycles were found at slightly different Rossby numbers, possibly due to different Reynolds, Prandtl, and Rayleigh numbers regimes achieved in the two ensemble of simulations. Indeed, Nelson et al. (2013) showed that fast-rotating models exhibiting stable wreaths of magnetism (Brown et al. 2010) could produce reversals when the Reynolds and Rayleigh numbers are increased. Because the Rossby number of the more turbulent models nevertheless changes significantly as well, it is therefore unclear whether this can be attributed to a fundamental change in the dynamo action or if it is the consequence of a change in Rossby number. Fundamental exploration aimed at predicting the Rossby number of turbulent numerical experiments such as Anders et al. (2019) is very promising in that respect and needs now to be extended to the full MHD regime. For the time being, we can conclude here that qualitatively the different regimes highlighted by our simulations are robust, yet simulations at much higher turbulent levels are required to assess the exact regime boundaries. Please note that case M11R5m is sometimes omitted in ensemble analysis in Sections 5 and 6 because it is not as well numerically converged as all the other cases and can sometimes be an outlier in some analysis. This does not impact our conclusions in any of the results reported in the paper.

5.2. Dependencies of the Cycle Periods

We have calculated the period of the short and long cycles and reported their values in the second and third columns of Table 4. We use the approach initially followed by Käpylä et al. (2016) and Strugarek et al. (2018) and rely on an empirical-mode decomposition method (Luukko et al. 2015) to identify quasi-periodic signals. Five of our models clearly

exhibit a deeply seated long cycle that can be identified by eye. We were nevertheless able to calculate accurately the associated period for four of them. The cycle period of the fourth model would require integration times at least twice as long to be identified. This would require an even more massive numerical effort and will be explored in future work. Still we can deduce with some confidence what characterizes this long-cycle nonlinear dynamo case. Conversely, the short cycles take place higher up in the convective envelope and their short periods allow us to determine the cycle periods for all the models exhibiting them. The error bars on the cycle periods are directly estimated with the empirical-mode decomposition method, as explained in Strugarek et al. (2018).

The left panel of Figure 14 shows the cycle periods (in years) as a function of the rotation period (in days) of our models. We report both short and long cycles here, respectively, in blue circles and red circles. We have also added the cycles found with the EULAG code and reported in Strugarek et al. (2017, 2018) as red and blue stars. Finally, we have overlaid the detected cycles of distant stars reported by Böhm-Vitense (2007) as gray squares, as well as the Sun right in the middle of the figure. Our three identified long cycles are achieved by models with different masses, which make their direct comparison subject to caution in a $(P_{\text{cyc}}, P_{\text{rot}})$ diagram. Overall, we do not recover the dichotomy between active and inactive branches as initially proposed by Saar & Brandenburg (1999) and Böhm-Vitense (2007). Rather, our sample of models combining the ASH and EULAG simulations spans the whole diagram, including the hypothetical gap where the Sun stands.

Using the EULAG sample of simulations only, we have previously shown that the cycle period is controlled by the effective Rossby number achieved by the simulated convection zone (Strugarek et al. 2017). This is shown for the long and short cycles in the middle and right panels of Figure 14. Here we find that our new ASH simulations are compatible with the trends obtained with the EULAG sample, which strengthens the similarities between the modeled dynamos in our two studies. This is moreover remarkable as the ASH simulations include a tachocline and a deeper radiative layer, whereas the EULAG sample considered only an isolated convective shell.

The fact that the cycle period seems to decrease with the Rossby number has also been reported by other research groups using yet another code (see, e.g., Warnecke 2018). So far, only one study relying on 3D turbulent simulations (Guerrero et al. 2019) has shown some evidence for the cycle period increasing

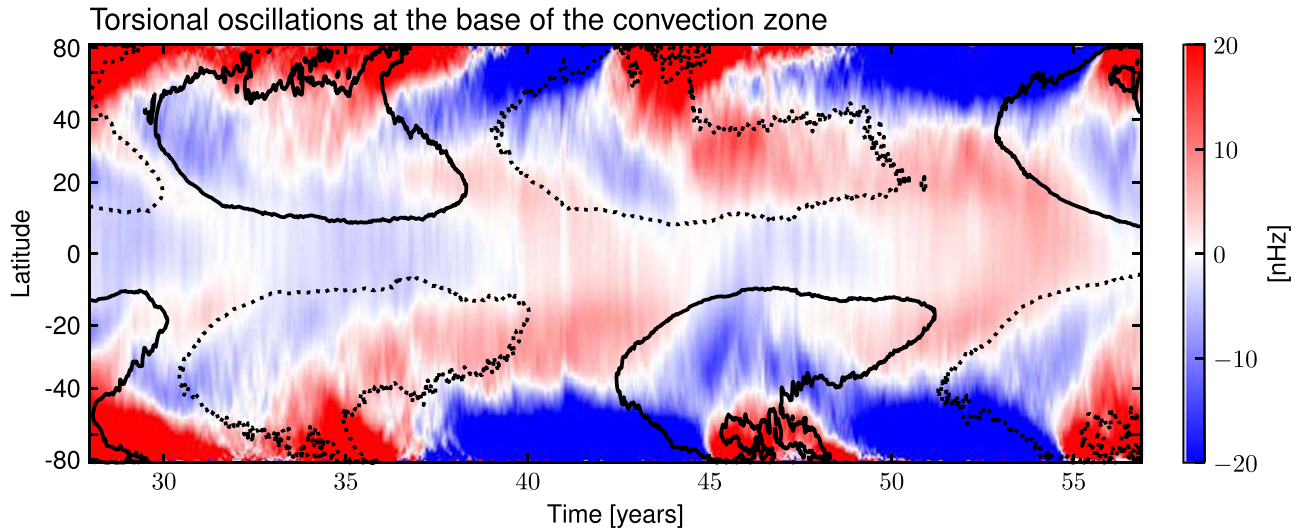


Figure 15. Torsional oscillations (in nHz) in model M09R3m at the base of the convective envelope, as a function of latitude and time. The black lines label the contour of $\langle B_\phi \rangle_\theta$ at +4000 G (plain lines) and -4000 G (dashed lines).

with rotation period. We believe this is due to how their DR scales with rotation rate. Indeed, their simulations exhibit a DR that strengthens as the rotation rate decreases (i.e., the rotation period increases). This is at odds with all the aforementioned studies (including the present work), where we find it to increase with the rotation rate up to a point where magnetic feedback strongly back-reacts to suppress it. We suspect that the thermal treatment of the radiative-convective interface may produce this effect in the work of Guerrero et al. (2019), albeit additional analyses are required to confirm this interpretation. Finally, it is worth noting that more complex dynamo states have also been reported in a similar Rossby number regime with the PENCIL code by Viviani et al. (2019). This again warrants caution in the interpretation of simulation results at moderate Reynolds number and highlights the need to achieve more turbulent regimes in future work to confirm our trends.

5.3. Torsional Oscillations in Cyclic Solutions

We observe clear and strong torsional oscillations $\delta_t \Omega$ (Basu & Antia 2019) in all our models that exhibit a long, deeply seated cycle. Torsional oscillations take the form of a modulation of the azimuthally averaged rotation rate $\Omega(r, \theta, t)$ in depth, latitude, and time. We illustrate the torsional oscillations at the base of the convection zone of model M09R3m in Figure 15. The torsional positive/negative oscillations are shown in red/blue in nHz as a function of time and latitude. We have overlaid isocontours of B_ϕ in black (plain lines correspond to 4000 G, dashed lines to -4000 G). The torsional oscillations are observed to be in phase with long magnetic cycle. At cycle minimum (in between the black contours), the poles are rotating slower (blue) and the equator faster (red), meaning that the latitudinal DR is strengthened as the magnetic field weakens and the associated magnetic torque stops inhibiting it. During cycle maximum, the opposite situation occurs, and the DR is found to decrease substantially. We observe torsional oscillations very similar to what were found with EULAG simulations by Strugarek et al. (2017, 2018) and previous ASH simulations by Nelson et al. (2013) and Augustson et al. (2015). In all these simulations, the torsional oscillations are found to play a major role in producing the deeply seated cycle. This is reassuring because

such nonlinear interplay between the flow and field seems independent of setup details such as BCs or numerical schemes. Moreover, torsional oscillations in our models are very energetic: they reach more than 20 nHz at the base of the convective envelope in model M09R3m, and their energy corresponds to the energy variations in the total magnetic energy (ME) seen in Figure 3. As a result, we find they play an active role in allowing deeply seated cycles by reversing locally $\partial\Omega/\partial\theta$ and hence generating a toroidal field of opposite sign.

We have also searched for torsional oscillations at the locations of short magnetic cycles, i.e., at the surface and close to the equator of fast-rotating models. We find a temporal modulation of the local rotation rate at the surface in all our models. We have nevertheless not found any evidence for a correlation between these temporal variations and the short cycles themselves. This confirms that a different dynamo process sustains the short cycles, which is likely related to a more standard $\alpha - \Omega$ mechanism as we have seen in Section 5.1.

Finally, we have characterized the surface torsional oscillations in all our models and reported in Table 4 the average values of $\delta_t \Omega$ within the activity band identified in Table 4. The surface torsional oscillations range from about 1 to 39 nHz in our sample of simulations, which corresponds to 0.4%–6% of the model rotation rates. Torsional oscillations associated with short cycles are found to be very weak, and the ones associated with the long cycle to be prominent deep inside the convective envelope. As a result, we do not observe any strong correlation between the amplitude of the surface torsional oscillations and the Rossby number of our models: a linear regression gives $\delta_t \Omega / \Omega_* \propto Ro_f^{1.1 \pm 0.15} \simeq Ro_f$.

5.4. Magnetic Flux Budget

To further assess the magnetic properties of a dynamo solution, we display in Figure 16 for three representative cases (M05R1m, M09R3m, M11R1m) various measures of the magnetic flux available at the top boundary layer, that is, Φ_+ and Φ_- , the magnetic fluxes for $B_r|_{r=r_{\text{top}}} > 0$ and $B_r|_{r=r_{\text{top}}} < 0$, respectively, the total flux $\Phi_{\text{tot}} = |\Phi_+| + |\Phi_-|$, the net flux $\Phi_{\text{net}} = \Phi_+ + \Phi_-$, and the southern Φ_S and northern Φ_N hemispheric fluxes (i.e., integrated only over the northern

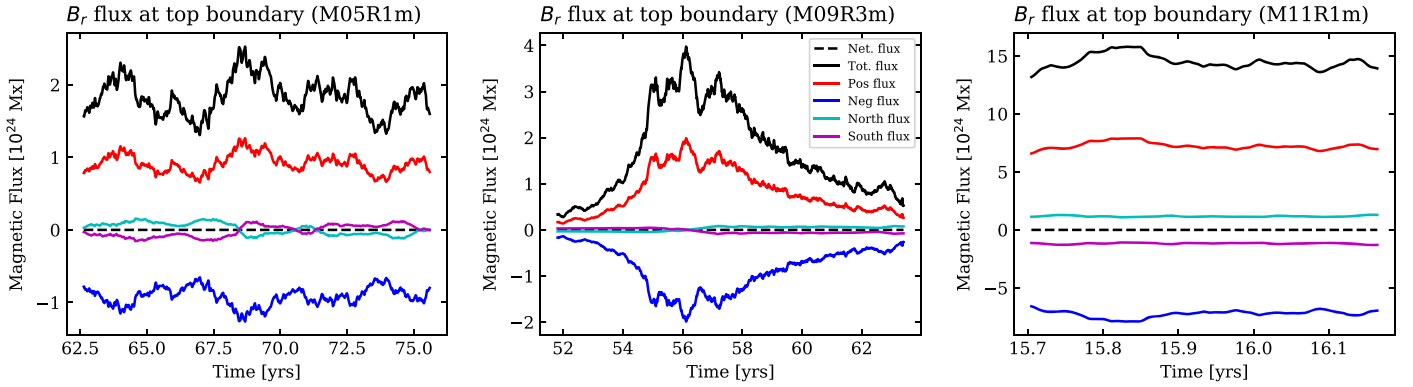


Figure 16. Temporal evolution of various measures of the magnetic flux in representative dynamo cases studied. Plotted for models M05R1m, M09R3m, and M11R1m are the positive (red) and negative (blue) fluxes Φ_+ and Φ_- , total flux $\Phi_{\text{tot}} = |\Phi_+| + |\Phi_-|$ in black, the net flux $\Phi_{\text{net}} = \Phi_+ + \Phi_-$ as a dashed black line, and the southern (cyan) and northern (magenta) hemispheric fluxes. In the M05R1m and M09R3m cases we clearly see the temporal modulation commensurable to their activity cycle.

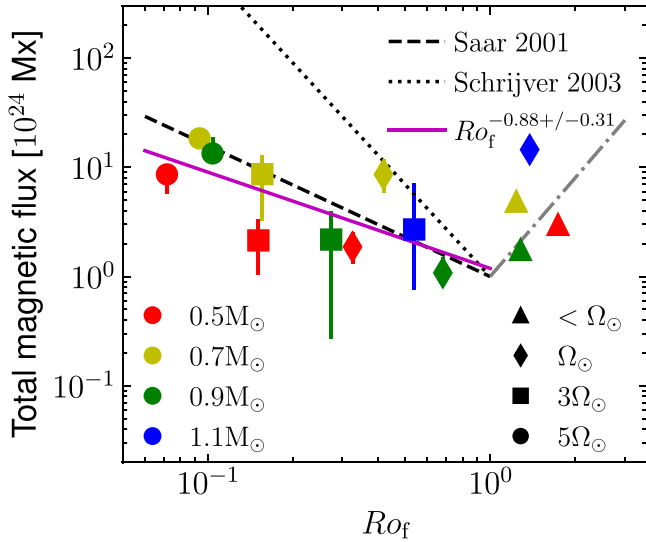


Figure 17. Total magnetic flux as a function of Rossby number. The different models are labeled in the same way as in Figure 7. The trends from Saar (2011) and Schrijver et al. (2003) are shown, respectively, by the dashed and dotted black lines, assuming a constant stellar mass. An indicative trend proportional to Ro_f^3 is indicated as a dashed-dotted line in the $Ro_f > 1$ regime.

and southern hemispheres, respectively). First, we see the very good conservation of the divergenceless nature of the magnetic field, with Φ_{net} being systematically null (so implying that $\Phi_- = -\Phi_+$, as clearly evident). This is the direct consequence of solving the induction equation via a poloidal–toroidal field decomposition (see Equation (6)). Likewise, the two hemispherical measures of Φ have opposite signs, but a much smaller amplitude than Φ_+ and Φ_- by about a factor of 10. This is likely due to a highly structured magnetic field because for an axial dipole they are expected to be equal. When adding up the absolute value of Φ_+ and Φ_- , we can assess the total amount of magnetic flux generated by the dynamo. We find fluxes from 10^{24} to 10^{25} Mx, which are in good agreement with values observed in the Sun (see for instance Figure 3 of Schrijver & Harvey 1994). We also note that in the M05R1m and M09R3m cases, both of which possess a clear and long magnetic cycle, the temporal modulation of the magnetic fluxes is obvious. In the M05R1m case, the modulation is about a factor of 2 from the minimum to maximum of activity. In case M09R3m, it reaches almost a factor of 8 (compared to 5 for the

Sun). Here again the larger mass (luminosity) of M09R3m and its higher rotation rate leads to a larger temporal modulation of the magnetic energy and hence the magnetic flux. Finally, for the steady dynamo case M11R1m, possessing an antisolar DR, a very small magnetic flux variability is observed. However, it is the model with the highest value of the total magnetic flux, reaching about 10 times what is observed in the present Sun.

We furthermore see a tendency for Φ_{tot} to increase with both stellar mass and rotation rate, in good agreement with the level of magnetic energy found in the simulations. However, more robust tendencies appear on the rotation when one considers only the model with $Ro_f < 1$. They are interestingly compatible with a simple linear dependency, with $\Phi_{\text{tot}} \simeq 2.3 \Omega_*^{0.84 \pm 0.42}$ for the rotation rate. When considering how the total magnetic flux scales with rotation rate $\Phi_{\text{tot}} \propto \Omega_*^n$, different values from $n = 1.2$ (Saar 2001) to $n = 2.8$ (Schrijver et al. 2003) have been proposed (Rempel 2008). In our study we find a tentative scaling with the fluid Rossby number as

$$\Phi_{\text{tot}} \simeq 1.19 Ro_f^{-0.88 \pm 0.31} 10^{24} \text{Mx}, \quad (14)$$

as shown in Figure 17, where the time-averaged total flux of each model is considered (see also Table 2). Our models depart significantly from this trend when their Rossby number exceeds one, indicating a possible change for very slowly rotating stars. In this regime, our sample of models suggests that the total magnetic flux increases with Rossby number, as shown by the dashed-dotted line. Additional models at large Rossby numbers are required to fully characterize this regime properly, which we leave for future work. To summarize, we find that the total magnetic flux follows a trend compatible with the one from Saar (2001) for intermediate and small Rossby numbers and that this trend reverses for slow rotators ($Ro_f > 1$).

5.5. Dynamo Families and f_{dip}

We now turn to considering how the change of DR state as a function of the Rossby number may influence the relative amplitude of the dynamo modes. We have seen in the previous sections that as we vary the Rossby number, the type of dynamo solution changes, going from steady for large Rossby numbers to long-period cyclic solutions for intermediate values of the Rossby number, to fast cyclic solutions for low Rossby numbers.

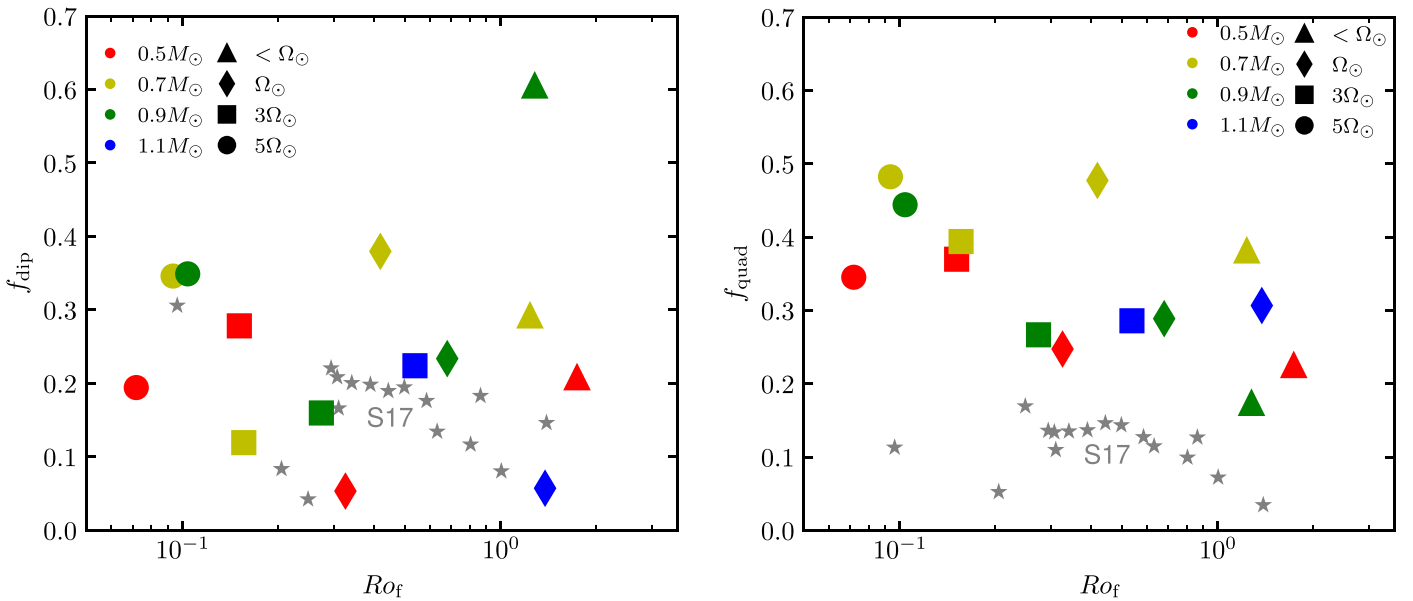


Figure 18. f_{dip} and f_{quad} in all 15 models (color symbols) and those published in Strugarek et al. (2017, 2018) (gray stars). Models with Rossby number greater than 1 possess an antisolar differential rotation. We see only a weak decreasing trend of f_{dip} and f_{quad} with Rossby number (for the parameter space explored). In addition, there does not seem to be a collapse of the large-scale magnetic field for slowly rotating stars.

Such a variation of the temporal behavior of the dynamo solutions may or may not be associated with a change in dominant field geometry. This is of particular importance because it has been recently claimed by van Saders et al. (2016, 2019), Metcalfe & van Saders (2017), and Hall et al. (2021) that the Sun and solar-like stars older than the Sun may be undergoing a magnetic activity transition around a Rossby number of 1 (see Lorenzo-Oliveira et al. 2018 for an alternative view). In particular, they argue that the wind-braking efficiency may be collapsing around that rotational state transition. This would result in stars rotating more rapidly than what the Skumanich law or gyrochronology would have predicted (Skumanich 1972; Barnes 2003). If, for instance, a collapse of the large-scale dynamo modes (mainly dipole and quadrupole) would occur after transitioning to antisolar DR, this would provide a very simple explanation, as it is well known that the most efficient wind braking for Sun-like stars is found for the simplest magnetic field geometry (Kawaler 1988; Réville et al. 2015; Finley & Matt 2018). In order to assess if such a change of magnetic geometry occurs at or near the $Ro_f \sim 1$ limit, we will use a measure called f_{dip} , which was introduced by Christensen & Aubert (2006), and that permits the assessment of the energy content of the dipolar field with respect to the first 12 magnetic modes. We also introduce f_{quad} , using the same principle, as a quadrupolar field configuration is still quite efficient at spinning down a star via its associated wind braking. Both are defined as

$$f_{\text{dip}} = \frac{\sum_m (a_{1,m})^2}{\sum_{l < 12, m} (a_{l,m})^2}, \quad (15)$$

$$f_{\text{quad}} = \frac{\sum_m (a_{2,m})^2}{\sum_{l < 12, m} (a_{l,m})^2} \quad (16)$$

where $a_{l,m}$ are the spherical harmonics coefficient of the radial magnetic field at the upper boundary (surface) of our models.

In Figure 18 we show f_{dip} (left panel) and f_{quad} (right panel) from 32 dynamo cases: the 15 cases analyzed in details in this

paper, to which we add the 17 published in Strugarek et al. (2018), using the EULAG-MHD code (Smolarkiewicz & Charbonneau 2013). This allows us to extend our database and to compare nonlinear dynamo solutions obtained with two different MHD codes using very different numerical techniques, hence giving us confidence that the trend found in our simulations is not due to a given code. We observe a relatively good agreement between the ASH and EULAG databases for f_{dip} and surprisingly find that the EULAG set of simulations produces systematically a weaker f_{quad} compare to the ASH database. In both series we find a weak trend for a decrease of f_{dip} and f_{quad} with the Rossby number. Nevertheless, we do not find any hint of a collapse of f_{dip} or f_{quad} when the Rossby number exceeds 1 and the DR realized in the simulations becomes antisolar. The weak decreasing trend is not significant enough to explain the stalling of stellar wind braking advocated by van Saders et al. (2016) and Metcalfe et al. (2016). Hence, it seems unlikely that field geometry is the source of the wind-braking regime change for old solar-type stars. This is in agreement with the observational study of Vidotto et al. (2016), who have analyzed spectropolarimetric inversion for a suite of Sun-like stars, and they too did not find a collapse of the dipole strength as they crossed the $Ro_f = 1$ limit. So if such a stalling of stellar spin-down occurs, it must come from another mechanism (see Section 7).

In summary, we have shown in Section 5 that the dynamo solutions presented in this study possess very interesting magnetic properties that agree very well with observations and other theoretical studies. In particular, we have confirmed the key role of the Rossby number (and magnetic Reynolds number) in determining the type of dynamo realized. Now we wish to characterize better their energy content and how energies flows back and forth from kinetic to magnetic reservoirs.

6. Energy Content and Transfers in Stellar Convective Dynamos

In the following section, we analyze the kinetic and magnetic energies contained in the models and how they are distributed between their various components.

Table 5
Kinetic and Magnetic Energy Densities

(erg cm ⁻³)	KE ×10 ⁶	DRKE (%KE) ×10 ⁶	MCKE (%KE) ×10 ⁴	CKE (%KE) ×10 ⁶	ME (%ME) ×10 ⁶	TME (%ME) ×10 ⁵	PME (%ME) ×10 ⁴	FME (%ME) ×10 ⁵
M05Sm	9.3	2.1 (22.8%)	17.1 (1.8%)	7.0 (75.3%)	1.7 (17.7%)	6.7 (40.8%)	6.1 (3.7%)	9.2 (55.5%)
M05R1m	20.3	17.0 (83.9%)	2.3 (0.1%)	3.3 (16.0%)	0.8 (3.9%)	2.5 (31.9%)	0.6 (0.7%)	5.3 (67.4%)
M05R3m	74.3	71.4 (96.1%)	0.9 (0.01%)	2.9 (3.9%)	1.1 (1.5%)	7.6 (68.2%)	0.1 (0.1%)	3.5 (31.6%)
M05R5m	2.7	1.2 (44.7%)	0.3 (0.1%)	1.5 (55.2%)	2.7 (98.2%)	8.8 (33.2%)	11.6 (4.4%)	16.7 (62.5%)
M07Sm	4.0	1.2 (30.3%)	6.1 (1.5%)	2.7 (68.2%)	0.3 (7.6%)	2.0 (65.0%)	1.3 (4.3%)	0.9 (30.7%)
M07R1m	4.8	3.3 (68.5%)	1.0 (0.2%)	1.5 (31.3%)	0.9 (18.5%)	2.8 (31.5%)	1.4 (1.5%)	5.9 (67.0%)
M07R3m	3.5	2.3 (67.1%)	0.4 (0.1%)	1.1 (32.8%)	2.0 (57.8%)	9.4 (47.1%)	4.3 (2.2%)	10.2 (50.7%)
M07R5m	1.1	0.3 (24.6%)	0.2 (0.1%)	0.8 (75.3%)	1.3 (116.2%)	0.8 (6.4%)	5.1 (3.9%)	11.7 (89.8%)
M09Sm	3.2	0.4 (13.3%)	3.0 (0.9%)	2.7 (85.8%)	0.04 (1.4%)	0.3 (68.2%)	0.7 (16.8%)	0.1 (15.0%)
M09R1m	4.0	2.1 (51.2%)	1.7 (0.4%)	1.9 (48.4%)	0.2 (5.7%)	1.9 (85.4%)	0.1 (0.6%)	0.3 (14.0%)
M09R3m	11.9	10.2 (85.5%)	0.8 (0.1%)	1.7 (14.4%)	0.5 (4.4%)	4.3 (83.5%)	0.8 (1.5%)	0.8 (15.0%)
M09R5m	2.6	1.6 (62.4%)	0.3 (0.1%)	1.0 (37.5%)	1.3 (49.3%)	4.1 (32.5%)	2.9 (2.2%)	8.3 (65.3%)
M11R1m	2.0	0.4 (20.5%)	2.0 (1.0%)	1.5 (78.4%)	0.2 (12.1%)	0.9 (37.7%)	1.9 (7.9%)	1.3 (54.4%)
M11R3m	3.9	2.9 (74.0%)	0.6 (0.2%)	1.0 (25.9%)	0.3(8.8%)	2.7 (79.2%)	1.0 (2.8%)	0.6 (18.0%)
M11R5m	2.3	1.0 (43.3%)	8.9 (3.9%)	1.2 (52.7%)	4.4 (192.3%)	1.8 (4.1%)	384.3 (88.1%)	3.4 (7.8%)

Note. The explicit definitions of the different energy decomposition are given in Appendix A and Brun et al. (2004).

6.1. Global Measure of Kinetic and Magnetic Energies

We now turn to discussing the global energy content in the convective envelope of the 15 dynamo cases presented in this study. In Table 5 we list the kinetic (KE) and magnetic (ME) energy densities and their axisymmetric and nonaxisymmetric components (see their definition in Appendix A and Brun et al. 2004). We first notice that as we increase the stellar mass, the KE is found to slightly decrease. This is due to the lower averaged mean density due to the shallower convective envelope in more massive stars. The averaged density over the simulated convective envelopes varies from 4 to 0.05 g cm⁻³ when going from models M05m to M11m, so a drop by a factor of 80. This is in part compensated by the higher luminosity (convective velocity) of the more massive stars, leading to values of KE in the range of 10⁶–10⁷ erg cm⁻³. Note that the total KE (i.e., the energy density multiplied by the volume) increases with stellar mass due to the much larger volume occupied by larger-mass stars. If we now decompose KE into its axisymmetric poloidal (MCKE) and toroidal (DRKE) and nonaxisymmetric (CKE) components, we can further understand how the energy is being distributed in the various models. First, as is often the case, MCKE is found to play a minor role in all models independently of their mass or rotation rates. In most cases, MCKE is of the order of 10⁴ erg cm⁻³ so about 1% or less of KE. This results in DRKE and CKE being the dominant components. Analyzing these two components, a clear trend is observed in common to all masses. As the rotation rate is increased, going from a Rossby number greater than 1 to a value less than about 0.1, we note that DRKE first increases to constitute up to 96% of KE. This means that most of the kinetic energy is in the DR with both strong latitudinal and radial shear across the convective envelope and at its base (we refer the reader to Section 4.1 where the angular velocity profiles of each model is discussed in details). Such a behavior is similar to what was observed in the purely hydrodynamic progenitors published in Brun et al. (2017). Hence, up to a certain rotational influence, the presence of dynamo-generated magnetic fields in the simulations does not modify significantly the trends observed before in the hydrodynamic cases. As a direct consequence, CKE is found to contribute less and less to the overall dynamics. CKE is found

to be dominant for the slowly rotating cases, their convective motions having little azimuthal mean. As the Rossby number is decreased and the rotational influence on convective motions made stronger, we see that CKE drops to less than a few percent of the total KE. However, this is not the case when the rotational influence increases even further. For all the fastest cases with the smallest Rossby numbers, we notice a sudden drop of DRKE both in percentage and absolute value, while CKE contributes relatively more to KE (but KE also undergoes a decrease of its amplitude). This is due to the strong feedback of the Lorentz force on the DR, a phenomenon often called Ω quenching (Glatzmaier 1985a; Brun 2004; Brun et al. 2005; Karak et al. 2015) and seen only in global spherical rotating models by similitude to α quenching (Blackman & Field 2001; Brun et al. 2004; Subramanian & Brandenburg 2004) found in most local dynamo simulations (at the origin of the interface dynamo paradigm; Parker 1993; Mason et al. 2008) and characterized in our simulations by the absolute concomitant drop of CKE. This significant drop of DRKE or “ Ω quenching,” accompanied by a smaller decrease of CKE or “ α quenching,” leads to a strong decrease of KE. This confirms that dynamo simulations do not have the same rotational dependence as the purely hydrodynamic cases. Because most solar-like stars are likely to have magnetic fields, such a finding indicates that scaling laws derived in this work will likely be more accurate when compared to observations. Because the influence of magnetic field becomes more and more dominant as we lower Ro_F , it is also instructive to analyze how the magnetic energy content evolves as well.

In Table 5, we also provide the value of the ME densities (total magnetic energy (ME), axisymmetric poloidal (PME) and toroidal (TME) components, and nonaxisymmetric components (FME)). Here there are some surprises given what we just discussed for their KE counterparts MCKE, DRKE and FKE. First, the axisymmetric poloidal component PME contributes more to total ME than MCKE contributes to KE. It often represents a few percent of ME, and in one case, M11R5m, it is even found to be dominant. Interestingly, PME is found to reach its lowest values for intermediate rotators close to the $Ro_F = 1$ regime. In $Ro_F > 1$, we find that PME rises again, confirming the trend we observed on the total magnetic flux in

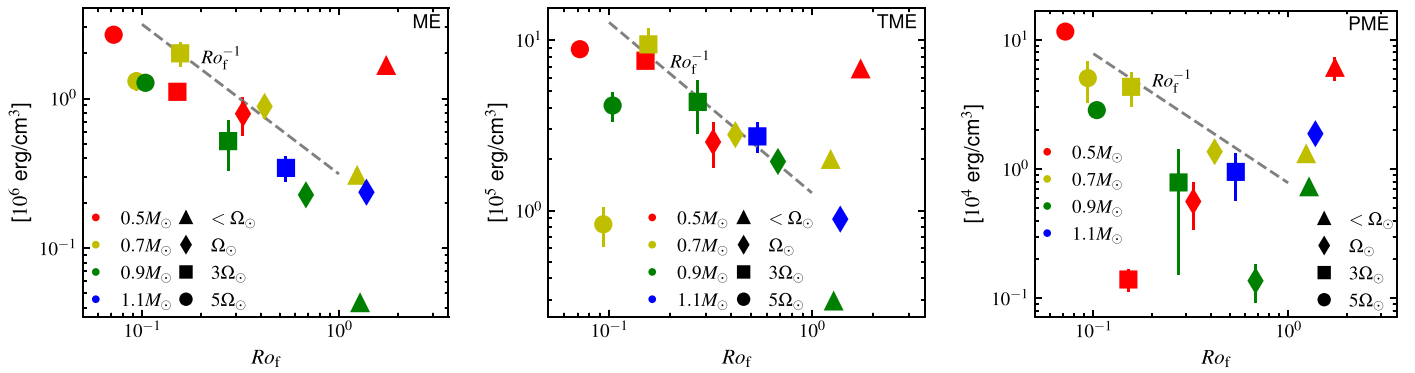


Figure 19. Total energy density in the convective envelope of our models, shown as a function of the fluid Rossby number. The magnetic energy (ME), toroidal magnetic energy (TME), and poloidal magnetic energy (PME) are displayed from left to right. The dashed gray lines indicate the Ro_f^{-1} trend.

Section 5.4. TME somewhat follows DRKE: it first increases with rotation rate, with more and more energy being pumped by the large-scale shear into toroidal ME via the dynamo Ω effect and also via complex convective motions. TME can reach values between 80% and 85% of the total ME. However, the Lorentz force feedback is so strong past a certain point that the large shear is quenched (the feedback destroying its generating source). In most of these highly rotationally constrained cases, the magnetic energy is found in the nonaxisymmetric magnetic field. These trends are also illustrated in Figure 19. It is worth noting that the three magnetic energies show an overall similar trend: the total energy density ME decreases with increasing Rossby number until $Ro_f \simeq 1$. The four models at $Ro_f > 1$ then exhibit a large scatter, and only PME shows an unambiguous increase with Rossby number in this regime. We also see a hint of a saturation and possibly a slight decrease of TME at low Rossby numbers. Additional simulations at even lower Rossby numbers are required to confirm this trend, which is to be expected based on the observed saturation of magnetic activity for fast rotators (see, e.g., Wright et al. 2011; Reiners et al. 2014). In all panels, we have indicated the inverse Rossby number trend as a gray dashed line. We remark that the three magnetic energy densities are all compatible with the Ro_f^{-1} trend at intermediate Rossby number, as expected from standard dynamo scaling laws in this regime (see Augustson et al. 2019). This translates into a bulk magnetic field $B_{\text{bulk}} \propto \text{ME}^{1/2} \propto Ro_f^{-0.5}$. We note that this scaling does not necessarily translate into the same scaling for the surface large-scale magnetic field, as will be made clear in Section 7.

The relative energies (shown as percentages in Table 5) also present interesting trends. We note first that in the slowly rotating cases, ME is only a few percent of KE. As we lower Ro_f , this value increases to reach equipartition by a subtle combination of both ME increasing while KE first increases and then decreases, as we have just seen. These variations inevitably lead to the fact that for the fastest rotating cases ME is even larger than KE and the simulations are in a so-called global super-equipartition state. This is very interesting, because it means that the kinetic energy in the convective envelope is not the maximal value that the ME can reach. This is due to a change in the force balance in the Navier–Stokes equation between the Lorentz, inertia, buoyancy, and Coriolis forces. As the rotation rate is increased and the Coriolis force becomes stronger and stronger, the balance at first shifts from being between mostly inertia and Lorentz force to a magnetostrophic state that implies a balance between Lorentz

and Coriolis forces. We refer the reader to these following studies for more detailed discussions of dynamo scaling laws (Christensen 2010; Davidson 2014; Oruba & Dormy 2014; Brun et al. 2015; Augustson et al. 2019).

Overall, we see that the dynamo states reached in our 15 cases do not show a strong difference as a function of mass, at least in the range studied here. However, both in terms of amplitude of the magnetic field and in the time variability of the magnetic field (cyclic, unsteady or steady solutions), we confirm that rotation plays a key role in determining the type of dynamo found in our simulations. We also note that the mean axisymmetric magnetic fields are not negligible in most of the models, often reaching values of 5% of the total energy content for the poloidal field and a large fraction for the toroidal magnetic field. For the latter, this has important consequences for the energy made available for the various magnetic phenomena occurring at the surface of solar-like stars (see Section 7).

Note that we did not look for hysteresis around the $Ro_f = 0.1$ limit by running various cases with different values of the seed magnetic field, as was done in some geophysical dynamo studies (Schinnerer et al. 2014). We consider stars to acquire their magnetic field through a complex formation process, in which the seed magnetic field is likely very weak (interstellar medium magnetic field amplitude are on averaged about 10–100 μG) and that starting the dynamo process with a weak seed field is the most likely scenario (Emeriau-Viard & Brun 2017). However, some studies have shown that weak and strong dynamo branches may exist under certain initial conditions (weak or strong seed magnetic field; Charbonneau 2004) or parameters such as the magnetic Prandtl number (Simitev & Busse 2009; Petitdemange 2018). Such weak or strong dynamo branches may explain some observed magnetic and rotational states seen in M dwarfs (Morin et al. 2011). Because this would depend on the local astrophysical context, we have decided to focus on the most common case of a weak seed magnetic field and refer the reader to these other complementary studies.

Having discussed how the KE and ME are distributed in our various models, we wish to go further in understanding exactly how these subtle balances come about. For this purpose we have computed the details of the energy transfers in our models, focusing on the mean axisymmetric components MCKE, DRKE, PME, and TME because large-scale fields and flows are of key astrophysical interest.

6.2. Main Transfer Mechanisms between Energy Reservoirs

In this section we discuss the various energy transfers occurring in a rotating magnetized convective envelope. We refer the reader to Appendix A for the detailed derivation of the energy transfer equations, in which we have followed Starr & Gilman (1966) and Rempel (2006), generalizing their derivation to global 3D spherical geometry. We focus here on the energy budget for the mean (axisymmetric) fields in the convective envelope of our models. We decompose energies into toroidal (along the azimuth) and poloidal (in the meridional plane) components. The budgets can be summarized as

$$\partial_t \text{DRKE} = \underbrace{\overbrace{Q_{\text{RS}}^{\text{DR}}}^{\text{Reynolds stress}}}_{\text{Reynolds stress}} \times \underbrace{\overbrace{-Q_{\text{MS}}^{\text{DR}}}^{\text{Maxwell stress}}}_{\text{Maxwell stress}} \underbrace{\overbrace{-Q_{\nu}^{\text{DR}}}^{\text{Viscosity}}}_{\text{Viscosity}} \underbrace{\overbrace{+C^{\text{DR}}}^{\text{Curvature}}}_{\text{Curvature}} \underbrace{\overbrace{-S^{\text{DR}}}^{\text{Boundaries}}}_{\text{Boundaries}}, \quad (17)$$

$$\partial_t \text{MCKE} = \underbrace{\overbrace{Q_{\text{RS}}^{\text{MC}}}^{\text{Reynolds stress}}}_{\text{Reynolds stress}} \times \underbrace{\overbrace{+Q_{\nabla P}}^{\text{Pressure work}}}_{\text{Pressure work}} \underbrace{\overbrace{+Q_b}_{\text{Buoyancy}}}_{\text{Buoyancy}} \underbrace{\overbrace{-Q_{\nu}^{\text{MC}}}^{\text{Viscosity}}}_{\text{Viscosity}} \underbrace{\overbrace{+C^{\text{MC}}}_{\text{Curvature}}}_{\text{Curvature}} \underbrace{\overbrace{-S^{\text{MC}}}_{\text{Boundaries}}}_{\text{Boundaries}}, \quad (18)$$

$$\partial_t \text{TME} = \underbrace{\overbrace{Q_{\Omega}}^{\text{Omega effect}}}_{\text{Omega effect}} \times \underbrace{\overbrace{-Q_{\text{TM}}^{\text{MC}}}^{\text{Mixed advection}}}_{\text{Mixed advection}} \underbrace{\overbrace{-Q_{\eta}^{\text{TM}}}^{\text{Ohmic diffusion}}}_{\text{Ohmic diffusion}} \underbrace{\overbrace{+C^{\text{TM}}}_{\text{curvature}}}_{\text{curvature}} \underbrace{\overbrace{-S^{\text{TM}}}_{\text{Boundaries}}}_{\text{Boundaries}}, \quad (19)$$

$$\partial_t \text{PME} = \underbrace{\overbrace{Q_{\text{PM}}^{\text{MC}}}^{\text{Mixed stresses}}}_{\text{Mixed stresses}} \times \underbrace{\overbrace{-Q_{\eta}^{\text{PM}}}^{\text{Ohmic diffusion}}}_{\text{Ohmic diffusion}} \underbrace{\overbrace{+C^{\text{PM}}}_{\text{Curvature}}}_{\text{Curvature}} \underbrace{\overbrace{-S^{\text{PM}}}_{\text{Boundaries}}}_{\text{Boundaries}}, \quad (20)$$

where all the different terms are detailed in Appendix A. We have computed individually each of the terms and show them normalized to the stellar luminosity in Figure 20, as a function of the fluid Rossby number of the models. For each model, we have averaged the balances (17)–(20) over typically 100 convective turnover time τ_c such that the sum of the terms is close to zero. Cyclic cases show large variations of the energy balance (we return to this point hereafter); in these cases, we averaged on a shorter time span chosen at cycle maximum. In addition, we have tabulated the transfers for three representative cases in Table 6 in units of both $\%L_{\star}$ and $\%L_{\odot}$.

The DR (upper-left panel of Figure 20) is always sustained primarily by Reynolds stresses in the models (as discussed in Section 4.2), with a dominant contribution of the radial

component $\overline{v_r'v_{\phi}'}$ over the latitudinal component $\overline{v_{\theta}'v_{\phi}'}$. The cases exhibiting antisolar DR (Rossby number larger than 1) present a reversal of the latter term, showing that the latitudinal component of the Reynolds stress is detrimental to the DR KE in these cases. The magnetic contributions Q_{Ω} (blue) and $Q_{\text{MS}}^{\text{DR}}$ (red) start playing a significant role for fast-rotating cases (low Rossby numbers; see model M07R5m in Table 6), sometimes even dominating completely viscous dissipation (Q_{ν}^{DR} , purple). In all cases the magnetic contributions tend to oppose the DR, as seen in Section 4.1. The power associated with the maintenance of DR can reach about 30% of the stellar luminosity and drops at minimum to about 4% in our sample of models. We remark that simulations with fluid Rossby numbers around $Ro_f \sim 0.2$ achieve the most powerful maintenance of DR that can reach values up to 17% of the solar luminosity. At larger Rossby numbers, the star does not rotate fast enough and the DR is weakly maintained. At lower Rossby numbers, the magnetic feedback from the dynamo field is so efficient that the power associated with the maintenance of DR decreases significantly.

The meridional circulation energy balance (upper right panel of Figure 20) is dominated by a balance between the work of pressure ($Q_{\nabla P}$, cyan), buoyancy (Q_b , blue-green) and Coriolis (Q_c , green) forces (see also Table 6 where the dominant transfer terms are highlighted in bold font). The latter almost always remains negative, indicating an energy transfer from the meridional flow to the DR when models are in a steady state. Viscous dissipation (purple) plays a much lesser role for MCKE compared to DRKE, and magnetic contributions can be considered as negligible, except maybe for small Rossby number cases possessing transequatorial meridional cells (see Figure 10). We find that the relative contribution of buoyancy and pressure gradients varies from model to model and also varies in time for each model. We believe that is due to the anelastic approximation used in this study, and expect that a Lantz–Braginsky formulation (Brown et al. 2012) would lead to more systematic relative contributions of these two important terms for MCKE. Finally, we note that the power associated with the meridional circulation maintenance increases with Rossby number and does not go above 15% of the stellar luminosity in our sample.

Let us now turn to the power sustaining magnetism in our models. The toroidal (TME) and poloidal (PME) magnetic energy budgets are shown in the left and right lower panels of Figure 20. We immediately note that the power sustaining magnetism corresponds at maximum to 3% of the stellar luminosity in our sample for TME. This corresponds to an absolute maximum of 6% of the solar luminosity. A very large amount of power is therefore indeed channeled to sustain the large toroidal ME reservoir that the dynamo builds up in the simulations. Hence, it is expected that a significant proportion of this large magnetic energy reservoir will be accessible to trigger various surface magnetic activity events (Shibata et al. 2013). The power associated with PME is a bit weaker but still reaches up to 0.4% of the stellar luminosity. We find again that the most powerful transfers occur around $Ro_f \sim 0.2$. The power involved saturates for lower Rossby numbers, which is reminiscent of the saturation of magnetic activity observed in the X-ray luminosity of fast-rotating stars (e.g., Wright et al. 2011). It slowly drops for large Rossby numbers, but the power maintains a value of at least 0.01% of the stellar luminosity even in our most slowly rotating models. These figures are in

Table 6

Dominant Energy Transfer Terms for Three Representative Cases (M07R5m—Low Rossby Number, M09R3m—Moderate Rossby Number, and M09R1m—High Rossby Number)

	M07R5m		M09R3m		M09R1m	
	[% L_*]	[% L_\odot]	[% L_*]	[% L_\odot]	[% L_*]	[% L_\odot]
$-Q_C$	0.38	0.06	2.96	1.63	1.35	0.75
Q_{RS}^{DR}	4.55	0.61	12.06	6.63	6.93	3.86
$-Q_\nu^{DR}$	-0.53	-0.08	-13.97	-7.69	-7.43	-4.08
$-Q_\Omega$	-0.43	-0.06	-0.84	-0.46	-0.004	-0.002
$-Q_{MS}^{DR}$	-3.84	-0.58	-0.70	-0.39	-0.05	-0.03
C^{DR}	0.20	0.03	-0.26	-0.14	-0.50	-0.28
Q_C	-0.38	-0.06	-2.96	-1.63	-1.35	-0.75
Q_{RS}^{MC}	0.15	0.02	0.29	0.16	0.15	0.08
$-Q_\nu^{MC}$	-0.08	-0.01	-0.83	-0.46	-1.17	-0.64
$Q_{\nabla P}$	1.36	0.20	2.65	1.46	2.17	1.20
$-Q_b$	-0.87	-0.13	0.50	0.28	0.29	0.16
Q_{MS}^{MC}	-0.17	-0.03	-0.03	-0.02	-0.002	-0.001
C^{MC}	-0.01	-0.001	0.19	0.10	0.01	0.01
$-Q_\eta^{TM}$	-0.44	-0.07	-0.54	-0.29	-0.004	-0.002
Q_{emf}^{TM}	0.11	0.02	0.06	0.04	0.008	0.005
Q_Ω	0.43	0.06	0.84	0.46	0.004	0.002
$-Q_\eta^{PM}$	-0.40	-0.06	-0.20	-0.11	-0.003	-0.002
Q_{emf}^{PM}	0.42	0.06	0.27	0.15	0.005	0.003

Note. The strongest transfers for each case and each energy are identified in bold font. The four blocks of rows correspond in order to (i) the differential rotation kinetic energy balance (Equation (17)), (ii) the meridional circulation kinetic energy balance (Equation (18)), and (iii) the toroidal magnetic energy balance (Equation (19)) and the poloidal magnetic energy balance (Equation (20)). Some transfer terms are tiny and have thus been omitted from the table.

7. Astrophysical Implications and Conclusion

We have shown in the previous sections how various magnetic properties of solar-type stellar dynamo simulations change as a function of stellar mass and rotation. Often such variations can be understood by using the Rossby number as a key control parameter. We here wish to reflect upon these findings and their astrophysical implications. There are several properties of solar-like stars such as their convective power and spectra, rotation profile, level of activity, and presence of a magnetic cycle, to cite only a few, that are of keen interest to be characterized. Our set of simulations can help us discuss some of these properties and provide clues to understand the physical mechanisms acting behind them.

Take, for instance, their interior rotation profile. We have seen in Section 4 that various states can be achieved in our set of simulations. We have further confirmed that such states depend on the Rossby numbers of the simulations. In Brun et al. (2017), it was advocated, based on the hydrodynamic counterpart of the dynamo cases studied here, that three states of internal rotation could be found: solar like (fast equator, slow poles), Jupiter like (cylindrical profile with alternations of prograde and retrograde zonal jets), and antisolar like (slow equator, fast poles). How is the presence of a self-sustained dynamo field changing this statement? We find that two states are retained: solar like and antisolar, and that the third one found for small Rossby numbers has been replaced by a new state. Indeed, we find that as the Rossby number decreases, the

feedback of the Lorentz force on the convective motion (via Maxwell stresses opposing Reynolds stresses in the angular momentum transport balance) yields smaller angular velocity contrast. This comes about because the rotation state tends toward uniform rotation (see Section 4). So for very small Rossby numbers, cases such as M11R5m or M09R5m are mostly showing a solid-body rotation in their convective envelope, in sharp contrast with the banded profile of their hydrodynamics counterpart. However, the disappearance of the cylindrical banded DR state may be due to the range of Reynolds and magnetic Reynolds numbers considered in our study. The strong Lorentz force feedback may be due to our moderate state of turbulent convection. It is possible that at higher Reynolds numbers, a cylindrical state would be retained even for a state near super-equipartition between KE and ME. This is a point that needs to be investigated further with a dedicated low Rossby/high Reynolds numbers study. Said differently: is there a level at which the magnetic energy contained in the convective envelope is so high that quasi-uniform internal rotation is inevitable? We believe this is a reasonable assumption given the tendency of the magnetic field to quench DR as identified by many authors (Glatzmaier & Gilman 1982; Charbonneau 2004; Brun et al. 2005; Karak et al. 2015; Warnecke & Käpylä 2020, and references therein). So, in summary, we find that the likely rotation states of solar-type stars depend on their increasing Rossby number: quasi-uniform, banded/cylindrical, solar like, and antisolar. Such variations of the DR states translated into an overall variation of the surface angular velocity contrast being less sensitive to the bulk rotation rate, with $\Delta\Omega \propto \Omega^{0.46}$, down from $\Omega^{0.66}$ as in Brun et al. (2017). We also find another potential interesting property for the DR of solar-like stars: a scaling law may not be the best fit to our simulations database. As in Saar (2011), we find that there is a clear change of trend for small Rossby numbers (see Figure 8). This is interestingly the change of rotation state from solar to almost uniform rotation. Determining for these various rotation states the exact transition in Rossby number will require more numerical study at higher levels of turbulence and continued dedicated observations. We intend to contribute to this effort with dedicated new simulations but also in preparing the scientific exploitation of PLATO (Rauer et al. 2014).

These various transitions of rotation profiles must impact the resulting dynamo and field properties. We have shown in the paper (Sections 5 and 6) that this is indeed the case. Going from low to high Rossby numbers, we find that dynamo action yields short-cycle, long-cycle, and statistically steady (yet irregular) magnetic field evolution. This is very interesting because we can guide observations to search for these transitions in rotation state or temporal variability of the magnetic field. This will also help us discriminate between various dynamo scenarios.

Our set of dynamo solutions can help us characterize the mechanisms at work to generate and maintain magnetic fields for different sets of global stellar parameters. The rich range of magnetic phenomena occurring in stars relies on the free energy available in magnetic structures created by dynamo mechanism. In this study we have focused our analysis on a key aspect of the convective dynamo: energy transfers. We have done an extensive study on how the energy flows to and from the KE and ME reservoirs, separating them into their toroidal and poloidal components. The first key result is that a

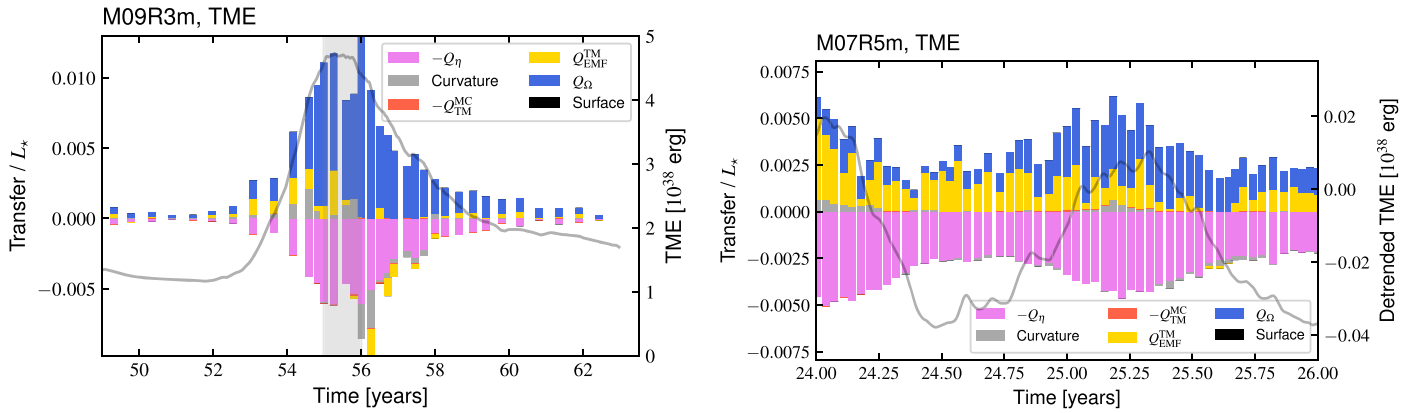


Figure 21. Energy budget as a function of time for model M09R3m. The labels are the same as the lower left panel in Figure 20. The toroidal magnetic energy (TME) is shown by the black line. The gray area in the left panel corresponds to the time-average interval used for M09R3m in Figure 20.

significant amount of the star’s luminosity is being transferred into KE and ME. In Table 6 we listed as a function of the star luminosity (also with respect to the solar one) the amount of accessible energy. We demonstrated that typical numbers for the KE contained in the DR are of order 10%, for the meridional circulation 1% of the star’s luminosity. We also showed that for the TME, the energy available is also around 1% (with a maximum of 3%) and of the order of 0.1% for the PME. Having access to 1% of the star luminosity to power stellar magnetism via collective emergence of toroidal structures is significant. This means that there is large reservoir of ME accessible for the manifestation of various magnetic phenomena at the star’s surface. We find for instance that our modeled stars can power dynamos such that they reach a global ME content from 10^{37} to 10^{39} erg. Part of this energy is found to be stored in the mean TME (up to 6×10^{38} erg), and the mean PME is generally found to be much less energetic (reaching at most 4×10^{37} erg). The corresponding total (unsigned) magnetic flux Φ_{tot} is found to vary between 10^{24} and 10^{25} Mx over the range of mass and rotation covered by our study, thus very similar to observations of the Sun and other solar-type stars. In dynamo cases with long cycles such as case M09R3m, Φ_{tot} is found to vary by a factor between 7 and 8 (see Figure 16), which is slightly more than what is found for the Sun (a factor of about 5 has been found for cycle 21 Schrijver & Harvey 1994).

We also found that Φ_{tot} follows a scaling law with the Rossby number $\Phi_{\text{tot}} \sim R_{\text{of}}^{-0.88}$ in qualitative agreement with observations (see Figure 17).

Another interesting finding of our study, which confirms results published in Augustson et al. (2015) with the same ASH code and in Strugarek et al. (2017, 2018) with the Eulag-MHD code, is the existence of a so-called nonlinear cyclic dynamo. Of course, convective dynamos are nonlinear in essence but what is meant here is that through the feedback of the Lorentz force on the flow, a cyclic behavior of the dynamo arises. Standard kinematic $\alpha - \Omega$ mean-field dynamos follow the Parker–Yoshimura (P–Y) rule (Parker 1955; Yoshimura 1975) and do not take into account nonlinear retroaction or do so in a limited way via the so-called Malkus–Proctor approach (Covas et al. 2005; Bushby 2006; Lopes et al. 2014, and references therein). By contrast, more and more 3D MHD convective dynamo simulations find that in a limited range of the parameter space, the P–Y rule does not apply anymore. This is the case in this study, where we find that for intermediate

values of the Rossby number, typically $0.15 \lesssim Ro_f \lesssim 0.65$, the long-cycle periods are due to a subtle interplay between the large-scale flow and the field. As the rotation rate is increased and the toroidal component of the dynamo-generated magnetic field becomes more and more dominant via an efficient Ω effect acting on the large-scale poloidal field, the associated Lorentz force starts to quench the DR via the action of Maxwell stresses opposing Reynolds stresses. This quenching of the DR in turn implies that the Ω effect is modified to the point that locally its latitudinal variation $\partial\Omega/\partial\theta$ reverses sign, leading to the generation of a toroidal field of opposite polarity, and through the action of turbulent convection, a reversed poloidal field. This nonlinear cyclic dynamo behavior is in sharp contrast with P–Y mechanism. Note that this is a delicate dynamo state to achieve, as the ME needs to be neither too weak nor too strong as discussed in Gilman (1983; see for instance their Figure 31 or in Brun et al. 2005 where such a modulated dynamo state was also found in stellar core dynamos). To demonstrate that further, we have computed in Figure 12 the P–Y rule for one typical long-cycle-period dynamo case of our study and confirm that it is unable to explain the dynamo wave and cyclic behavior of this subset of dynamo cases (M09R3m and M11R3m for instance). However, we do find that for low Rossby number ($Ro_f < 0.42$), the P–Y rule still works, and for instance in a case such as M07d5m also shown in Figure 12, we clearly have poleward dynamo waves compatible with the radial shear and the α effect. Hence, we may have been able in this study to identify when P–Y versus nonlinear cyclic dynamos (in the sense defined in this study, e.g., feedback of the magnetic field on the local shear) take place. This is very important as it tells us how to reconcile various recent publications in the community that sometimes were finding that global convective dynamo could be interpreted as classical $\alpha - \Omega$ dynamos (Viviani et al. 2018, 2019; Warnecke 2018, and references therein), whereas others did not (Augustson et al. 2015; Strugarek et al. 2017, 2018). We propose that it is linked to different effective values of the Rossby number used in these various dynamo simulations.

As we have seen above, it is instructive to make the link between full 3D MHD convective dynamo simulation and mean-field dynamo concepts. Mean-field dynamo theory usually uses the α effect to parameterize turbulent magnetic field generation. In this study, we have estimated it through both the kinetic helicity (see Appendix C and Pouquet et al. 1976) and an SVD decomposition (see Section 5.1,

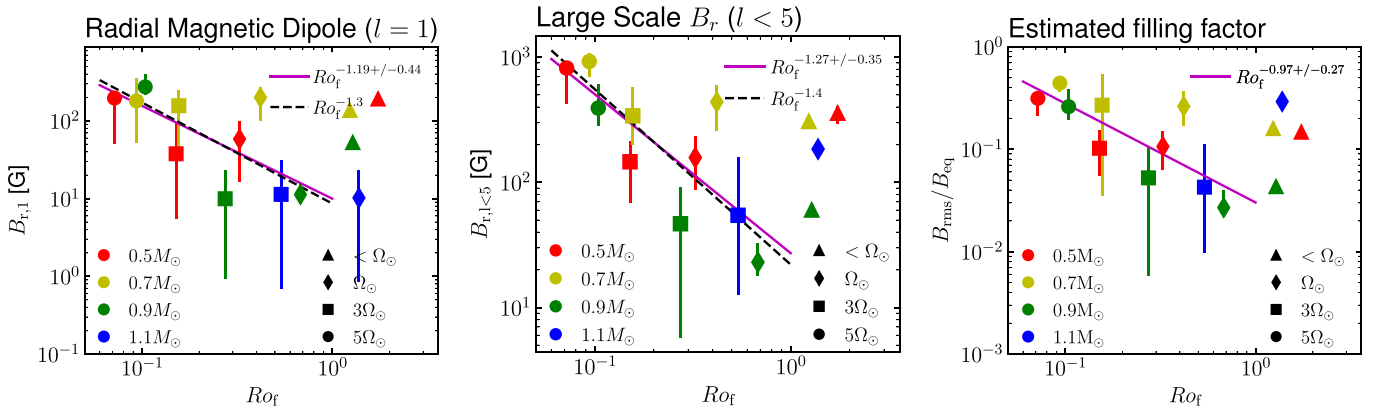


Figure 22. Large-scale field at the surface of our modeled convective envelopes as a function of the Rossby number. The first panel shows the total dipole field, the second panel the large-scale fields (spherical harmonics $\ell < 5$, including the nonaxisymmetric components ($m \neq 0$)). The third panel shows the ratio between the total rms field at the surface and the equilibrium field based on the gas pressure at the photosphere. It can be considered as a measure of the filling factor f (see Cranmer & Saar 2011; See et al. 2019b). The symbols used in the panels are the same as in Figure 7.

Appendix B, and Racine et al. 2011; Dubé & Charbonneau 2013; Augustson et al. 2015; Emeriau-Viard & Brun 2017). In the former case, we do not find a significant change of sign nor amplitude in the kinetic helicity of models possessing an antisolar DR. In the range of parameters considered in this study, this means that antisolar-like stars need to be modeled with an α effect similar to solar-like stars at least in their radial dependency, if not in amplitude (see detailed discussion in Noraz et al. 2021). In the mean-field $\alpha - \Omega$ dynamo paradigm this implies that antisolar-like stars will have a dynamo wave with a propagation reversed to that of the Sun, e.g., poleward from the equator to midlatitudes as imposed by the P-Y rule. In our 3D simulations, we do not find such cyclic poleward dynamos for slowly rotating simulations; instead, we find that they are statistically steady (but highly time dependent on short timescales). This is likely due to a less favorable phasing between poloidal and toroidal magnetic field generation in the convective envelope of these slowly rotating case that develops via complex nonlinear interactions between the fields and flows, which are not fine-tuned but instead evolves depending on the global parameters considered.

Another interesting aspect is to assess how the dynamo-generated magnetic field is distributed over spatial scales. It is well known that there is a nonlinear feedback loop between rotation, dynamo, stellar wind, and magnetic braking over secular timescales (Skumanich 1972; Brown 2014; Matt et al. 2015; Brun & Browning 2017; Metcalfe & van Saders 2017; Brun 2020; Vidotto 2021). It has been demonstrated that the magnetic torque provided by stellar winds is mostly controlled by the dipolar and quadrupolar modes (Garraffo et al. 2015; Réville et al. 2015; Finley & Matt 2018). Hence, one key question is to assess what happens with dipolar and quadrupolar modes when the dynamo changes its properties. To this end, we showed in Figure 18 how magnetic geometry changes by computing quantities known as f_{dip} and f_{quad} . This allows us to assess the overall contribution of these two dynamo modes to the overall magnetic energy spectra. We found that they are key contributors to the overall magnetic energy with values ranging from 0.05 to 0.6, with most of the cases studied possessing f_{dip} and f_{quad} around 0.2–0.3. We do not see any clear trend with Rossby number. Fast rotators and slow rotators both possess large dipolar and quadrupolar components. So from a stellar dynamo point of view, it is

difficult to invoke a drop in the large-scale magnetic field to explain a possible break of stellar spin-down for slow rotators as proposed by Metcalfe & van Saders (2017). Similar findings are obtained from observations of magnetic fields in cool stars as shown in Vidotto et al. (2016). The advocated Rossby number transition in magnetic field geometry to explain a collapse of magnetic braking is thus unlikely. This study suggests that we must find a different explanation, maybe a less efficient heating mechanism inducing a sudden drop of coronal temperature and wind mass loss (Ó Fionnagáin & Vidotto 2018), which directly impacts angular momentum loss. Self-consistent rotating wind models with detailed treatment of the coronal heating mechanism are needed (see, for instance, Shoda et al. 2020; Hazra et al. 2021) in order to confirm the existence or not of such a transition in mass loss at slow rotation rates.

We have focused our analysis on the global energetics of the dynamo, and showed that the global dynamo field followed roughly a $B_{\text{bulk}} \simeq Ro_f^{-0.5}$ trend (see Section 6.1) in agreement with previously published dynamo scaling laws (Augustson et al. 2019). It is also useful to interpret our simulations only considering the top of the dynamo domain, making a more direct link with stellar observations of the surface magnetism. In this context, we show in Figure 22 the trend in Rossby number for the surface dipole field (first panel), surface large-scale field (second panel, see Table 5), and the ratio of the root-mean-square (rms) surface field to the equipartition field (third panel). The error bars were deduced from the temporal variability of the fields, and the values are reported in Table 4. The first striking observation is that the scaling law of the surface large-scale field differs from the global volume-averaged dynamo field e.g., including all scales with a steeper slope. Indeed, we find for low and intermediate Rossby numbers that

$$B_{r,\text{dip}} \simeq 10 Ro_f^{-1.16 \pm 0.47} \text{ G}, \quad (21)$$

$$B_{L,\text{surf}} \simeq 28 Ro_f^{-1.27 \pm 0.35} \text{ G}. \quad (22)$$

Both trends are compatible with the trends deduced from the Zeeman–Doppler imaging surveys, which generally find the large-scale surface magnetic field to follow an $Ro_f^{-1.3}$ trend at intermediate Rossby numbers (See et al. 2019a). Finally, it is also instructive to assess the level of equipartition at the surface

through the ratio between the surface rms field B_{rms} and the equipartition field B_{eq} (as defined in Johns-Krull & Valenti 2000) deduced here from the gas pressure at the surface of the stellar models we considered. Indeed, Cranmer & Saar (2011) have proposed that this ratio measures the filling factor f of the large-scale field that shapes the lower stellar corona and ultimately determines the angular momentum loss rate of stars. See et al. (2019b) have found observationally that this ratio decreases with Rossby number. We find a similar trend here as seen in the third panel of Figure 22, with $f \simeq B_{\text{rms}}/B_{\text{eq}} \simeq 0.03 Ro_f^{-0.97 \pm 0.27}$. Finally, we note that the three magnetic field measures shown in Figure 22 all exhibit an increase in amplitude at high Rossby number. This again strengthens the case that dynamo action within cool stars does not exhibit any significant decrease of the large-scale magnetic field for slow rotators.

How are these results informing us about our star, the Sun? First, we note that the study of Strugarek et al. (2017, 2018) is about 1 solar mass stars and is taken into account in the analysis presented in this study. Given the good agreement seen in many of the plots discussed in Section 5 between the study done with the Eulag-MHD code and the one presented here with the ASH code (independently of models details), we are confident that the dynamo solutions discussed in this study are useful to understand the physical nature of the cyclic activity of a 1 solar mass star such as the Sun. Second, in this parametric stellar dynamo study we are proposing that in order to get both a solar-like conical DR and a deep slow decadal-long magnetic cycles, the Rossby number must be between 0.15 and 0.65. Hence, we here acknowledge that cases M09R1m and M11R1m rotating at the solar rate do not show behaviors that are Sun like with respect to their magnetic activity (no cycles present) because their Rossby number is not falling in the 0.15–0.65 range. Instead, we believe that M09R3m or M11R3m are better, closer representations of the Sun even though their rotation rate is faster than the Sun, because their Rossby number is in the correct range of values. This means that while the overall trends found in our study are robust, the specific location of any given star must be thought with extreme care due to the so-called convective conundrum, i.e., a mismatch between global convection simulations and solar helioseismic inversion regarding the amplitude of giant convection cells (Hanasoge et al. 2016; Hotta & Kusano 2021). This is likely due to the fact that for any given rotation rate, because of the convective conundrum, the Rossby number achieved in the rotating convection simulation is slightly too large. So in order to be likely closer to the solar state and to aim for the correct value of the solar Rossby number, models rotating faster such as the M09R3m or M11R3m cases are somewhat a better match to model the Sun than M09R1m or M11R1m. Thanks to this knowledge, we will next build a new global convective dynamo model of the Sun with an improved set of parameters by keeping the rotation rate to the solar one while controlling the effective Rossby number achieve in the simulation to be in the right range of values. We will report our finding in a future work.

To conclude, our study has confirmed the richness of dynamo solutions in parameter regimes that are likely to be found in solar-like stars and the large amount of magnetic energy and flux made available to the star and its surface activity by dynamo action. We have also identified the Rossby

number regimes for different realizations of DR profiles and magnetic temporal modulations (cyclic or not), generalizing in an MHD context what we published in Brun et al. (2017). Two key transitions in parameter space seem to be present, one at low Rossby number ($Ro_f < 0.1$), another at high Rossby number ($Ro_f > 1$). We need to study them with even more detail and at higher resolution and turbulence level to confirm the trends and scaling laws we have reported here. We intend to do so in the near future as well as study in more detail the influence of a realistic atmosphere and of a wind (Perri et al. 2021) on the dynamo properties.

We acknowledge partial financial support by DIM-ACAV+ ANAIS2 project, ERC Whole Sun Synergy grant #810218 and STARS2 starting grant #207430, ANR Toupies, INSU/PNST, Solar Orbiter, and PLATO CNES funds. We thank GENCI via project 1623 for having provided the massive computing resources needed to perform this extensive study. J.V. acknowledge Project 2019-T1/AMB-13648 and multiannual agreement with UC3M (“Excelencia para el Profesorado Universitario”—EPUC3M14)—Fifth regional research plan 2016–2020 founded by the Comunidad de Madrid. This work benefited from discussions within the international team “The Solar and Stellar Wind Connection: Heating processes and angular momentum loss,” supported by the International Space Science Institute (ISSI). A.S.B. is thankful to B.P. Brown, M. Derosa, N. Featherstone, B. Hindman, K. Shibata, S.-i Takehiro, and M. Yamada for useful discussions.

Appendix A Equation for Kinetic and Magnetic Energy Transfers in MHD Anelastic Systems

In this appendix we list the set of equations describing the energy transfer occurring in a star, focusing on mean energy quantities such as the poloidal and toroidal mean axisymmetric KE and ME. Following Starr & Gilman (1966), Brandenburg et al. (1996), De Rosa et al. (2002), and Rempel (2006), we derive the set of equations of full energy transfers in spherical MHD configurations.

Let us denote the azimuthal average by a bar and the derivation from it by a prime. For example, the radial velocity component will be written as $v_r = \bar{v}_r + v_r'$. In order to characterize the axisymmetric ME (\bar{E}_m) and KE (\bar{E}_k) transfers between the various reservoirs of energy (thermal, potential, kinetic, and magnetic) we will split \bar{E}_m and \bar{E}_k into three components:

$$\begin{aligned} \bar{E}_m &= \frac{1}{4\pi} (\bar{B}_r^2 + \bar{B}_\theta^2 + \bar{B}_\phi^2) \\ &= \underbrace{\frac{1}{4\pi} (\bar{B}_\phi^2)}_{\text{TME}} + \underbrace{\frac{1}{4\pi} (\bar{B}_r^2 + \bar{B}_\theta^2)}_{\text{PME}} + \underbrace{\frac{1}{4\pi} (\bar{B}_r'^2 + \bar{B}_\theta'^2 + \bar{B}_\phi'^2)}_{\text{FME}} \end{aligned} \quad (\text{A1})$$

$$\begin{aligned} \bar{E}_k &= \frac{\hat{\rho}}{2} (\bar{v}_r^2 + \bar{v}_\theta^2 + \bar{v}_\phi^2) \\ &= \underbrace{\frac{\hat{\rho}}{2} (\bar{v}_\phi^2)}_{\text{DRKE}} + \underbrace{\frac{\hat{\rho}}{2} (\bar{v}_r^2 + \bar{v}_\theta^2)}_{\text{MCKE}} + \underbrace{\frac{\hat{\rho}}{2} (\bar{v}_r'^2 + \bar{v}_\theta'^2 + \bar{v}_\phi'^2)}_{\text{FKE}} \end{aligned} \quad (\text{A2})$$

with DRKE and TME the mean axisymmetric toroidal energies, MCKE and PME the mean axisymmetric poloidal

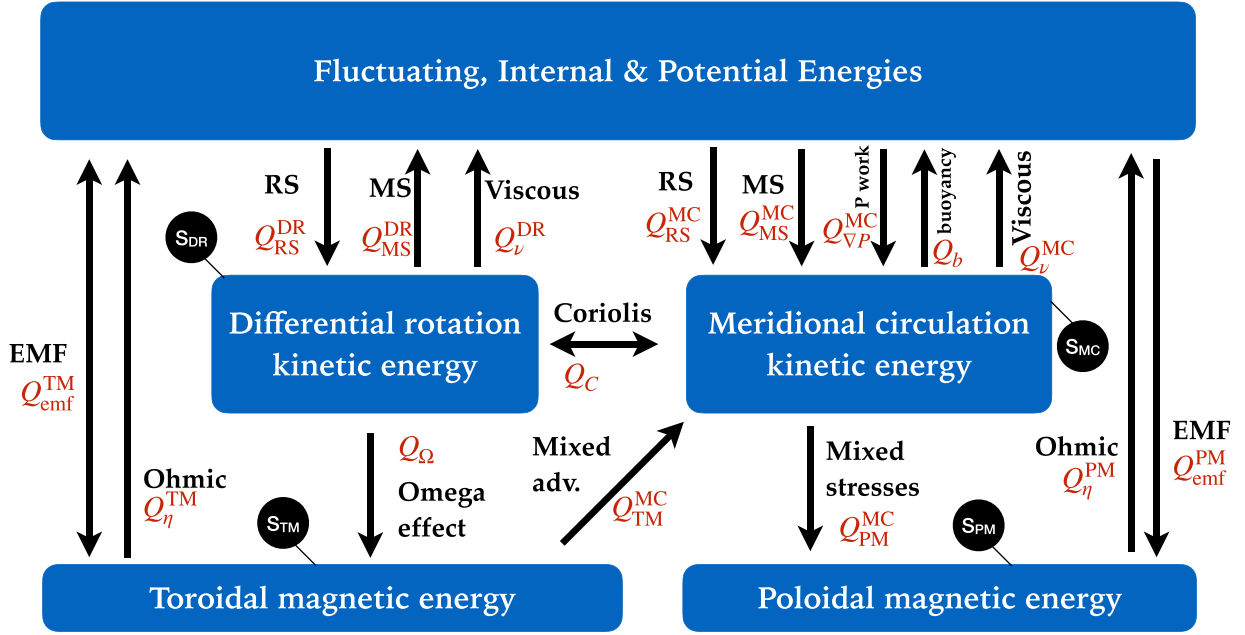


Figure 23. Global energy budget schematic. In red, we list all the key energy transport terms (see Appendix A). Black arrows correspond to the direction of transport between the various energy reservoirs. Surface terms are indicated as black disks. We omit curvature terms to avoid crowding the figure.

energies and FKE and FME the nonaxisymmetric energies. To find the energy transfer equation for these various components, we project the Navier–Stokes or induction equation onto the direction we wish to write the energy equation for, e.g., ϕ for TME for instance and inject the decomposition between the mean and prime quantities. Then we perform an azimuthal average, thereby eliminating all terms that are linear in prime quantities. For each energy equations, we then multiply by a bar quantity (for instance $\overline{B_\phi}$ for TME) and rearrange the terms. For MCKE and PME, we combine the radial and latitudinal equations. Doing so systematically leads to the following set of equations.⁶

A.1. Overall Energy Budgets

We follow the approach of Starr & Gilman (1966) and write the energy budgets in the following way (see the schematic in Figure 23):

$$\partial_t \text{DRKE} = Q_{RS}^{\text{DR}} - Q_\Omega - Q_C - Q_{MS}^{\text{DR}} - Q_\nu^{\text{DR}} + C^{\text{DR}} - S^{\text{DR}}, \quad (\text{A3})$$

$$\partial_t \text{MCKE} = Q_{RS}^{\text{MC}} + Q_{TM}^{\text{MC}} + Q_{MS}^{\text{MC}} + Q_{VP} + Q_C - Q_{PM}^{\text{MC}} - Q_b - Q_\nu^{\text{MC}} + C^{\text{MC}} - S^{\text{MC}}, \quad (\text{A4})$$

$$\partial_t \text{TME} = Q_\Omega + Q_{\text{emf}}^{\text{TM}} - Q_{TM}^{\text{MC}} - Q_\eta^{\text{TM}} + C^{\text{TM}} - S^{\text{TM}}, \quad (\text{A5})$$

$$\partial_t \text{PME} = Q_{PM}^{\text{MC}} + Q_{\text{emf}}^{\text{PM}} - Q_\eta^{\text{PM}} + C^{\text{PM}} - S^{\text{PM}}. \quad (\text{A6})$$

In all that follows, quantities are separated into mean and fluctuating components through

$$A = \bar{A} + A', \quad (\text{A7})$$

and the corresponding terms in the original derivation of Starr & Gilman (1966) are given in bold “SG66: [XX]” labels at the end of each equation, where XX is the term or equation number in Starr & Gilman (1966). Note that we have extra curvature terms C^x due to our choice of spherical coordinates.

A.2. Axisymmetric Differential Rotation Kinetic Energy Equation (DRKE)

The various terms of Equation (A3) are

$$Q_{RS}^{\text{DR}} = \int \hat{\rho} \left[v_r' v_\phi' \partial_r \bar{v}_\phi + v_\theta' v_\phi' \frac{1}{r} \partial_\theta \bar{v}_\phi \right] dV, \quad \text{SG66: [6c+6d]} \quad (\text{A8})$$

$$Q_\Omega = \int \frac{1}{4\pi} \overline{B_\phi} \left[\overline{B_r} \partial_r \bar{v}_\phi + \frac{\overline{B_\theta}}{r} \partial_\theta \bar{v}_\phi \right] dV, \quad \text{SG66: [5a+5b]} \quad (\text{A9})$$

$$Q_C = \int 2\Omega \hat{\rho} \bar{v}_\phi [\cos \theta \bar{v}_\theta + \sin \theta \bar{v}_r] dV, \quad \text{SG66: [6a+6b]} \quad (\text{A10})$$

$$Q_{MS}^{\text{DR}} = \int \frac{1}{4\pi} \overline{B_r' B_\phi'} \partial_r \bar{v}_\phi + \frac{1}{4\pi} \frac{\overline{B_\theta' B_\phi'}}{r} \partial_\theta \bar{v}_\phi dV, \quad \text{SG66: [7a+7b]} \quad (\text{A11})$$

$$Q_\nu^{\text{DR}} = \int \nu \hat{\rho} \left\{ \left[r \partial_r \left(\frac{\bar{v}_\phi}{r} \right) \right]^2 + \left[\frac{\sin \theta}{r} \partial_\theta \left(\frac{\bar{v}_\phi}{\sin \theta} \right) \right]^2 \right\} dV, \quad \text{SG66: [Fz]} \quad (\text{A12})$$

$$C^{\text{DR}} = \int -\frac{\hat{\rho} \bar{v}_\phi}{r} [\bar{v}_r \bar{v}_\phi + \cot \theta \bar{v}_\theta \bar{v}_\phi] + \frac{1}{4\pi} \frac{\bar{v}_\phi}{r} [\overline{B_r B_\phi} + \cot \theta \overline{B_\theta B_\phi}] dV, \quad (\text{A13})$$

⁶ Because we focus our study on the mean flows and magnetic fields, we will not show the equations for FKE and FME.

$$S^{\text{DR}} = -\frac{1}{4\pi} \int_{r=R_{\text{top}}} \overline{B_r B_\phi \overline{v_\phi}} dS. \text{ SG66: [Eq. 6].} \quad (\text{A14})$$

A.3. Axisymmetric Meridional Circulation Kinetic Energy Equation (MCKE)

Q_C was defined previously in Equation (A10). The remaining terms in Equation (A4) are

$$Q_{\text{RS}}^{\text{MC}} = \int \hat{\rho} \overline{v_r' v_\theta'} \left[\partial_r \overline{v_\theta} + \frac{1}{r} \partial_\theta \overline{v_r} \right] + \hat{\rho} \overline{v_r'^2} \partial_r \overline{v_r} + \hat{\rho} \overline{v_\theta'^2} \frac{1}{r} \partial_\theta \overline{v_\theta} dV, \text{ SG66: [3a+3b+3c]} \quad (\text{A15})$$

$$Q_{\text{TM}}^{\text{MC}} = \int \frac{1}{8\pi} \overline{B_\phi^2} \left[\frac{1}{r^2} \partial_r (r^2 \overline{v_r}) + \frac{1}{r \sin \theta} \partial_\theta (\sin \theta \overline{v_\theta}) \right] dV, \text{ SG66: [4a]} \quad (\text{A16})$$

$$Q_{\text{MS}}^{\text{MC}} = \int \frac{1}{8\pi} [-\overline{B_r'^2} + \overline{B_\theta'^2} + \overline{B_\phi'^2}] \partial_r \overline{v_r} + \frac{1}{8\pi} [\overline{B_r'^2} - \overline{B_\theta'^2} + \overline{B_\phi'^2}] \frac{1}{r} \partial_\theta \overline{v_\theta} - \frac{1}{4\pi} \overline{B_r' B_\theta'} \left[\partial_r \overline{v_\theta} + \frac{1}{r} \partial_\theta \overline{v_r} \right] dV, \text{ SG66: [8a]} \quad (\text{A17})$$

$$Q_{\nabla P} = \int - \left[\overline{v_r} \partial_r \overline{p} + \overline{v_\theta} \frac{1}{r} \partial_\theta \overline{p} \right] dV, \text{ SG66: [1a]} \quad (\text{A18})$$

$$Q_{\text{PM}}^{\text{MC}} = \int \frac{1}{4\pi} [\overline{B_r v_\theta} - \overline{v_r B_\theta}] \cdot \left[-\partial_r \overline{B_\theta} + \frac{1}{r} \partial_\theta \overline{B_r} \right] dV, \text{ SG66: [9a]} \quad (\text{A19})$$

$$Q_b = \int \hat{\rho} g \overline{v_r} dV, \text{ SG66: [2a]} \quad (\text{A20})$$

$$Q_\nu^{\text{MC}} = \int 2 \nu \hat{\rho} \left\{ \left[\partial_r \overline{v_r} - \frac{1}{3} (\nabla \cdot \mathbf{v}) \right]^2 + \left[\frac{1}{r} \partial_\theta \overline{v_\theta} + \frac{\overline{v_r}}{r} - \frac{1}{3} (\nabla \cdot \mathbf{v}) \right]^2 + \left[\frac{\overline{v_r}}{r} + \frac{\overline{v_\theta} \cos \theta}{r \sin \theta} - \frac{1}{3} (\nabla \cdot \mathbf{v}) \right]^2 + \frac{1}{2} \left[\frac{1}{r} \partial_\theta \overline{v_r} + r \partial_r \left(\frac{\overline{v_\theta}}{r} \right) \right]^2 \right\} dV, \text{ SG66: [Fm]} \quad (\text{A21})$$

$$C^{\text{MC}} = \int \frac{\hat{\rho}}{r} [\overline{v_r} (\overline{v_\theta^2} + \overline{v_\phi^2}) - \overline{v_\theta} (\overline{v_r v_\theta} - \cot \theta \overline{v_\phi^2})] - \frac{\overline{v_r}}{4\pi r} (\overline{B_\theta^2} + \overline{B_\phi^2}) + \frac{\overline{v_\theta}}{4\pi r} (\overline{B_r B_\theta} - \cot \theta \overline{B_\phi^2}) + \frac{1}{8\pi r} \overline{B^2} (2\overline{v_r} + \cot \theta \overline{v_\theta}) dV, \quad (\text{A22})$$

$$S^{\text{MC}} = -\frac{1}{4\pi} \int_{r=R_{\text{top}}} \overline{B_r' B_\theta' \overline{v_\theta}} dS. \text{ SG66: [Eq. 8].} \quad (\text{A23})$$

A.4. Axisymmetric Toroidal Magnetic Equation (TME)

Q_Ω and $Q_{\text{TM}}^{\text{MC}}$ were defined previously in Equations (A9) and (A16). The remaining terms in Equation (A5) are

$$Q_{\text{emf}}^{\text{TM}} = \int \frac{1}{4\pi} [\overline{B_\phi' v_r'} - \overline{B_r' v_\phi'}] \partial_r \overline{B_\phi} + \frac{1}{4\pi} [\overline{B_\phi' v_\theta'} - \overline{B_\theta' v_\phi'}] \frac{1}{r} \partial_\theta \overline{B_\phi} dV, \text{ SG66: [4b + 4c]} \quad (\text{A24})$$

$$Q_\eta^{\text{TM}} = \int -\frac{\overline{B_\phi}}{4\pi r} [\partial_r \{ \eta \partial_r (r \overline{B_\phi}) \} + \frac{\eta}{r} \partial_\theta \left\{ \frac{1}{\sin \theta} \partial_\theta (\sin \theta \overline{B_\phi}) \right\}] dV, \text{ SG66: [Jz]} \quad (\text{A25})$$

$$C^{\text{TM}} = \int -\frac{\overline{B_\phi}}{4\pi r} [\overline{B_r v_\phi} + \cot \theta \overline{B_\theta v_\phi} - (\overline{B_\phi v_r} + \cot \theta \overline{B_\theta v_\theta})] dV, \quad (\text{A26})$$

$$S^{\text{TM}} = -\frac{1}{4\pi} \int_{r=R_{\text{top}}} \overline{B_r' v_\phi' \overline{B_\phi}} dS. \text{ SG66: [Eq. 7].} \quad (\text{A27})$$

A.5. Axisymmetric Poloidal Magnetic Equation (PME)

$Q_{\text{MC}}^{\text{PM}}$ have already been defined in Equation (A19). The remaining terms in Equation (A6) are

$$Q_{\text{emf}}^{\text{PM}} = \int \frac{1}{4\pi} [\overline{B_r' v_\theta'} - \overline{B_\theta' v_r'}] \cdot \left[-\partial_r \overline{B_\theta} + \frac{1}{r} \partial_\theta \overline{B_r} \right] dV, \text{ SG66: [9b]} \quad (\text{A28})$$

$$Q_\eta^{\text{PM}} = \int \frac{\overline{B_r}}{4\pi r^2 \sin \theta} \eta \partial_\theta \{ \sin \theta [\partial_r (r \overline{B_\theta}) - \partial_\theta \overline{B_r}] \} - \frac{\overline{B_\theta}}{4\pi r} \partial_r \{ \eta [\partial_r (r \overline{B_\theta}) - \partial_\theta \overline{B_r}] \} dV, \text{ SG66: [Jm]} \quad (\text{A29})$$

$$C^{\text{PM}} = \int \frac{\overline{B_\theta}}{4\pi r} [\overline{B_\theta v_r} - \overline{B_r v_\theta}] dV, \quad (\text{A30})$$

$$S^{\text{PM}} = -\frac{1}{4\pi} \int_{r=R_{\text{top}}} \overline{B_r v_\theta \overline{B_\theta}} dS. \text{ SG66: [Eq. 9].} \quad (\text{A31})$$

Appendix B

Mean-field SVD Decomposition of Dynamo Solution

It is instructive to compare our 3D simulation results with the concepts used in mean-field dynamo theory (see Section 5). For instance, the generation of a poloidal magnetic field in the simulation is dominated by the action of the fluctuating EMF: $E_{\text{FI}} = \mathcal{E}' = \langle \mathbf{v}' \times \mathbf{B}' \rangle$. This process can also be interpreted through the α -effect approximation, which is a first order expansion of \mathcal{E}' around the mean magnetic field and its gradient:

$$\langle \mathcal{E}' \rangle_i = \alpha_{ij} \langle \mathbf{B} \rangle_j + \beta_{ijk} \partial_j \langle \mathbf{B} \rangle_k + \mathcal{O}(\partial \langle \mathbf{B} \rangle / \partial t, \nabla^2 \langle \mathbf{B} \rangle) \quad (\text{B1})$$

with α_{ij} a rank-two pseudo-vector and β_{ijk} a rank-three tensor. In the following, we will neglect the β term. However, this will increase the systematic error when estimating the α term. Thus,

a SVD including the β effect has been calculated in order to provide a lower-bound on the systematic error as discussed in Augustson et al. (2015). In the following analysis, α has been decomposed into its symmetric and antisymmetric components

$$\alpha \langle \mathbf{B} \rangle = \alpha_S \langle \mathbf{B} \rangle + \gamma \times \langle \mathbf{B} \rangle \quad (\text{B2})$$

with

$$\alpha_S = \begin{bmatrix} \alpha_{(rr)} & \alpha_{(r\theta)} & \alpha_{(r\varphi)} \\ \alpha_{(r\theta)} & \alpha_{(\theta\theta)} & \alpha_{(\theta\varphi)} \\ \alpha_{(r\varphi)} & \alpha_{(\theta\varphi)} & \alpha_{(\varphi\varphi)} \end{bmatrix} \quad \text{and} \quad \gamma = \begin{bmatrix} \gamma_r \\ \gamma_\theta \\ \gamma_\varphi \end{bmatrix}. \quad (\text{B3})$$

Thanks to the SVD decomposition we can quantify the relative efficiency of the α effect in generating the mean magnetic field and characterize the type of dynamo through the relative influence of its regenerating terms. We can start by evaluating how the convective flows regenerate mean magnetic fields. This can be determined by finding the amplitude of an estimated α effect relative to the rms value of the nonaxisymmetric velocity field

$$E \simeq \left\langle \frac{\alpha}{v_{\text{rms}}} \right\rangle = \frac{3}{2(r_{\text{top}}^3 - r_{\text{bcz}}^3)} \times \sum_{ij} \iint dr d\theta r^2 \sin \theta \sqrt{\frac{\alpha_{ij} \alpha^{ij}}{\{\mathbf{v}' \cdot \mathbf{v}'\}}} \quad (\text{B4})$$

where $\{\mathbf{v}' \cdot \mathbf{v}'\}$ is the sum of the diagonal elements of the Reynolds stress tensor averaged over time and over all longitudes. If we want to refine the analysis, we can use the Equation (B4) to provide a measure of the importance of each component of α as

$$\begin{aligned} \varepsilon_{ij} &= \frac{E_{ij}}{E} \\ &\simeq \frac{1}{E} \left\langle \frac{\alpha_{ij}}{v_{\text{rms}}} \right\rangle \\ &= \frac{3}{2E(r_{\text{top}}^3 - r_{\text{bcz}}^3)} \iint dr d\theta r^2 \sin \theta \sqrt{\frac{\alpha_{ij} \alpha^{ij}}{\{\mathbf{v}' \cdot \mathbf{v}'\}}} \\ &= \begin{bmatrix} \varepsilon_{(rr)} & \varepsilon_{(r\theta)} & \varepsilon_{(r\varphi)} \\ \varepsilon_{\gamma_\varphi} & \varepsilon_{(\theta\theta)} & \varepsilon_{(\theta\varphi)} \\ \varepsilon_{\gamma_\theta} & \varepsilon_{\gamma_r} & \varepsilon_{(\varphi\varphi)} \end{bmatrix} \end{aligned} \quad (\text{B5})$$

with $\varepsilon_{(xx)} = \frac{\alpha_{(xx)}}{E}$ and $E_{\gamma_x} = \frac{\gamma_x}{E}$. By calculating this matrix (see Table 7), we notice that for the antisymmetric part γ , the predominant term is γ_φ , which impacts the poloidal component of the magnetic field. Only for M07R5m are the three components of the same order of magnitude. In the three other cases shown, γ_r and γ_θ have roughly the same order of magnitude and are smaller by a factor 2 to 3 compared to γ_φ . By looking at the symmetric part α_S , we see the same trend. The predominant term is $\alpha_{(rr)}$ with $\alpha_{(r\theta)}$ and $\alpha_{(\theta\theta)}$ close second. They all act on the poloidal component of the magnetic field. The smallest term is in most cases $\alpha_{(\varphi\varphi)}$ which is at least five times smaller than the predominant term except once more in case M07R5m where it is of the same order of magnitude. The sum of all α terms varies between 51% in case M07R5m up to 73% in case M09R3m. Hence, the γ terms (the antisymmetric

Table 7
 $\alpha - \Omega$ Effects from SVD Decomposition

	α tensor	Ω/α_φ	α_P/α_φ		
M07R5m	0.120	0.092	0.073	19.7	12.4
	<i>0.155</i>	0.063	0.061		
	<i>0.220</i>	<i>0.119</i>	0.097		
M09R3m	0.246	0.194	0.088	7.0	1.59
	<i>0.166</i>	0.125	0.056		
	<i>0.042</i>	<i>0.053</i>	0.030		
M11R3m	0.174	0.157	0.087	5.53	3.18
	<i>0.162</i>	0.135	0.054		
	<i>0.075</i>	<i>0.109</i>	0.047		
M09R1m	0.209	0.120	0.112	1.81	4.31
	<i>0.157</i>	0.110	0.089		
	<i>0.067</i>	<i>0.099</i>	0.037		

Note. Results of the mean-field SVD dynamo analysis for four representative models (M07R5m, M09R1m, M09R3m, and M11R3m) ordered from top to bottom in increasing Rossby number values. The first column represents the α tensor with its symmetric: α_S and antisymmetric: γ (italic) portions (see Equation (B2)). The middle column gives the relative importance of the Ω effect to the α effect for the regeneration of the toroidal field. The last column quantifies the ratio of the α effect used for the regeneration of the poloidal magnetic field to the one used for the regeneration of the toroidal field.

part of the alpha tensor) account for 49% in case M07R5m down to 27% in case M09R3m.

In order to better quantify this relative influence we can compute the α_P/α_φ ratio:

$$\begin{aligned} \frac{\alpha_P}{\alpha_\varphi} &= \frac{3}{2(r_{\text{top}}^3 - r_{\text{bcz}}^3)} \\ &\times \iint dr d\theta r^2 \sin \theta \left| \frac{\langle \mathbf{B}_P \rangle \cdot \nabla \times \langle \mathcal{E}' \rangle}{\langle \mathbf{B}_\varphi \rangle \hat{\varphi} \cdot \nabla \times \langle \mathcal{E}' \rangle} \right|. \end{aligned} \quad (\text{B6})$$

Looking at Table 7 where we report the value of this ratio for all four representative models, we note the predominance of the poloidal field regeneration over the toroidal field regeneration for all models as the ratio α_P/α_φ is always above 1. This ratio varies from 1.59 in M09R3m up to 12.4 in case M07R5m.

Turning now to the regeneration of the toroidal field, we know from mean-field dynamo theory that it can be due to either the α effect coming from the fluctuating EMF \mathcal{E}' , or from the Ω effect that acts on the poloidal field through DR. In all our models, we note that the regeneration of $\langle \mathbf{B}_\varphi \rangle$ by the α effect is small, compared to the one of \mathbf{B}_{pol} . Therefore, we now want to measure the relative influence of the Ω effect to that of the α effect because the toroidal magnetic field can be regenerated through both effects:

$$\begin{aligned} \frac{\Omega}{\alpha_\varphi} &= \frac{3}{2(r_{\text{top}}^3 - r_{\text{bcz}}^3)} \\ &\times \iint dr d\theta r^2 \sin \theta \left| \frac{r \sin \theta \langle \mathbf{B}_\varphi \rangle \langle \mathbf{B}_P \rangle \cdot \nabla \langle \Omega \rangle}{\langle \mathbf{B}_\varphi \rangle \hat{\varphi} \cdot \nabla \times \langle \mathcal{E}' \rangle} \right|. \end{aligned} \quad (\text{B7})$$

We note that in all models the Ω effect is much stronger than the α effect in generating the toroidal magnetic field (the ratio Ω/α_φ is greater than 5), except for case M09R1m for which it is closer to 1. This confirms that most of the dynamo models considered in this study can be classified as $\alpha - \Omega$ dynamos rather than $\alpha^2 - \Omega$. Statistically steady simulations such as

M09R1m on the contrary are closer to be classified as $\alpha^2 - \Omega$. Of course, this mean-field dynamo classification is mostly useful for short magnetic cycle period cases (illustrated in the table with case M07R5m) as they also follow the P-Y rule (see Section 5). For long magnetic cycle period cases such as M09R3m and M11R3m, this is less significant, as we observe a complex nonlinear feedback that leads to a different type of cyclic dynamo. Further, we have shown in Section 6 and Figure 21 that these dynamo mechanisms are highly variable in time and can sometimes be quenched while at other times they become dominant. Hence, a mean-field classification on such solutions could vary depending on the dynamo phase considered.

Appendix C Kinetic Helicity in Solar and Antisolar Cases

In Figure 24 we display several realizations of the horizontally averaged radial profile of the kinetic helicity $H_k = \mathbf{v} \cdot \boldsymbol{\omega}$ in our set of convective dynamo models. These profiles have been averaged over the northern hemisphere only.

On the left panel we display the kinetic helicity profiles for the M05m series. We first note that the kinetic helicity is negative in most of the domain and changes sign at the bottom of the convective envelope and is close to zero in the deep radiative interior below. This sign reversal of H_k is understood by the change of sign of the vorticity field in the downward plumes. As they splash onto the top of the radiative zone (whose realistic stiffness we recall is directly taken from 1D stellar structure model, see Section 2), they diverge and this yields a change of sign of the local kinetic helicity (see Miesch et al. 2000 for a detailed explanation). Next, we can study how dynamo-generated magnetic field influences the kinetic helicity content of the convective shell. We do so by comparing the M05 dynamo cases to their hydrodynamic counterpart published in Brun et al. (2017) (dashed versus solid lines). We mostly find that magnetic fields tend to reduce the kinetic helicity content. In some rare cases we find it has little or no influence. In cyclic dynamo cases such as M05R3m we do not see a large influence of the cycle phase on the kinetic helicity content. This confirms that unless magnetic feedbacks are strong on the velocity and vorticity field (via the opposing/drag effect of Maxwell stresses in the converging and cyclonic

intersection of downflow lanes), this quantity is not modified much. In the middle panel, we show how the kinetic helicity evolves with a decreasing Rossby number. We illustrate this by plotting the radial kinetic helicity profiles of the M09m series (other mass bins display similar behavior). We see that as we increase the rotation rate from M09Sm to M09R1m and M09R3m, the peak amplitude near the surface becomes more and more negative (more cyclonic in the northern hemisphere, i.e., more right-handed). This seems to stop for case M09R5m. We believe this is due to the strong quenching of the DR and convection state due to the stronger feedback of Maxwell stresses in that case.

Finally, one important question, relevant to $\alpha - \Omega$ dynamo concepts, is how the kinetic helicity behaves in a high Rossby number regime, when the DR harbors an antisolar rotation profile. Indeed, we already know that in these cases, the gradients of Ω have a reversed sign. We also know that there is a relationship between the dynamo α effect and kinetic helicity. In the mean-field dynamo approach $\alpha = -\frac{\tau}{3} \mathbf{v} \cdot (\nabla \times \mathbf{v})$. Hence, knowing if the α effect would change sign or not, can yield interesting information on the dynamo properties (e.g., is there or not a breaking of symmetry). On the right panel of Figure 24, we display the kinetic helicity radial profiles for the slow-rotating cases, those with a high (greater than 1) Rossby number. Across the four mass bins, we see a clear increase in the amplitude of the kinetic helicity in an absolute sense (it becomes more negative near the surface of each model). This is linked to the fact that the velocity amplitude increases by more than one order of magnitude from the M05 to M11 series due to the increased stellar luminosity of the more massive cases. Moreover, even though these four cases (M05Sm, M07Sm, M09Sm, and M11R1m) have antisolar DR (see Figure 5) their kinetic helicity profile is similar to the solar-like cases (negative in the upper layers and positive at the base of the convective zone) as discussed in the two previous panels. This can be understood by the fact that all models still rotate in the same direction when considering their rotating frame. This means that the mean-field α effect is not expected to change sign when the DR (Ω effect) does. This conservation of the kinetic helicity sign when changing the Rossby number from greater to lower than 1 is confirmed when displaying the radial vorticity near the surface in two cases, M09S and M09R3 (not shown). The vortical nature of the

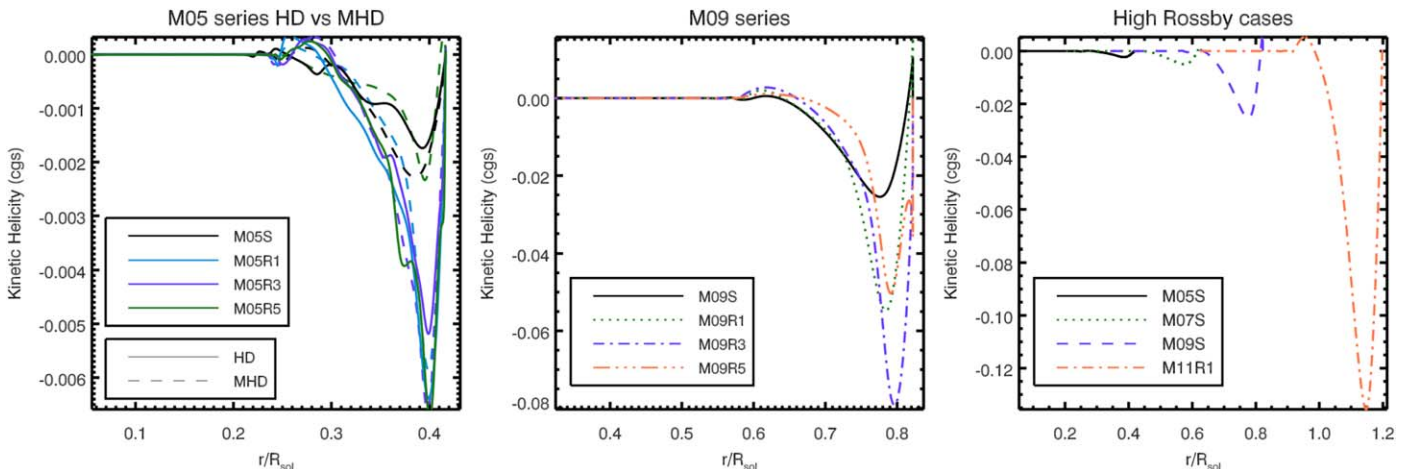


Figure 24. Radial kinetic helicity profiles in various models averaged over the northern hemisphere only. Left panel: comparing kinetic helicity for the M05 cases for both the hydrodynamic progenitors and the MHD dynamo runs. Middle panel: for decreasing Rossby number for M09 series. Right panel: for the $Ro_{\tau} > 1$ models spanning the four mass bins.

interstices of the downflow lanes (as illustrated with the enstrophy field in Figure 4) is not modified between the two models even though they possess the opposite profile to the DR. We note that there is some debate in the community whether to include or not a correction from the current helicity such that $\alpha_m = -\frac{\tau}{3}(\mathbf{v} \cdot (\nabla \times \mathbf{v}) - \frac{1}{c\rho} \mathbf{J} \cdot \mathbf{B})$ (see Pouquet et al. 1976; Brandenburg & Subramanian 2005). So, it could be the case where the kinetic helicity does not change sign, but that a correction from the current helicity may. We have assessed this point, and we find that the profile of the current helicity is less coherent as a function of depth and does not seem to modify the conclusion of our analysis.

ORCID iDs

Allan Sacha Brun  <https://orcid.org/0000-0002-1729-8267>
 Antoine Strugarek  <https://orcid.org/0000-0002-9630-6463>
 Quentin Noraz  <https://orcid.org/0000-0002-7422-1127>
 Barbara Perri  <https://orcid.org/0000-0002-2137-2896>
 Jacobo Varela  <https://orcid.org/0000-0002-6114-0539>
 Kyle Augustson  <https://orcid.org/0000-0003-4714-1743>
 Paul Charbonneau  <https://orcid.org/0000-0003-1618-3924>
 Juri Toomre  <https://orcid.org/0000-0002-3125-4463>

References

- Alvan, L., Brun, A. S., & Mathis, S. 2014, *A&A*, 565, A42
 Alvan, L., Strugarek, A., Brun, A. S., Mathis, S., & Garcia, R. A. 2015, *A&A*, 581, A112
 Anders, E. H., Manduca, C. M., Brown, B. P., Oishi, J. S., & Vasil, G. M. 2019, *ApJ*, 872, 138
 Aschwanden, M. J., Boerner, P., Ryan, D., et al. 2015, *ApJ*, 802, 53
 Augustson, K., Brun, A. S., Miesch, M., & Toomre, J. 2015, *ApJ*, 809, 149
 Augustson, K. C., Brun, A. S., & Toomre, J. 2013, *ApJ*, 777, 153
 Augustson, K. C., Brun, A. S., & Toomre, J. 2019, *ApJ*, 876, 83
 Baliunas, S. L., Donahue, R. A., Soon, W. H., et al. 1995, *ApJ*, 438, 269
 Balona, L. A., & Abedigamba, O. P. 2016, *MNRAS*, 461, 497
 Barnes, J. R., Collier Cameron, A., Donati, J.-F., et al. 2005, *MNRAS Lett.*, 357, L1
 Barnes, S. A. 2003, *ApJ*, 586, 464
 Barnes, S. A. 2007, *ApJ*, 669, 1167
 Barnes, S. A., Weingrill, J., Fritzewski, D., Strassmeier, K. G., & Platais, I. 2016, *ApJ*, 823, 16
 Basu, S., & Antia, H. M. 2019, *ApJ*, 883, 93
 Beaudoin, P., Simard, C., Cossette, J.-F., & Charbonneau, P. 2016, *ApJ*, 826, 138
 Benomar, O., Bazot, M., Nielsen, M. B., et al. 2018, *Sci*, 361, 1231
 Bice, C. P., & Toomre, J. 2020, *ApJ*, 893, 107
 Blackman, E. G., & Field, G. B. 2001, *PhPl*, 8, 2407
 Böhm-Vitense, E. 2007, *ApJ*, 657, 486
 Boro Saikia, S., Marvin, C. J., Jeffers, S. V., et al. 2018, *A&A*, 616, A108
 Brandenburg, A., & Giampapa, M. S. 2018, *ApJL*, 855, L22
 Brandenburg, A., Jennings, R. L., Nordlund, Å., et al. 1996, *JFM*, 306, 325
 Brandenburg, A., & Subramanian, K. 2005, *PhR*, 417, 1
 Broomhall, A. M., Chaplin, W. J., Elsworth, Y., & Simoniello, R. 2012, *MNRAS*, 420, 1405
 Brown, B. P., Browning, M. K., Brun, A. S., Miesch, M. S., & Toomre, J. 2008, *ApJ*, 689, 1354
 Brown, B. P., Browning, M. K., Brun, A. S., Miesch, M. S., & Toomre, J. 2010, *ApJ*, 711, 424
 Brown, B. P., Miesch, M. S., Browning, M. K., Brun, A. S., & Toomre, J. 2011, *ApJ*, 731, 69
 Brown, B. P., Vasil, G. M., & Zweibel, E. G. 2012, *ApJ*, 756, 109
 Brown, T. M. 2014, *ApJ*, 789, 101
 Browning, M. K., Miesch, M. S., Brun, A. S., & Toomre, J. 2006, *ApJL*, 648, L157
 Brun, A. S. 2004, *SoPh*, 220, 333
 Brun, A. S. 2020, *ASSP*, 57, 75
 Brun, A. S., Antia, H. M., Chitre, S. M., & Zahn, J. P. 2002, *A&A*, 391, 725
 Brun, A. S., & Browning, M. K. 2017, *LRSP*, 14, 4
 Brun, A. S., Browning, M. K., & Toomre, J. 2005, *ApJ*, 629, 461
 Brun, A. S., García, R. A., Houdek, G., Nandy, D., & Pinsonneault, M. 2015, *SSRv*, 196, 303
 Brun, A. S., Miesch, M. S., & Toomre, J. 2004, *ApJ*, 614, 1073
 Brun, A. S., Miesch, M. S., & Toomre, J. 2011, *ApJ*, 742, 79
 Brun, A. S., Strugarek, A., Varela, J., et al. 2017, *ApJ*, 836, 192
 Brun, A. S., & Toomre, J. 2002, *ApJ*, 570, 865
 Bushby, P. J. 2006, *MNRAS*, 371, 772
 Chabrier, G., & Küker, M. 2006, *A&A*, 446, 1027
 Charbonneau, P. 2004, in *IAU Symp.* 215, *Stellar Rotation* Vol. 215, ed. A. Maeder & P. Eenens (Cambridge: Cambridge Univ. Press), 366
 Charbonneau, P. 2020, *LRSP*, 17, 4
 Christensen, U. R. 2010, *SSRv*, 152, 565
 Christensen, U. R., & Aubert, J. 2006, *GeoJI*, 166, 97
 Clune, T. C., Elliot, J. R., Miesch, M. S., Toomre, J., & Glatzmaier, G. A. 1999, *ParC*, 25, 361
 Collier Cameron, A. 2007, *AN*, 328, 1030
 Covas, E., Moss, D., & Tavakol, R. 2005, *A&A*, 429, 657
 Cranmer, S. R., & Saar, S. H. 2011, *ApJ*, 741, 54
 Curtis, J. L., Agüeros, M. A., Matt, S. P., et al. 2020, *ApJ*, 904, 140
 Davidson, P. A. 2014, *GeoJI*, 198, 1832
 De Rosa, M. L., Gilman, P. A., & Toomre, J. 2002, *ApJ*, 581, 1356
 do Nascimento, J., García, R. A., Mathur, S., et al. 2014, *ApJL*, 790, L23
 do Nascimento, J. D. J., de Almeida, L., Velloso, E. N., et al. 2020, *ApJ*, 898, 173
 Donahue, R. A., Saar, S. H., & Baliunas, S. L. 1996, *ApJ*, 466, 384
 Donati, J.-F., & Collier Cameron, A. 1997, *MNRAS*, 291, 1
 Dubé, C., & Charbonneau, P. 2013, *ApJ*, 775, 69
 Egeland, R. 2017, PhD thesis, Montana State University, Bozeman, Montana, USA
 Emeriau-Viard, C., & Brun, A. S. 2017, *ApJ*, 846, 8
 Fan, Y., & Fang, F. 2014, *ApJ*, 789, 35
 Featherstone, N. A., & Miesch, M. S. 2015, *ApJ*, 804, 1
 Finley, A. J., & Matt, S. P. 2018, *ApJ*, 854, 78
 García, R. A., & Ballot, J. 2019, *LRSP*, 16, 4
 García, R. A., Ceillier, T., Salabert, D., et al. 2014, *A&A*, 572, A34
 Garraffo, C., Drake, J. J., & Cohen, O. 2015, *ApJL*, 807, L6
 Gastine, T., Yadav, R. K., Morin, J., Reiners, A., & Wicht, J. 2014, *MNRAS*, 438, L76
 Ghizaru, M., Charbonneau, P., & Smolarkiewicz, P. K. 2010, *ApJL*, 715, L133
 Gilman, P. A. 1983, *ApJS*, 53, 243
 Gilman, P. A., & Miller, J. 1981, *ApJS*, 46, 211
 Gizon, L., & Solanki, S. K. 2004, *SoPh*, 220, 169
 Glatzmaier, G. A. 1985a, *ApJ*, 291, 300
 Glatzmaier, G. A. 1985b, *GApFD*, 31, 137
 Glatzmaier, G. A., & Gilman, P. A. 1982, *ApJ*, 256, 316
 Guerrero, G., Smolarkiewicz, P. K., de Gouveia Dal Pino, E. M., Kosovichev, A. G., & Mansour, N. N. 2016, *ApJ*, 819, 104
 Guerrero, G., Zaire, B., Smolarkiewicz, P. K., et al. 2019, *ApJ*, 880, 6
 Hall, J. C. 2008, *LRSP*, 5, 2
 Hall, J. C., Lockwood, G. W., & Skiff, B. A. 2007, *AJ*, 133, 862
 Hall, O. J., Davies, G. R., van Saders, J., et al. 2021, *NatAs*, 5, 707
 Hanasoge, S., Gizon, L., & Sreenivasan, K. R. 2016, *AnRFM*, 48, 191
 Hazra, S., Réville, V., Perri, B., et al. 2021, *ApJ*, 910, 90
 Hotta, H., & Kusano, K. 2021, *NatAs*, 5, 1100
 Jeffers, S. V., Mengel, M., Moutou, C., et al. 2018, *MNRAS*, 479, 5266
 Johns-Krull, C. M., & Valenti, J. A. 2000, in *ASP Conf. Ser.* 198, *Stellar Clusters and Associations: Convection, Rotation, and Dynamos*, ed. R. Pallavicini, G. Micela, & S. Sciortino (San Francisco, CA: ASP), 371
 Jones, C. A., Boronski, P., Brun, A. S., et al. 2011, *Icar*, 216, 120
 Jouve, L., Brown, B. P., & Brun, A. S. 2010, *A&A*, 509, A32
 Käpylä, M. J., Käpylä, P. J., Olsper, N., et al. 2016, *A&A*, 589, A56
 Käpylä, P. J., Käpylä, M. J., & Brandenburg, A. 2014, *A&A*, 570, A43
 Käpylä, P. J., Mantere, M. J., & Brandenburg, A. 2013, *Geophys. Astro Fluid*, 107, 244
 Käpylä, P. J., Mantere, M. J., Guerrero, G., Brandenburg, A., & Chatterjee, P. 2011, *A&A*, 531, A162
 Käpylä, P. J., Viviani, M., Käpylä, M. J., Brandenburg, A., & Spada, F. 2019, *GApFD*, 113, 149
 Karak, B. B., Käpylä, P. J., Käpylä, M. J., et al. 2015, *A&A*, 576, A26
 Karoff, C., Metcalfe, T. S., Santos, Á. R. G., et al. 2018, *ApJ*, 852, 46
 Kawaler, S. D. 1988, *ApJ*, 333, 236
 Kitchatinov, L. L., Mordvinov, A. V., & Nepomnyashchikh, A. A. 2018, *A&A*, 615, A38
 Küker, M., Rüdiger, G., & Kitchatinov, L. L. 2011, *A&A*, 530, A48
 Lanza, A. F., Das Chagas, M. L., & De Medeiros, J. R. 2014, *A&A*, 564, A50
 Lawson, N., Strugarek, A., & Charbonneau, P. 2015, *ApJ*, 813, 95
 Lehtinen, J. J., Käpylä, M. J., Olsper, N., & Spada, F. 2021, *ApJ*, 910, 110

- Lopes, I., Passos, D., Nagy, M., & Petrovay, K. 2014, *SSRv*, **186**, 535
- Lorenzo-Oliveira, D., Freitas, F. C., Meléndez, J., et al. 2018, *A&A*, **619**, A73
- Lorenzo-Oliveira, D., Meléndez, J., Yana Galarza, J., et al. 2019, *MNRAS*, **485**, L68
- Lorenzo-Oliveira, D., Porto de Mello, G. F., & Schiavon, R. P. 2016, *A&A*, **594**, L3
- Luukko, P. J. J., Helske, J., & Räsänen, E. 2015, *Comput. Stat.*, **31**, 545
- Maehara, H., Notsu, Y., Notsu, S., et al. 2017, *PASJ*, **69**, 41
- Marsden, S. C., Petit, P., Jeffers, S. V., et al. 2014, *MNRAS*, **444**, 3517
- Masada, Y., Yamada, K., & Kageyama, A. 2013, *ApJ*, **778**, 11
- Mason, J., Hughes, D. W., & Tobias, S. M. 2008, *MNRAS*, **391**, 467
- Matilsky, L. I., & Toomre, J. 2020, *ApJ*, **892**, 106
- Matt, S. P., Brun, A. S., Baraffe, I., Bouvier, J., & Chabrier, G. 2015, *ApJL*, **799**, L23
- Matt, S. P., Do Cao, O., Brown, B. P., & Brun, A. S. 2011, *AN*, **332**, 897
- McIntyre, M. E. 2007, in *The Solar Tachocline*, ed. D. W. Hughes, R. Rosner, & N. O. Weiss (Cambridge: Cambridge Univ. Press), 183
- Meibom, S., Barnes, S. A., Platais, I., et al. 2015, *Natur*, **517**, 589
- Metcalfe, T. S., & Egeland, R. 2019, *ApJ*, **871**, 39
- Metcalfe, T. S., Egeland, R., & van Saders, J. 2016, *ApJL*, **826**, L2
- Metcalfe, T. S., Monteiro, M. J. P. F. G., Thompson, M. J., et al. 2010, *ApJ*, **723**, 1583
- Metcalfe, T. S., & van Saders, J. 2017, *SoPh*, **292**, 126
- Miesch, M. S., Brun, A. S., & Toomre, J. 2006, *ApJ*, **641**, 618
- Miesch, M. S., Elliott, J. R., Toomre, J., et al. 2000, *ApJ*, **532**, 593
- Morel, P. 1997, *A&AS*, **124**, 597
- Morin, J., Dormy, E., Schrunner, M., & Donati, J. F. 2011, *MNRAS*, **418**, L133
- Nelson, N. J., Brown, B. P., Brun, A. S., Miesch, M. S., & Toomre, J. 2013, *ApJ*, **762**, 73
- Noraz, Q., Brun, A.-S., Strugarek, A., & Depambour, G. 2021, arXiv:2111.12722
- Noyes, R. W., Hartmann, L. W., Baliunas, S. L., Duncan, D. K., & Vaughan, A. H. 1984, *ApJ*, **279**, 763
- Ó Fionnagáin, D., & Vidotto, A. A. 2018, *MNRAS*, **476**, 2465
- Oláh, K., Kolláth, Z., Granzer, T., et al. 2009, *A&A*, **501**, 703
- Oruba, L., & Dormy, E. 2014, *GeoJI*, **198**, 828
- Parker, E. N. 1955, *ApJ*, **122**, 293
- Parker, E. N. 1993, *ApJ*, **408**, 707
- Passos, D., & Charbonneau, P. 2014, *A&A*, **568**, A113
- Perri, B., Brun, A. S., Strugarek, A., & Réville, V. 2021, *ApJ*, **910**, 50
- Petit, P., Dintrans, B., Solanki, S. K., et al. 2008, *MNRAS*, **388**, 80
- Petitdemange, L. 2018, *PEPI*, **277**, 113
- Pipin, V. V. 2021, *MNRAS*, **502**, 2565
- Plachinda, S. I., & Tarasova, T. N. 1999, *ApJ*, **514**, 402
- Pouquet, A., Frisch, U., & Leorat, J. 1976, *JFM*, **77**, 321
- Racine, E., Charbonneau, P., Ghizaru, M., Bouchat, A., & Smolarkiewicz, P. K. 2011, *ApJ*, **735**, 46
- Rauer, H., Catala, C., Aerts, C., et al. 2014, *ExA*, **38**, 249
- Reiners, A. 2006, *A&A*, **446**, 267
- Reiners, A. 2007, *AN*, **328**, 1034
- Reiners, A., Schüssler, M., & Passegger, V. M. 2014, *ApJ*, **794**, 144
- Reinhold, T., & Gizon, L. 2015, *A&A*, **583**, A65
- Reinhold, T., Reiners, A., & Basri, G. 2013, *A&A*, **560**, A4
- Rempel, M. 2006, *ApJ*, **647**, 662
- Rempel, M. 2008, *JPhCS*, **118**, 012032
- Réville, V., Brun, A. S., Matt, S. P., Strugarek, A., & Pinto, R. F. 2015, *ApJ*, **798**, 116
- Rogers, T. M., & Glatzmaier, G. A. 2006, *ApJ*, **653**, 756
- Saar, S. H. 1990, *MmSAI*, **61**, 559
- Saar, S. H. 2001, in *ASP Conf. Ser.* 223, 11th Cambridge Workshop on Cool Stars, Stellar Systems and the Sun, ed. R. J. Garcia Lopez, R. Rebolo, & M. R. Zapaterio Osorio (San Francisco, CA: ASP), 292
- Saar, S. H. 2011, in *IAU Symp.* 273, *Physics of Sun and Star Spots*, ed. D. Prasad Choudhary & K. G. Strassmeier (Cambridge: Cambridge Univ. Press), 61
- Saar, S. H., & Brandenburg, A. 1999, *ApJ*, **524**, 295
- Schrijver, C. J., De Rosa, M. L., & Title, A. M. 2003, *ApJ*, **590**, 493
- Schrijver, C. J., & Harvey, K. L. 1994, *SoPh*, **150**, 1
- Schrinner, M., Petitdemange, L., Raynaud, R., & Dormy, E. 2014, *A&A*, **564**, A78
- See, V., Jardine, M., Vidotto, A. A., et al. 2015, *MNRAS*, **453**, 4301
- See, V., Matt, S. P., Finley, A. J., et al. 2019a, *ApJ*, **886**, 120
- See, V., Matt, S. P., Folsom, C. P., et al. 2019b, *ApJ*, **876**, 118
- Shibata, K., Isobe, H., Hillier, A., et al. 2013, *PASJ*, **65**, 49
- Shoda, M., Suzuki, T. K., Matt, S. P., et al. 2020, *ApJ*, **896**, 123
- Simard, C., Charbonneau, P., & Dubé, C. 2016, *AdSpR*, **58**, 1522
- Simitev, R. D., & Busse, F. H. 2009, *EL*, **85**, 19001
- Simoniello, R., Jain, K., Tripathy, S. C., et al. 2013, *ApJ*, **765**, 100
- Skumanich, A. 1972, *ApJ*, **171**, 565
- Smolarkiewicz, P. K., & Charbonneau, P. 2013, *JCoPh*, **236**, 608
- Spada, F., & Lanzafame, A. C. 2020, *A&A*, **636**, A76
- Spiegel, E. A., & Zahn, J.-P. 1992, *A&A*, **265**, 106
- Starr, V. P., & Gilman, P. A. 1966, *PapGe*, **64**, 145
- Strugarek, A., Beaudoin, P., Charbonneau, P., & Brun, A. S. 2018, *ApJ*, **863**, 35
- Strugarek, A., Beaudoin, P., Charbonneau, P., Brun, A. S., & do Nascimento, J. D. 2017, *Sci*, **357**, 185
- Subramanian, K., & Brandenburg, A. 2004, *PhRvL*, **93**, 205001
- Takehiro, S.-i., Brun, A. S., & Yamada, M. 2020, *ApJ*, **893**, 83
- Tobias, S. M. 1998, in *ASP Conf. Ser.* 154, *Cool Stars, Stellar Systems, and the Sun*, ed. R. A. Donahue & J. A. Bookbinder (San Francisco, CA: ASP), 1349
- van Saders, J. L., Ceillier, T., Metcalfe, T. S., et al. 2016, *Natur*, **529**, 181
- van Saders, J. L., Pinsonneault, M. H., & Barbieri, M. 2019, *ApJ*, **872**, 128
- Varela, J., Strugarek, A., & Brun, A. S. 2016, *AdSpR*, **58**, 1507
- Vida, K., Oláh, K., & Szabó, R. 2014, *MNRAS*, **441**, 2744
- Vidotto, A. A. 2021, *LRSP*, **18**, 3
- Vidotto, A. A., Donati, J. F., Jardine, M., et al. 2016, *MNRAS*, **455**, L52
- Vidotto, A. A., Gregory, S. G., Jardine, M., et al. 2014, *MNRAS*, **441**, 2361
- Viviani, M., Käpylä, M. J., Warnecke, J., Käpylä, P. J., & Rheinhardt, M. 2019, *ApJ*, **886**, 21
- Viviani, M., Warnecke, J., Käpylä, M. J., et al. 2018, *A&A*, **616**, A160
- Warnecke, J. 2018, *A&A*, **616**, A72
- Warnecke, J., & Käpylä, M. J. 2020, *A&A*, **642**, A66
- Weiss, N. O. 1994, *Lectures on Solar and Planetary Dynamos* (Cambridge: Cambridge Univ. Press), 59
- Wilson, O. C. 1978, *ApJ*, **226**, 379
- Wright, N. J., Drake, J. J., Mamajek, E. E., & Henry, G. W. 2011, *ApJ*, **743**, 48
- Yoshimura, H. 1975, *ApJ*, **201**, 740